Design and Development of MEMS based Guided Beam type Piezoelectric Energy Harvester

Submitted in

fulfillment of the requirements for the degree of

Doctor of Philosophy
by

Shanky Saxena

ID: 2013REC9032

Under Supervision of

Dr. Ritu Sharma

Associate Professor, Dept. of ECE, MNIT, Jaipur

Dr. B.D. Pant
(External Co-Supervisor)

Emeritus Scientist, CSIR-CEERI, Pilani, and Prof. AcSIR, New Delhi

DEPARTMENT OF ELECTRONICS & COMMUNICATION ENGINEERING
MALAVIYA NATIONAL INSTITUTE OF TECHNOLOGY JAIPUR, INDIA

AUGUST 2019

© Malaviya National Institute of Technology Jaipur - 2019.

All rights reserve

DECLARATION

I, Shanky Saxena, declare that this thesis titled, **"Design and Development of MEMS based Guided Beam type Piezoelectric Energy Harvester"** and the work presented in it, are my own. I confirm that:

- This work was done wholly or mainly while in candidature for a research degree at this university.

- Where any part of this thesis has previously been submitted for a degree or any other qualification at this university or any other institution, this has been clearly stated.

- Where I have consulted the published work of others, this is always clearly attributed.

- Where I have quoted from the work of others, the source is always given. With the exception of such quotations, this thesis is entirely my own work.

- I have acknowledged all main sources of help.

- Where the thesis is based on work done by myself, jointly with others. I have made clear exactly what was done by others and what I have contributed myself.

Date: 02-08-2019

Shanky Saxena

(2013REC9032)

CERTIFICATE

This is to certify that the thesis entitled **"Design and Development of MEMS based Guided Beam type Piezoelectric Energy Harvester"** being submitted by **Shanky Saxena (2013REC9032)** is a bonafide research work carried out under my supervision and guidance in fulfillment of the requirement for the award of the degree of **Doctor of Philosophy** in the Department of Electronics and Communication Engineering, Malaviya National Institute of Technology, Jaipur, India. The matter embodied in this thesis is original and has not been submitted to any other University or Institute for the award of any other degree.

Place: Jaipur

Date:

Dr. Ritu Sharma

Supervisor

Associate Professor

Dept. of Electronics and Communication

MNIT, Jaipur

Dr. B.D. Pant

External Supervisor

Emeritus Scientist and Professor

Smart Sensor Area

CSIR-CEERI, Pilani

ACKNOWLEDGEMENT

I would first like to thank my Ph.D. supervisor Dr. Ritu Sharma, Associate Professor, Department of Electronics and Communication Engineering, MNIT, Jaipur for giving her esteemed guidance. She consistently allowed me to pursue my research work but steered me in the right direction whenever she thought I needed it. I am gratefully indebted to her for her valuable comments on this thesis without which this work could not have been successfully conducted.

I would also like to thank Dr. B.D. Pant, Emeritus Scientist & Professor, Smart Sensor Area, CSIR-CEERI, Pilani, whose expertise in MEMS device fabrication has helped me all the way especially while carrying out experimental work. I sincerely thank him for his guidance and efforts he has put in the successful completion of this research work.

I would also like to thank respected director Prof. Udaykumar R Yaragatti and former director Prof. I.K. Bhatt, Dean Academics Prof. K.R. Niazi, former DPGC Convener Prof. Lava Bhargava for permitting me to conduct research and for providing vital resources in the institution.

I would also like to thank D.R.E.C. members Dr. Ritu Sharma, Dr. Ghanshyam Singh, Dr. Vijay Janyani, Dr. C. Periasamy and Dr. Ravi Maddila for giving their valuable and timely suggestions during progress presentations which helped me in the successful completion of research work.

I would sincerely thank the support of scientific and technical staff from CEERI, Pilani, especially from Smart Sensor Area for assisting me in every tough situation and without their expertise, this work, would not have been at all possible. They stood by me in time of failures and assisted me with their field expertise to solve the complex fabrication issues. I pay my gratitude to scientists Dr. Ajay Agarwal Dr. Ravindra Mukhiya, Dr. Santosh Kumar, Dr. Rishi Sharma, Dr. Jitendra Singh, Dr. M. Santosh Kumar. I also thank the technical staff members Supriyo Das, Prateek Kothari, Deepak Panwar, Dhirender Kumar, Arvind Singh, and Ashok K. Gupta and V.B. Sahai.

I would also thank technical staff members from Department of Electronics and Communication Engineering Materials Research Centre, MNIT, Jaipur, Arun Suresh Kumawat, Firoz Ahmed, Sanjay Bagharia, Ramesh Chandra Prajapati, Atul, Bhupesh, Shubham, and other staff members.

I would thank my colleagues from MNIT Jaipur, Dr. Anup Sharma, Mr. Lalit Kumar Dusad, Giriraj Sharma, Jaypdeep Singh Parmar, Prateek Jain, Sidharth Pancholi, Arathy Varghese, Rachana Gupta, Upendra Chaudhary, Dinesh Kotari, Niketa Sharma, and from CEERI, Pilani, Dr. Robin Joyce, Kushboo Singh Raghav, Gurpreet Singh Gill, Ramesh, Ranjan Maurya, Ashish Singh, Prerna Balyan, Sushil, Sadab Hussain and all friends who have supported me in completing my work.

I would thank my beloved parents Shri Anil Kumar Saxena and Smt. Raagni Saxena whom continuous support and never give up attitude has led the foundation for me in completing this Ph.D. journey. I would also thank my sister Yashika Saxena for helping me in my work.

Finally, I would thank God for bestowing grace upon me, which helped me to keep going in the tough times and complete my work successfully.

ABSTRACT

In the current race of miniaturization of microelectronic circuits and systems, the power required by these systems, particularly, by the Wireless Sensor Networks (WSNs) or Mobile Sensor Nodes (MSNs) has reduced to a very low level (milli-watts, microwatts or even in nano-watts in some cases). WSNs consists of many MSNs which are driven by miniaturized lithium ion batteries which are efficient but exhaustible. As these MSNs are remotely mounted or embedded in a system, the replacement of batteries is not feasible which imposes a serious challenge of powering these sensor MSNs for an infinitely long time. Energy harvesting provides an unending power source (few milli-watts) which is adequate to power these sensor nodes specifically for remote area applications. Thus, the focus of the current research work is to design and develop an energy harvester which can convert freely available ambient energy into electrical energy to provide an endless source of power for MSNs. Vibration energy harvesting is of our prime concern because vibrations of different amplitudes and frequencies are freely available in the environment. Vibrations generated from engines, motors, pumps, moving objects such as automobiles, airplanes, wind etc. can be used to harvest energy. Ambient mechanical vibrations range from few hertz (Hz) to 1 KHz e.g. vibration from the rotor blades of the helicopter range from 500 to 2000 Hz, vibrations from human body range ~400 Hz and vibrations from motors range from 30 – 300 Hz.

In Microelectromechanical system (MEMS) based energy harvesters, electrical and mechanical components are integrated into a single device, making them tiny and compact which is suitable for remote area applications. Mostly, MEMS-based vibration energy harvesters are generally, based on three transduction mechanisms, which are electromagnetic, capacitive, and piezoelectric to harvest energy from ambient vibrations. Electromagnetic type uses Faraday's law of electromagnetic induction for the generation of electric potential; however, fabrication of coils and magnets in MEMS fabrication technology is not suitable. Capacitive type operates on variation in capacitance due to vibrations, fabrication is relatively suitable in MEMS but the device requires an initial charging voltage to start operation, which is not suitable at remote area operation. In the present work, the piezoelectric type approach has been considered because of its

simplicity in design, compatibility with MEMS fabrication technology, packaging and device operation. Cantilevers fixed from one end, free from the other or fixed from both ends with a seismic mass at the center (guided beam) are used to realize MEMS-based piezoelectric vibration energy harvesters (P-VEHs). Cantilever structures are modeled as a spring mass damper system, where each cantilever structure has a specific resonance frequency. Maximum displacement occurs when the resonance frequency is in tune with the ambient vibration frequency of the environment resulting in the generation of an electric potential. The design of the cantilevers has to be aimed at low-frequency operation to be in resonance with ambient vibrations. Seismic mass is placed at the free end of the cantilever to reduce the resonance frequency of the structure. Due to ease of fabrication, the seismic mass designed and realized in MEMS is generally square in shape. The following research gaps were observed while doing literature survey (i) Investigation on effect of different shapes of seismic mass on potential generated by P-VEH. (ii) Optimization of dimensions of split electrodes for guided beam structure. (iii) Fabrication, testing, and comparison of guided two-beam and four-beam P-VEH for low-frequency operation.

In the present work, different shapes of the seismic mass i.e. square-shape, pyramidal-shape and triangular-shape have been investigated. The center of mass for the device is analytically calculated by dividing the structure into the cantilever beam and the seismic mass. The geometry of the seismic mass affects the center of mass of the system, resulting in a change in the electric potential generated. FEM simulation using COMSOL Multiphysics® has been carried out to study the effect of different shapes of seismic mass on the potential generated by cantilever type piezoelectric energy harvester. A triangular-shape seismic mass generates a potential of 53.3 mV, whereas a rectangular-shaped seismic mass cantilever structure generates a potential of 52.4 mV, which clearly shows that there is a considerable increase in potential due to the variation in the shape of the seismic mass. The increased potential generated by the triangular-shaped seismic mass is due to the fact that the resultant center of mass of the geometry (cantilever structure and seismic mass section) gets shifted upward, i.e., toward the applied pressure, which results in the exertion of a high force which leads to a higher potential being generated. However, the fabrication of a triangular-shape seismic mass is extremely difficult

because of the technology limitations, the next better option, which is a pyramidal shaped seismic mass, has been selected for further investigation and device fabrication.

Design and FEM simulation has been done for a single beam, guided two-beam, and guided four-beam piezoelectric energy harvester having pyramidal shape seismic mass. Cantilever structures fixed from one end and free from other provide a high output but they are highly fragile and results in low reliability and stability. This limitation can be overcome by the use of guided beam structure fixed at both ends and having seismic mass at the center. Guided two-beam and four-beam structure fixed from ends and having proof mass at the center gives a stable, reliable and improved response as compared to single beam cantilever structure. Seismic mass is supported with two or four-beams which provides stable operation and ability to sustain higher stress values at high amplitude vibrations as compared to single beam cantilever. Guided two or four-beams provide higher stiffness to the structure resulting in lower displacement which reduces frequent collision of the proof mass with the encapsulation layer of the device. As the proof mass at the center is guided by two or four-beams this structure gives lower residual stress as compared to a single beam cantilever structure. Piezoelectric layer on each beam generates two electric potentials in opposite polarities due to compressive and tensile stress which can be harvested using split electrodes. Split electrodes placed at individual beams can be connected in series to increase the net output potential generated. Parameters such as resonance frequency, total displacement, von-Mises stress, output potential, are obtained using FEM as a function of input acceleration for guided two-beam and four-beam piezoelectric energy harvester. At an input acceleration of 1g guided two-beam and guided four-beam structure gives a displacement of 0.107 μm and 0.055 μm respectively. Displacement in the structure generates von-Mises stress of 1.29×10^5 N/m^2 in guided two-beam structure and 0.67×10^5 N/m^2 in guided four-beam structure at 1g input acceleration. Due to stress, on each beam, an electric potential of 23.62 mV is generated in guided two-beam structure whereas guided four-beam structure generates an electric potential of 12.22 mV at 1g input acceleration. Based on these simulation results, the optimized design of guided two-beam and four-beam piezoelectric energy harvester is selected for fabrication using MEMS technology.

Fabrication of MEMS-based guided two-beam and four-beam P-VEH for low-frequency operation has been carried out. A highly c-axis oriented zinc oxide (ZnO) thin film of 2.5 µm thickness was deposited through reactive sputtering of Zn in oxygen ambiance. In order to protect it from environmental deteriorations, it was sandwiched between two layers of 0.5 µm thick PECVD SiO_2. As already stated, the piezoelectric layer develops both tensile as well as compressive stress, the top electrode is split into two electrodes known as split electrodes, whereas the bottom electrode is made of a single electrode, common to both the tensile and compressive stress areas. Aluminum is deposited over the SiO_2 layer using sputtering technique and patterned to form the bottom electrode and top split electrodes through which electric charges are collected. A pyramidal shaped seismic mass which gives a high electric potential has been realized using CMOS compatible 25wt% tetramethylammonium hydroxide (TMAH) wet bulk micromachining of Silicon. The convex corners of the seismic mass were very precisely realized through the design of corner-compensating structures. The thickness of the beams is optimized using deep reactive ion etching (DRIE) to achieve a low-frequency operation. COMSOL Multiphysics® has been used to study the stress distribution to optimize the dimension and placement of the split electrodes. The optimized split electrodes give a reduced resonance frequency by 4.2% when compared with previously used electrode pattern ensuring maximum potential generation for guided two-beam structure. The resonance frequency of the device is experimentally worked out using a Laser Doppler Vibrometer (LDV) and is measured to be 466 Hz for the guided two-beam device and 515 Hz for the guided four-beam device. A PCB was designed to package the device. The packaged device was mounted and tested on a micro-shaker (SPEKTRA SE-10 vibration exciter and 9100D Portable Shaker) output measurement set up. Around resonance frequency of 500 Hz, the packaged two-beam-device exhibits a sensitivity of 1.1392 $mV/m/s^2$ whereas the packaged four-beam device exhibits a sensitivity of 1.0231 $mV/m/s^2$ for the frequency range of 10 to 1000 Hz. Both the devices operate in the frequency range from 10 to 1000 Hz which is the desired frequency range for harvesting ambient vibrations.

Therefore, a reliable and robust vibration energy harvester with reasonably high output has been successfully designed, developed and tested.

List of Publications

International Journal Papers

[1] S. Saxena, R. Sharma and B. D. Pant, "Fabrication and comparison of guided two-beam and four-beam piezoelectric energy harvester for low-frequency operation," in IEEE Journal of Microelectromechanical Systems, vol. 28, no. 3, pp. 513-520, June 2019. doi: 10.1109/JMEMS.2019.2908966.

[2] S. Saxena, R. Sharma and B. D. Pant, "Fabrication and sensitivity analysis of guided beam piezoelectric energy harvester," in IEEE Transactions on Electron Devices, vol. 65, no. 11, pp. 5123-5129, Nov. 2018. doi: 10.1109/TED.2018.2869690.

[3] S. Saxena, R. Sharma, and B. D. Pant, "Dynamic characterization of fabricated guided two-beam and four-beam cantilever type MEMS based piezoelectric energy harvester having pyramidal shape seismic mass," in Microsystem Technologies, vol. 23, no. 12, pp. 5947–5958, Dec. 2017. doi: 10.1007/ s00542-017-3455-0.

[4] S. Saxena, R. Sharma, and B. D. Pant, "Design and development of guided four-beam cantilever type MEMS based piezoelectric energy harvester," in Microsystem Technologies, vol. 23, no. 6, pp. 1751–1759, Jun. 2017. doi: 10.1007/s00542-016-2940-1

[5] S. Saxena and R. Sharma, "Effect of shape of seismic mass on potential generated by MEMS-based cantilever-type piezoelectric energy harvester," in Journal of Micro /Nano-lithography, MEMS, and MOEMS, vol. 13, no. 3, pp. 033012-1–033012-7, Jul. 2014. doi: 10.1117/1.JMM.13.3. 033012.

[6] S. Saxena, R. Sharma, and B. D. Pant, "Design optimization in geometry of seismic mass for MEMS based cantilever type piezoelectric energy harvester for motor vibrations," in Indian Journal of Pure and Applied Physics, vol. 57, no. 5, pp. 334-337, May. 2019.

International Conference Papers

[1] S. Saxena, R. Sharma and B. D. Pant, "Design and development of cantilever-type MEMS based piezoelectric energy harvester," 2015 19th International Symposium on VLSI Design and Test, Ahmedabad, 2015, pp. 1-4. doi: 10.1109/ISVDAT.2015.7208045.

[2] S. Saxena, R. Sharma and B.D. Pant, "Effect of thickness of piezoelectric layer on resonance frequency of Cantilever-type MEMS based piezoelectric energy harvester," 2015 International Conference on Micro-electronics, Communication and Computation, San Diego, USA, 2015, pp.1-5. (Best Paper Award).

[3] S. Saxena, R. Sharma and B. D. Pant, "Design optimization of cantilever based MEMS piezoelectric energy harvester," 2014 International Conference on Devices, Circuits and Communications (ICDCCom), Ranchi, 2014, pp. 1-4. doi: 10.1109/-ICDCCom.2014.7024713.

[4] S. Saxena and R. Sharma, "Effect of seismic mass shape on potential generated by piezoelectric energy harvester," 2014 International Conference on Innovative Advancement on Engineering and Technology, Jaipur National University, Jaipur, 2014, pp. 1-4.

Table of Contents

DECLARATION i

CERTIFICATE ii

ACKNOWLEDGEMENT iii

ABSTRACT v

List of Publications ix

Table of Contents xi

List of Figures xvi

List of Tables xxiv

List of Abbreviations xxvi

List of Symbols xxvii

Chapter-1 1

Introduction 1

1.1 Introduction 1

1.2 Energy Requirement in WSNs 2

1.3 Energy Harvesting for WSNs - State of the Art 4

1.4 Vibration-Based Energy Harvesters 7

1.5 Motivation 14

1.6 Objective of Thesis 14

1.7 Research Methodology 15

1.8 Contributions 15

1.9 Organization of the Thesis ... 16

Chapter 2 ... 18

Literature Review ... 18

Chapter 3 ... 30

Design, Modeling and Comparison of Piezoelectric Energy Harvesters ... 30

3.1 Single cantilever structure ... 30

3.2 Cantilever Generator array ... 36

3.3 Clamped-Clamped or guided beam structures ... 38

3.4 Comparison ... 42

3.5 Effect of shape of seismic mass on potential generated by piezoelectric energy harvester ... 43

3.6 Simulation of different geometries of Seismic Mass ... 46

3.7 Discussion ... 48

3.8 Effect of piezoelectric material on guided beam piezoelectric energy harvester ... 49

Chapter 4 ... 52

Design and FEM Simulation of Guided Beam Piezoelectric Energy Harvester ... 52

4.1 Design of guided four-beam P-VEH ... 52

4.2 FEM analysis of guided four-beam P-VEH ... 54

4.2.1 Resonance Frequency ... 54

4.2.2 Displacement ... 57

4.2.3 von-Mises Stress: ... 59

4.2.4 Electric Potential: 60

4.2.5 Selection of Proof Mass 62

4.3 Comparison of guided two-beam and four-beam piezoelectric energy harvester 64

4.3.1 Comparison of guided two-beam and four-beam piezoelectric energy harvester 64

4.3.2 Resonance frequency 65

4.3.3 Displacement 66

4.3.4 von-Mises Stress 68

4.3.5 Electric potential 69

4.4 Design and Optimization of Split Electrodes for Guided Beam Piezoelectric Energy Harvester 71

4.4.1 Effect of length of split electrode on resonance frequency 74

4.4.2 Effect of length of split electrode on change in capacitance 75

Chapter 5 77

Fabrication of Guided Beam Piezoelectric Energy Harvester 77

5.1 Introduction 77

5.1.1 Fabrication Methodology 77

5.2 Design of Mask Layouts 78

5.2.1 Mask #1: TMAH Etch mask for Pyramidal shape seismic mass 79

5.2.2 Mask #2: Bottom electrode patterning 81

5.2.3 Mask #3: Piezoelectric layer patterning 81

5.2.4 Mask #4: Top electrode patterning 81

5.2.5 Mask #5: DRIE Etch 83

5.3 Fabrication of guided beam piezoelectric energy harvester 83

5.3.1 Device Fabrication Flow 83

5.3.2 Device fabrication (Batch 1) 84

5.4 Detailed unit processes 86

5.4.1 Cleaning 86

5.4.2 Thermal oxidation and LPCVD nitride 87

5.4.3 Lithography (Mask #1) for pyramidal shape seismic mass 87

5.4.4 Reactive ion etching (RIE) for oxide and nitride etch 89

5.4.5 Bulk-Micromachining of silicon for pyramidal shape seismic mass 90

5.4.6 Gold sputtering and bottom electrode patterning (Mask #2) 91

5.4.7 Piezoelectric layer (Zinc oxide) sputtering and patterning (mask #3) 92

5.4.8 Gold sputtering and top electrode patterning (Mask #4) 93

5.4.9 Lithography mask #5 and beam release using DRIE 94

5.4.10 Dicing and device release 96

5.4.11 Discussions 96

5.5 Fabrication process optimization and device fabrication (Batch2) 97

5.5.1 Fabrication flow 98

5.5.2 Fabrication of structure on front side of wafer 98

5.5.3 Bulk-Micromachining of silicon for pyramidal shape seismic mass 98

5.5.4 Guided beam release and thinning using deep reactive ion etching (DRIE) 100

5.5.5 Dicing and device release ... 101

5.6 Design of the PCB and packaging ... 101

Chapter 6 ... 105

Testing and Characterization of Guided Beam Piezoelectric Energy Harvester ... 105

6.1 Structural Characterization ... 105

6.2 Dynamic Characterization using Laser Doppler Vibrometer ... 110

6.2.1 LDV measurement for guided two-beam piezoelectric energy harvester . 111

6.2.2 LDV measurement for guided four-beam piezoelectric energy harvester. 114

6.3 Dynamic Characterization for Batch 2 devices using LDV ... 116

6.3.1 LDV measurement for guided two-beam device ... 116

6.3.2 LDV measurement for guided four-beam device ... 117

6.4 Static capacitance measurement and device packaging ... 118

6.5 Vibration Shaker Test ... 119

6.5.1 Output Voltage/Power versus input acceleration ... 124

6.5.1 Output Voltage versus frequency ... 125

Chapter 7 ... 128

Conclusion and Future Scope ... 128

7.1 Contributions ... 128

7.2 Future Scope ... 129

REFERENCES ... 130

Bio - Data ... 142

List of Figures

Fig. 1.1 (a) car tire pressure monitors (b) wireless weather station (c) implantable/mobile medical devices 1

Fig. 1.2 SN schematic depicting various functional units 3

Fig. 1.3 Generic model of a vibration-based micro-generator 8

Fig. 1.4 Electromagnetic Energy Harvester. 10

Fig. 1.5 Electrostatic energy harvester Vullers et al. 11

Fig. 1.6 Cantilever beam fixed from one end and seismic mass at other 12

Fig. 1.7 Fabricated guided two-beam device Marzencki et al. 12

Fig. 2.1 (a) An array of cantilever beams acting as band pass filter: the beam dimensions and the proof masses at the tips are chosen in such a manner that the array acts as band-pass filter allowing a certain frequency range pass through. (b). The pass band frequency 19

Fig. 3.1 Deflection of cantilever beam 30

Fig. 3.2 Mechanical deformation of a coil spring under point loading force 31

Fig. 3.3 (a) Resonance frequency of the free end cantilever is 1593.1 Hz. (b) Resonance frequency of the cantilever with proof mass is 764.05 Hz. 33

Fig. 3.4 Graph of resonance frequency vs. cantilever length 33

Fig. 3.5 FEM simulation of single beam cantilever 34

Fig. 3.6 Graph of displacement of the cantilever from fixed end towards free end. 35

Fig. 3.7 Graph of von-Mises stress generated from fixed end towards free end. 35

Fig. 3.8 Line graph of electric potential generated from fixed end towards free end. 36

Fig. 3.9 Generator array of three cantilevers 37

Fig. 3.10 Line graph of displacement of Cantilever array type P-VEH 38

Fig. 3.11 Snapshot of eigen mode generated by the guided two-beam structure 39

Fig. 3.12 Line graph of total displacement v/s arc length of guided beam type structure. 40

Fig. 3.13 Graph of von-Mises stress v/s arc length of guided beam structure................. 41

Fig. 3.14 Graph of electric potential generated at various arc length for guided beam structure.. 41

Fig. 3.15 (a) The shape of seismic mass (triangular) when the ratio r = 0, (b) the modified shape of seismic mass (pyramidal) at r = 0.4, and (c) the shape of seismic mass (rectangular) at r =1. 44

Fig. 3.16 (a) Displacement generated along the surface of the cantilever structure. (b) Distribution of von-Mises stress along the surface of the cantilever structure................ 46

Fig. 3.17 (a) Displacement versus arc length graph for different values of r. (b) Displacement versus arc length graph extended curve from arc length 388µm to 392 µm for different values of r. 47

Fig. 3.18 (a) von-Mises stress versus arc length graph for different values of r. (b) von-Mises stress versus arc length graph extended curve from arc length 384 to 392 µm for different values of r. 48

Fig. 3.19 (a) Electric potential versus arc length graph for different values of r. (b) Electric potential versus arc length graph extended curve from arc length 330 to 390 µm for different values of r. 49

Fig. 4.1 Snapshot of design structure for guided four-beam P-VEH............................... 53

Fig. 4.2 Cross-sectional view of the proof mass. 54

Fig. 4.3 Resonance frequency for four-beam guided cantilever structure at a beam thickness of 5µm is 335.96 Hz obtained using FEM. 55

Fig. 4.4 Resonance frequency at a thickness of 5 µm to 20 µm of the silicon beam. The minimum and maximum resonance frequency obtained at 335.96 Hz and 1631.4 Hz for beam thickness of 5 µm and 20 µm respectively. 56

Fig. 4.5 Displacement versus arc length graph for the guided beam for input acceleration from 1g to 5g. Displacement values of 0.095 µm and 0.479 µm are obtained at an input acceleration of 1g and 5g respectively. 58

Fig. 4.6 Single beam cantilever with proof mass having resonance frequency of 1611.9 Hz gives displacement of 0.14 µm at an input acceleration of 1g. 59

Fig. 4.7 von-Mises stress versus arc length graph for the guided beam for input acceleration from 1g to 5g. Maximum stress values of 9.4 x 10^4 N/m^2 and 4.7 x 10^5 N/m^2 is obtained at an input acceleration of 1g and 5g respectively 60

Fig. 4.8 Electric potential versus arc length graph for the guided beam for input acceleration from 1g to 5g. Maximum electric potential of 17.84 millivolts and 89.21 millivolts is obtained at an input acceleration of 1g and 5g respectively. 61

Fig. 4.9 Snapshot of design structure for (a) guided two-beam and (b) guided four-beam P-VEH. 65

Fig. 4.10 (a). Snapshot of first mode at 1535.2 Hz for guided two-beam P-VEH. (b). Snapshot of first mode at 2141.1 Hz for guided four-beam P-VEH. 66

Fig. 4.11 (a). Displacement versus arc length graph for the guided two-beam for input acceleration from 1g to 5g. Maximum displacement 0.107 µm and 0.537 µm is obtained at an input acceleration of 1g and 5g respectively. (b). Displacement versus arc length graph for the guided four-beam for input acceleration from 1g to 5g. Maximum displacement 0.055 µm and 0.279 µm is obtained at an input acceleration of 1g and 5g respectively. 67

Fig. 4.12 (a). von-Mises stress versus arc length graph for the guided two-beam for input acceleration ranging from 1 to 5 g. Maximum stress values of 1.29 x 10^5 N/m^2 and 6.49 x 10^5 N/m^2 is obtained at an input acceleration of 1g and 5 g respectively. (b) von-Mises stress versus arc length graph for the guided four-beam for input acceleration ranging from 1 to 5 g. Maximum stress values of 0.67 x 10^5 N/m^2 and 2.6 × 10^5 N/m^2 is obtained at an input acceleration of 1g and 5 g respectively. 69

Fig. 4.13 (a). Electric potential versus arc length graph for the guided two-beam for input acceleration from 1g to 5 g. Maximum electric potential of 24.28 mV and 121.38 mV is obtained at an input acceleration of 1g and 5 g respectively. (b). Electric potential versus arc length graph for the guided four-beam for input acceleration from 1g to 5 g. Maximum electric potential of 12.22 mV and 61.12 mV is obtained at an input acceleration of 1g and 5 g respectively. Single beam of guided four-beam structure generates half the potential (12.22 mV) compared to guided two-beam cantilever structure but the net potential generated by the four-beams would be 48.88 mV (4x 12.22 mV) which is equal to the electric potential generated by two-beams of the guided two-beam cantilever structure. 70

Fig. 4.14 Displacement and von-Mises stress along the length of the beam at1g. Electrodes T1 and T2 placed at region A and C of maximum tensile and compressive stress. 73

Fig. 4.15 Beam thickness vs. resonance frequency at different electrode pattern. 74

Fig. 4.16 Change in displacement and capacitance due to variation of electrode length from 675 µm to 2500 µm. 76

Fig. 5.1 (a) 5 - Level mask layout for guided two-beam device (b) 5 - Level mask layout for guided four-beam device. 79

Fig. 5.2 (a) TMAH opening mask #1 for pyramidal shape seismic mass. (b) Corner compensation design to obtain perfect edges of seismic mass 80

Fig. 5.3 Mask #2 for bottom electrode patterning for (a) two-beam device (b) four-beam device. 81

Fig. 5.4 Mask #3 for piezoelectric layer patterning (a) two-beam device (b) four-beam device. 82

Fig. 5.5 Mask #4 for top electrode patterning (a) two-beam device (b) four-beam device. 82

Fig. 5.6 Mask #5 DRIE etching (a) two-beam device (b) four-beam device........ 83

Fig. 5.7 Fabrication flow steps of the device (a) Thermal oxidation and LPCVD nitride deposition (b) Oxide patterning for pyramidal shape seismic mass (mask #1)and etching (c) TMAH etching. (d) Dry oxidation (e) Cr-Gold deposition and patterning (mask #2)(f) ZnO deposition and patterning (mask #3) (g) Gold deposition and patterning (mask #4). (h) Patterning for release of guided beams (mask #5). 85

Fig. 5.8 (a) Piranha cleaning of wafers. (b) HF dip of wafers for oxide removal. 86

Fig. 5.9 (a) Wafers loading in thermal oxidation furnace. (b) Wafers loading in LPCVD nitride furnace. 87

Fig. 5.10 (a) Wafers after moisture bake for photoresist coating. (b) Positive photoresist S1818 coating process on spin coater. 88

Fig. 5.11 (a) PR coated wafer alignment with mask #1. (b) Exposure of the wafer through mask #1. 88

Fig. 5.12 (a) Developer CD26 (left) and two DI water beakers. (b) Developing UV exposed PR coated wafer in CD26 developer........ 89

Fig. 5.13 (a) Wafers loading in RIE machine (b) Plasma etching during the process....... 89

Fig. 5.14 (a) TMAH setup during etching process. (b) Seismic mass obtained after etching. 90

Fig. 5.15 (a) HF dip of wafers for oxide and nitride removal (b) Dry oxidized wafers. .. 91

Fig. 5.16 (a) Back side alignment for bottom electrode patterning. (b) Developing pattered wafers. 92

Fig. 5.17 (a) Chrome/gold etching of wafers. (b) Patterned bottom electrode wafer. 92

Fig. 5.18 (a) Wafer mounting on holder of ZnO sputtering machine. (b) ZnO deposition in process. 93

Fig. 5.19 (a) Patterned top electrode wafer (b) Zeta image of the device from the front showing the top and bottom electrode pattern. 94

Fig. 5.20 (a) Wafer stick to six-inch wafer after lithography. (b) Lateral view of the wafer. 94

Fig. 5.21 (a) Beam release after DRIE. (b) Lateral view of the released beams. 95

Fig. 5.22 (a) PR removal after DRIE. (b) Wafer with released beams. 95

Fig. 5.23 Snapshot of fabricated guided (a) two-beam and (b) four-beam piezoelectric energy harvester. 96

Fig. 5.24 (a) Cross-sectional SEM image of the beam. (b) Zeta image of the ZnO pattern after etching. 97

Fig. 5.25 Fabrication steps for device (a) Thermal oxidation (b) Aluminum deposition and patterning (mask #1). (c) PECVD SiO2 deposition. (d) ZnO deposition and patterning (mask #2). (e) PECVD SiO2 deposition. (f) Aluminum deposition and patterning (mask #3). (g) Oxide patterning for pyramidal shape seismic mass (mask #4) and TMAH etching. (h) Patterning for guided beams (mask #5), DRIE front release and dicing. 99

Fig. 5.26 Snapshot of the front side protection of the processed wafer with Zig for TMAH etching. 100

Fig. 5.27 (a) Snapshot of wafer after DRIE etch of Si from front side. (b) Snapshot of bulk-micromachined side of the wafer in process during beam thinning process. 101

Fig. 5.28Snapshot of fabricated guided (a) two-beam and (b) four-beam piezoelectric energy harvester. 101

Fig. 5.29 (a) Snapshot of PCB package. (b) Device mounted on a PCB package. 102

Fig. 5.30 (a), (b) PCB with connectors to connect the devices to the vibration analyzer. 103

Fig. 6.1 (a) XRD pattern of the device (b) XRD pattern of ZnO deposited on a bare silicon wafer. 106

Fig. 6.2 SEM image of the bottom view of the pyramidal shape seismic mass. 107

Fig. 6.3 SEM image of the top view of the pyramidal shape seismic mass. 107

Fig. 6.4 SEM image of the beam with bottom electrode. 108

Fig. 6.5 SEM image of the split electrodes each having dimensions of 675 µm. 108

Fig. 6.6 SEM image of the interface of the top electrode and the piezoelectric layer 109

Fig. 6.7 (a) and (b) AFM images of the gold metal deposited for electrodes. 110

Fig. 6.8 (a) and (b) AFM images of deposited 2 µm thick ZnO layer. 110

Fig. 6.9 Experimental setup of LDV used to measure dynamic response of the device at CSIR-CEERI. 112

Fig. 6.10 Extended view of the device mounted on the piezo disc for LDV measurement. 112

Fig. 6.11 Snapshot of Scanning LDV measurement result for guided two-beam device. The device operates in dominant frequency mode (±Z direction). 113

Fig. 6.12 Frequency versus displacement curve for the two-beam device obtained using LDV. The resonance frequency for the device obtained experimentally comes at 1971.9 Hz giving a maximum displacement of 49.67 nm. 113

Fig. 6.13 Snapshot of Scanning LDV measurement result for guided four-beam device. The device operates in dominant frequency mode (±Z direction). 115

Fig. 6.14 Frequency versus displacement curve for the four-beam device obtained using LDV. The resonance frequency for the device obtained experimentally comes at 2540.6 Hz giving a maximum displacement of 32.17 nm. 115

Fig. 6.15 Frequency versus displacement curve for the two-beam device. The resonance frequency for the device obtained experimentally is 466.3 Hz. 117

Fig. 6.16 Frequency versus displacement curve for the four-beam device. The resonance frequency for the device obtained experimentally is 515 Hz. 118

Fig. 6.17 Low level CV measurement of device at CSIR-CEERI. 119

Fig. 6.18 (a) Device mounted on PCB package. (b) Device package sealed for testing. 119

Fig. 6.19 Snapshot of fabricated guided two-beam energy harvester device. 120

Fig. 6.20 (a) Device mounted on SPEKTRA SE-10 vibration exciter setup at Acoustics and Vibration standards laboratory, National Physical Laboratory, Delhi, India........... 120

Fig. 6.21 Extended view of the device mounted on SE-10 vibration exciter. 121

Fig. 6.22 Sensitivity of the device measured from SE-10 at T1 and T2 electrodes........ 122

Fig. 6.23 Guided four-beam device mounted on SE-10 vibration exciter. 123

Fig. 6.24 Comparison of sensitivity of guided two-beam and four-beam device. 123

Fig. 6.25 Device mounted on 9100D Portable Shaker. 124

Fig. 6.26 Voltage/power vs acceleration amplitude from 0.5 g to 5 g. 125

Fig. 6.27 Output voltage vs frequency test using 9100D portable shaker. 126

Fig. 6.28 Output voltage and frequency at acceleration ranging from 0.5 to 3g. 126

List of Tables

Table 1.1 Comparison of power consumption for commercially available MSNs [3]....... 2

Table 1.2 MICA2 motes SN energy consumption 3

Table 1.3 Classification of Energy harvesting techniques based on ambient source and their key characteristics suitable for WSN.. 6

Table 1.4 Low-frequency Vibrations 7

Table 3.1 Comparison of the three structures used as piezoelectric energy harvester. 42

Table 3.2 Comparison of different shape of seismic mass 45

Table 3.3 Comparison for different piezoelectric materials for guided four beam P-VEH ……………………………………………………………………………………………50

Table 3.4 Comparison for different piezoelectric materials for guided two beam P-VEH ……………………………………………………………………………………………50

Table 4.1 Electric potential generated by one beam due to tensile and compressive stress at fixed end and guided end of four-beam guided cantilever structure............................ 62

Table 4.2 Displacement, von-Mises stress and Electric potential at different dimensions of proof mass.. 63

Table 4.3 Comparison of maximum displacement at an input acceleration range of 1g to 5g for guided two-beam and four-beam cantilever structure.. 68

Table 4.4 Comparison of von-Mises stress at an input acceleration range of 1g to 5g for guided two-beam and four-beam cantilever structure. 69

Table 4.5 Summarizes the electric potential generated by one beam of guided four-beam cantilever structure due to tensile and compressive stress at fixed end and guided end. . 71

Table 4.6 Comparison of resonance frequency for three different electrode patterns...... 75

Table 5.1 Mask details Device: MEMS-VEH: Die size: 12.5 x 12.5 mm........................ 78

Table 5.2 Fabrication Steps.. 84

Table 5.3 Comparison for two-beam and four-beam device. 103

Table 6.1 Comparison of sensitivity of guided two-beam and four-beam device.......... 124

Table 6.2 Comparison with published work.. 127

List of Abbreviations

AFM - Atomic Force Microscopy

DRIE - Deep reactive ion etching

DI - Deionized

EMF - Electro motive force

FFT - Fast Fourier transform

LDV - Laser Doppler Vibrometer

MEMS - Microelectromechanical systems

MFC - Microbial Fuel Cell

MSN - Mobile Sensor Node

PB - Piezoelectric Biomorph

PECVD - Plasma enhanced chemical vapor deposition

PVDF - Polyvinylidene Flouride

P-VEH - Piezoelectric Vibration Energy Harvester

PZT - Lead Zirconate Titanate

SEM - Scanning electron microscope

TMAH - Tetramethylammonium Hydroxide

TPMS - Tire pressure monitoring system

WSN - Wireless Sensor Network

XRD - X-ray Diffraction

List of Symbols

Al - Aluminum

AlN - Aluminum Nitride

Au - Gold

b - Damping

C - Capacitance

E - Young's Modulus

HCl - Hydro chloric

I - Moment of Inertia

k - Spring constant

l - Length of cantilever

m - Seismic mass

Pt - Platinum

Si - Silicon

SiO_2 - Silicon oxide

t - Thickness of beam

W - Width of cantilever

x - Distance between plates

ZnO - Zinc oxide

Chapter-1

Introduction

1.1 Introduction

A Wireless Sensor Network (WSN) consisting of a large number of randomly deployed Mobile Sensor nodes (MSNs) was initially introduced with a focus on intrusion detection for tactical applications [1]. Since then, WSNs have been used in diverse applications such as measurement of microclimates in agriculture farms, on road traffic monitoring, detection of human presence in workplaces and homes, and many more [2]. WSNs consist of several different functional parts i.e. a transducer, an analog to digital converter, a wireless transmitter/receiver and a battery to power the system. WSNs has remote area applications as shown in Fig. 1.1 (a) pressure monitors for car tires (b) wireless weather stations and (c) implantable/mobile medical devices. These WSNs are powered by small lithium-ion batteries which are efficient but are not environment friendly and exhaustible [3].

Fig. 1.1 (a) car tire pressure monitors (b) wireless weather station (c) implantable/mobile medical devices

Replacement of these batteries, typically in remote locations is practically not feasible. Moreover, these batteries make the overall system heavy through addition of its weight

and volume thereby lowering the overall efficiency. These batteries also adversely affect the environment when discarded without necessary precautions [4].

WSNs powered with natural sources such as thermal energy, wind energy, solar energy, vibration energy, etc. stands an effective solution for the aforesaid problem. Therefore, the main objective here is to design and develop an energy harvester mounted WSNs that can power remotely for a longer period or ideally for infinitely long time. The above idea has evolved from the fact that the low power nano and micro devices have very low power requirements which can be effectively met using an energy harvester.

1.2 Energy Requirement in WSNs

Recent advancements in microelectronics have reduced the device power consumption to milliwatt or microwatt levels through miniaturization [5]. The small size, low power consumption and remote operational capability of WSNs have gained them huge research focus in the past decades. Table 1.1 summarizes some commercially available wireless MSNs along with their power consumption levels [3].

Table 1.1 Comparison of power consumption for commercially available MSNs [3].

Node Name	Sleep Mode	Transmit Mode	Receive Mode	Duty Cycle	Operating Voltage	Batteries Required	Battery Life
Fleck3	80 µA	36.8 mA	18.4 mA	0.27 mA	3.3 V	3 no.	440 days
XBee™	10 µA	45 mA	50 mA	0.51 mA	2.8 V	2 no.	230 days
MICAz™	-	-	-	0.70 mA	2.7 V	2 no.	170 days

As already stated, a SN consists of multiple functional units i.e. Transducer, A/D converter, Battery, Memory, Embedded processor and a Trans-receiver as shown in Fig.

1.2. A Transducer or a sensor converts different form of energy (thermal, mechanical, etc.) to electrical energy and holds the responsibility of measuring the physical parameters of the sensor locality [1].

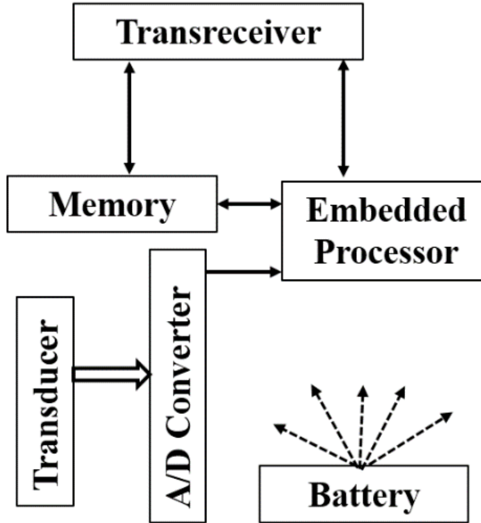

Fig. 1.2 SN schematic depicting various functional units [1]

The output from a sensor is in the form of analog current or voltage, which requires conversion in digital form and is done with the aid of Analog to Digital converter. This digital signal output from the A/D converter then gets processed by a dedicated embedded processor. The wireless Transmitter/Receiver that transmits or receives data wirelessly at any time of interest becomes the heart of the SN. All these individual components/units get powered by small batteries embedded within the system. Commercial version of a SN is named as ‘mote’ [1]. Table 1.2 gives the power required for different component of SN.

Table 1.2 MICA2 motes SN energy consumption [1].

Component	**Current**	**Power**
Nothing Test	.0075 mA	23.25 nW
Radio off	.004 mA	12.4 nW

Radio idle	16 mA	49.6 μW
Radio receiver	16 mA	49.6 μW
Radio Transmit	21 mA	65.1 μW
Consumption alone	.010 mA	31.0 nW
Transmission Cost	-	.001 mJ/bit

It can be seen from Table 1.2 that the power required for the operation of different components of SNs ranges from milliwatt to microwatt level. This power is provided by an exhaustible battery which requires timely replacement. Therefore, we aim to harvest energy from ambient conditions to power these MSNs which is discussed in the next sections.

1.3 Energy Harvesting for WSNs - State of the Art

"Energy harvesting is a technology that converts the excess energy available in the environment into usable energy for low power electronics" [6]. Energy harvesting from environmental sources can be integrated with WSNs to enable perpetual operation and prolong the system lifetime. The major techniques that can be used for the same matching the WSN node constraints include light energy, heat energy, energy from vibrations etc. Based on the energy source, the state of the art technologies used for energy-harvesting in WSNs is presented [2].

Popular kinetic energy sources are mechanical stress, vibrations from manufacturing machines and sound waves. Vibration energy finds applicability in devices whose operational principle rely on electromagnetic, electrostatic and piezoelectric effects [7]. Sazonov et al. [8] in 2009 developed an energy harvester based on an electromagnetic approach which was employed for bridge health monitoring systems that can generate 12.5 mW from vehicular traffic vibrations. Rajamani and Vijayaraghavan [9] in 2010 implemented a self-sustainable WSN that effectively monitors the traffic flow utilizing

the vibration energy of the passing vehicles. On board, sensors can also be powered using vehicular vibrations. Piezoelectric harvesters utilizing vehicular vibrations were used by Talampus and Tolentino [10] in 2012 designed a self-powered vehicle tracker. Electrostatic harvesters were used by Lohndorf et al. [11] in 2007 to evaluate their applicability in self-sustained tire pressure monitoring system (TPMS) ensuring safety of trailer trucks, heavy vehicles, etc. Dondi et al. [12] in 2012 developed a WSN comprising of different magnetometers and accelerometers which employs piezoelectric energy harvesters that get self- powered and also powers the nodes from trailer induced vibrations.

Extraction of energy from electromagnetic radiations below infrared spectrum is feasible as per photoelectric effect taking visible/solar energy as a primary example. Solar cells or photovoltaic cells comprising of two layers of semiconductor (commonly Si) material is conventionally used for energy harvesting using photoelectric effect. Solar cells extending the battery life of MSNs in an automated and self-sustainable irrigation system were demonstrated by Gutierrez et al. [13] in 2014. Further Brunelli et al. [14] in 2008 enhanced the efficiency of the solar cells through a 1mW (low power) tracking module for energy harvesting at micro-levels. Yerva et al. [15] in 2012 demonstrated a sensor capable of harvesting indoor solar energy sufficient enough to transmit and receive minute wise sensor data through a pre-defined collection route tree.

Radio frequency energy transmitted from WiFi network, FM radio and cellular stations can be harvested. Cong et al. [16] in 2009, designed and demonstrated a self-sustainable blood pressure monitor with dimensions in millimeter scale that gets powered from external RF sources. Similarly, another micrometer scale cubic sensor got demonstrated by Sun et al. [17] in 2012 with a rectenna capable of harvesting 1µW of power to be used in implantable sensors.

Thermoelectric energy harvesters, based on temperature difference got employed to power WSN self-powered node by Zhao et al. [18] in 2014. Structural health monitors for water, oil and gas pipes demonstrated has been done by Zhang et al. [19] in 2011 and Martin et al. [20] in 2012 used thermal sources in the environment such as steam and hot water. Rizzon et al. [21] in 2013 utilized energy from heat dissipation of CPUs in data

centers in order to run dedicated WSNs meant for environment monitoring. Thermal energy harvesters can simultaneously act as harvesters and sensors as presented by Campbell et al. [22] in 2004, and Lossec et al. [23] in 2013 suggested that medical sensors can be powered using the warmth of animal or human bodies.

Energy harvesting may be accomplished from chemical or biological energy depending on the environment of interest. Microbial fuel cells (MFCs) powered small oceanographic sensors presented by Reimers et al. [24] in 2001generated a constant output power: 0.05 W/m^2. Further, Donovan et al. [25] in 2008 demonstrated a power management system boosting the voltage of these fuel cells making them suitable for use in wireless temperature sensors ensuring extended lifetimes of at least a year in natural water. Gong et al. [26] in 2011 demonstrated a footprint MFC of 0.25 m with an average output power of 44 mW/m^2 powering an acoustic modem that transmits measured temperature values over 50 days.

Table 1.3 Classification of Energy harvesting techniques based on ambient source and their key characteristics suitable for WSN.

Source of energy		Extraction Technique	Application domain	Harvested output power	Available energy	Type of operation	Literature reference
Kinetic	Vibration	Electromagnetic	Structural health monitoring	12mW	Intermittent	Intermittent	Sazonov et al. [8] [2009]
	Vibration	Piezoelectric	Safety of vehicles	13.5µW	Continuous	Continuous	Lohndorf et al. [11] [2007]
	Vibration	Piezoelectric	Safety of agriculture machinery	724µW	Intermittent	Intermittent	Scorcioni et al. [27] [2011]
	Air flow	Electromagnetic	Detection of forest fire	7.7mW(@3.6m/s)	Continuous	Continuous	Tan and Panda [28] [2011]
	Air flow	Electromagnetic	Automatic HVAC	45mW(@9 m/s)	Intermittent	Intermittent	Sardini and Serpelloni [29] [2011]
	Water flow	Electromagnetic	Water pipe monitoring	18mW	Continuous	Continuous	Morais et al. [30] [2008]
	Human motion	Piezoelectric	Biomedical implants	1mW	Intermittent	Intermittent	Almouahed et al. [31] [2011]
	Animal motion	Electromagnetic	Herd localization	N/A	Intermittent	Intermittent	Dopico et al. [32] [2012]
Radiant	Indoor light	Amorphous crystalline	Indoor applications	180µW	Intermittent	Intermittent	Roundy et al. [33] [2013]

	Sun light	Amorphous crystalline	Smart irrigation	240mW	Intermittent	Continuous	Gutierrez et al. [13] [2014]
	Ambient RF	Rectenna	Outdoor sensing	60μW	Continuous	Continuous	Sample et al. [34] [2007]
Thermal		Thermoelectric	Environment monitoring	218μW	Continuous	Continuous	Rizzon et al. [21] [2013]
		Thermoelectric	Water metering	250μW	Continuous	Continuous	Campbell et al. [35] [2014]
Biochemical		Microbial fuel cell	Precision agriculture	310.24μW	Continuous	Continuous	Pietrelli et al. [36] [2014]

From the above Table 1.3 it is clear that the kinetic energy from vibrations is highly suitable for harvesting energy for WSNs. Therefore, we further focus our investigation on vibration-based energy harvesters.

1.4 Vibration-Based Energy Harvesters

Vibration energy is a very promising and unending source of energy. They are random vibrations which are having different amplitudes and frequency that are freely available everywhere [37]. The different frequencies available in the environment suitable for vibration energy harvesting is given in Table 1.4.

Table 1.4 Low-frequency Vibrations

Application Domain	Vibration Frequency Range	Reference
Motor vibrations (car, engines)	30 - 300 Hz	Jha et al. [38] [1976]
Human body vibrations	~ 400 Hz	Koenig et al. [39] [2008]
Chopper Vibrations	500 - 2000 Hz	Szefi et al. [40] [2004]

Most vibration energy harvesters (also called vibration-based micro-generators) are modeled as single degree-of-freedom second-order spring-mass systems (see Fig. 1.3) as first described by Williams and Yates [41]. The system consists of an inertial frame that transmits the vibration to a suspended inertial mass, m, via the spring, k, and the damper, b, to produce a relative displacement or cause mechanical strain.

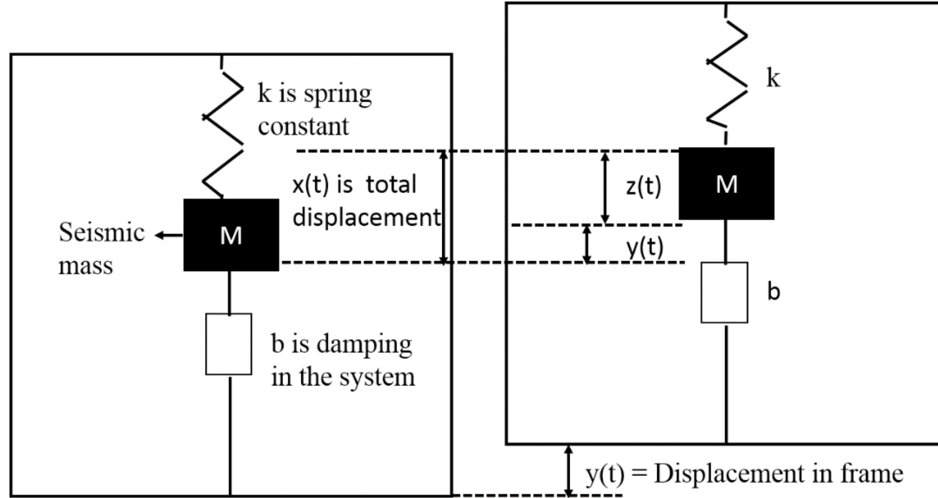

Fig. 1.3 Generic model of a vibration-based micro-generator [41].

Fig. 1.3 shows an inertial structure with simple mass-spring-damper system attached to a fixed frame. If generator housing vibrates with a displacement y(t), which displaces the mass by z(t) due to relative motion with respect to housing then the differential motion is given by equation 1.1.

$$m\ddot{z}(t) + b\dot{z}(t) + kz(t) = -m\ddot{y}(t) \qquad 1.1$$

The force on the mass is equal to the force on the mass-spring damper given by equation 1.2.

$$F = -m\ddot{y}(t) \qquad 1.2$$

The power transfer in the mass, p(t), is the product of the force on the mass and its velocity given by equation 1.3.

$$p(t) = -m\ddot{y}(t)[\dot{y}(t) + \dot{z}(t)] \qquad 1.3$$

The motion of the mass relative to the fixed frame due to damping explains the basic principle of operation of the device. The relative displacement created with respect to the housing results from the vibration of the mass spring system which, in turn, is due to the vibration of the fixed frame or housing due to the environmental vibrations. Resonance frequency when matches with the excitation frequency, then the mass stroke is magnified

by the total damping ratio of the system and a considerable amount of energy is converted to useful electrical energy.

Vibration energy harvesters are realized through MEMS technology because in MEMS technology, electrical and mechanical components are integrated in the form of tiny devices or systems [42]. This enables the integration of the mechanical moving parts such as cantilever beams with the electrical parts like circuit used for signal conditioning. These systems having sizes varying from micrometers to millimeters are fabricated by making use of standard batch processing techniques have got inherently the ability to function as controllers, actuators and sensors in micro scale by proper processing or amplification. MEMS devices or systems gain advantages from the excellent mechanical and electrical properties and stability of Si, whereas the ICs exploit only its electrical properties. MEMS, in general, comprises of mechanical micro sensors, micro actuators, microelectronics and micro sensors all integrated into a single Silicon chip [43]. SNs used in WSN are also MEMS-based sensors therefore, integration of these SNs with a MEMS-based vibration energy harvester is highly suitable.

Three transduction mechanisms i.e. electromagnetic, capacitive and piezoelectric are used to scavenge vibration energy that can be realized in MEMS technology [44]. To couple the environmental vibrations to the transduction method, vibration energy harvesting require a transducer and an energy converter. Such transducers must be designed carefully to maximize the energy converted with minimum loss.

The Electromagnetic type energy harvesters operate on the principle of Faraday’s law of electromagnetic induction i.e. induction of EMF (Electro motive force) in a coil due to change in magnetic flux linked with the coil [45]. A basic prototype of electromagnetic type energy harvester is shown in Fig. 1.4 [45]. Resistance to the relative motion of charges in any magnetic field is created by the combined force on the moving charges as stated by Lenz’s law. This resistive force leads to the generation of heat in the system as, work will be done by the moving charges to overcome the resistive force and to store the energy developed by the magnetic field, which depends on the inductance of the circuit. Thus by using permanent magnets, resonating cantilever beam and a coil, achievement of electromagnetic induction become feasible [46].

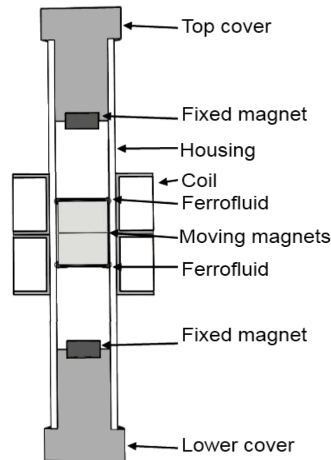

Fig. 1.4 Electromagnetic Energy Harvester [45].

One among the two, the magnet or coil will be kept fixed while the other would be mounted on a beam. However, it is more preferable when the magnet is attached to the beam instead of the coil as they have the capability to act as inertial mass. The resonant frequencies of such systems have to be carefully designed to match the application environment specific characteristic frequency so that the amplitude of the environment vibration gets amplified by the quality factor linked with the resonant system [47].

Electrostatic type energy harvesters are based on the principle of constant charge separation. Increasing the electrical potential of charge by moving a fixed charge along an electric field is one of the methods of operation of an electrostatic transducer [48]. In a parallel plate capacitor with negligible fringing field, constant overlap and variable separation between the plates that are perfectly isolated from one another by air or vacuum as shown in Fig. 1.5 [49].

Electrostatic field developed will be independent of the plate separation and will be directly proportional to charge involved, which is fixed. The mechanical work is done, which would be against the attractive force existing between the parallel plates, leads to an increase in separation between the plates and additional storage of electrical/potential energy. When a force acts on the plates and the plates are moved relatively maintaining a fixed/constant separation, the work done will be against the existing fringing fields leading to an increment electric field.

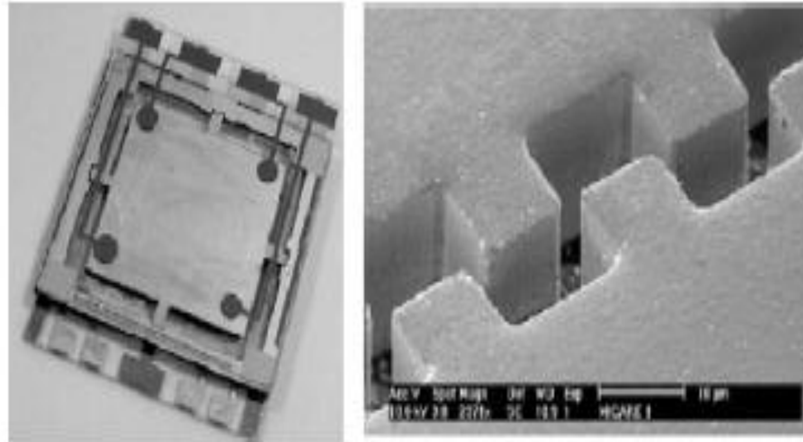

Fig. 1.5 Electrostatic energy harvester Vullers et al. [49].

The reduction in plate overlap leads to an enhancement in the stored electrical energy as field density increases at a faster rate than decrease in volume of the field as it is proportional to the square of the absolute magnitude of field strength. Some initial amount of energy becomes an essential requirement in all electrostatic transducers to generate the resultant higher electrical energy which is a demerit of using them in energy harvesting applications [50].

Piezoelectric energy harvesters are based on the phenomenon of piezoelectric effect which was discovered by J and P Curie [51]. Piezoelectric polarization fields are generated when the mechanical strain in material results in production of an electric field across it and the degree of polarization directly depends on the applied strain. The mechanical work expended on a strained material gets stored as elastic energy. Polarization fields developed in the material results in potential generation. Piezoelectric materials are widely being used in the form of piezo ceramics (PZT), thin films (sputtered ZnO, AlN), polymeric materials (PVDF) and single crystals (quartz). As fabrication of magnets and coils in MEMS is practically difficult; therefore, electromagnetic type energy harvester is not suitable. Fabrication of capacitive type is suitable in MEMS but requires initial voltage for device operation. Piezoelectric type is best suitable for vibration energy harvesting due to its simple design, operation and because of ease of fabrication in MEMS technology. Piezoelectric energy harvesters are realized by

cantilever structure fixed at one end and free at the other end having seismic mass as shown in Fig. 1.6 [52].

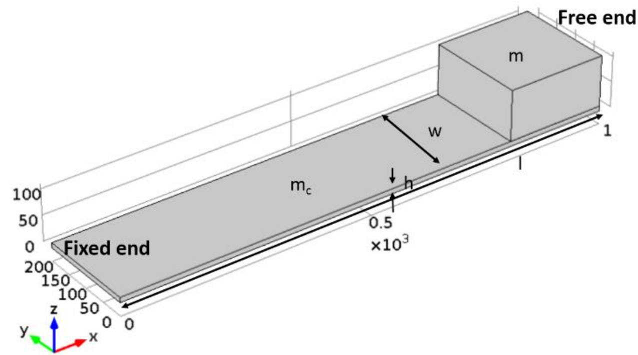

Fig. 1.6 Cantilever beam fixed from one end and seismic mass at other [52].

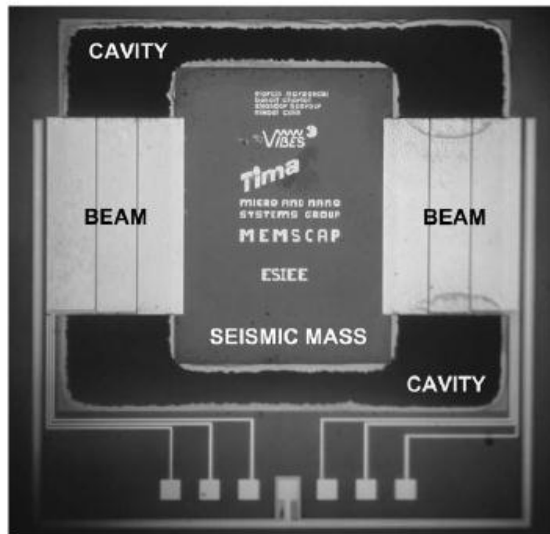

Fig. 1.7 Fabricated guided two-beam device Marzencki et al. [53].

In order to have a high sensitivity, the stiffness (spring constant k) of the cantilever has to be very low. However, lower stiffness of the cantilever makes it fragile. Therefore, guided beams fixed from both ends and having seismic mass at the center have been used for better stability and reliability as shown in Fig .1.7 [53].

Cantilever structures are modeled as spring mass damper system having a fixed resonance frequency. This resonance frequency depends on the physical parameters of

cantilever such as length ‘l’, width ‘W’, thickness ‘t’ and Young’s modulus ‘E’ of the cantilever beam and weight of the seismic mass attached with the cantilever structure. The spring constant of the cantilever is therefore given by equation 1.4 [54].

$$k = \frac{F}{x} = \frac{3EI}{l^3} = \frac{EWt^3}{4l^3} \quad 1.4$$

The first criterion to generate maximum output power from the energy harvester is to tune the resonance frequency of the cantilever beam to the frequency of ambient vibration. The resonance frequency of the cantilever depends on spring constant (k) of the beam and seismic mass (m) at the center as given by equation 1.5 [54].

$$f = \frac{1}{2\pi}\sqrt{\frac{k}{m}} \quad 1.5$$

A cantilever type piezoelectric energy harvester should operate in resonance with the ambient frequency for optimal output; otherwise the power harvested will drastically reduce and will not be able to drive sensor nodes [55]. Piezoelectric energy harvesters must be designed and operated in low-frequency region as ambient vibrations available in environment are in low-frequency range. Therefore, lower frequency operation and resonance with ambient frequency vibration are the key parameters in successful operation of cantilever type piezoelectric energy harvesters. The main advantage of P-VEHs is the compatibility of fabrication of cantilever structures in MEMS technology [56]. The cantilever structure is shown in Fig. 1.6 is fabricated on silicon substrate using bulk micromachining to realize proof mass and piezoelectric layer deposited on the front side with bottom and top electrodes. Ambient vibration displaces the cantilever from the free end which generates stress on the fixed end. The stress in the piezoelectric layer generates charge in the piezoelectric layer which results in the electric potential. The potential generated is harvested from bottom and top electrodes [57-59].

Reliability and stability can be ensured by making use of a guided beam design in which the cantilever beams are fixed at one end and supported with a seismic mass at the other end as shown in Fig. 1.7 [53]. The fixed nature of the beams leads to lower residual stress while vibrating, compared to single cantilever based designs, enhancing the device

stability and reliability. Guided beam structure gives lower displacement which reduces the possibility of collisions with the encapsulation layer, thereby preventing beam fractures improving the device reliability and stability. Guided two-beam piezoelectric energy harvester has been designed and fabricated by Marzencki et al. [53] and Wang et al. [60]. However, fabrication and testing of guided four-beam piezoelectric energy harvester and comparison with two-beam P-VEH have not been investigated by the researchers so far. The previous split electrode designs such as discussed by Marzencki et al.. [53] deployed the set of electrodes on almost complete beam length. Therefore, length and position optimization of the electrodes has not been reported in the literature. Square shape seismic mass has been used in the past literature [61] and investigation on different shapes of seismic mass has not been carried out. Furthermore, design and testing of guided beam P-VEH for lower frequency range below 500 Hz has not been reported so far.

1.5 Motivation

In the current scenario, there is a vast requirement for MEMS-based energy harvesters in WSNs. Some applications include structural health monitoring, tire pressure monitoring system, remote weather stations and many others. All these applications has a vibration frequency range from few Hz to KHz range as discussed earlier. Thus, to provide a clean and an unending energy source which can power these MSNs is the motivation of this work Therefore, we aim at design and development of MEMS based piezoelectric type energy harvester.

1.6 Objective of Thesis

This thesis aims at Design and Development of Guided Beam type Piezoelectric Energy Harvester for low frequency operation. The device is designed and developed for vibrations range from 10 – 600 Hz, for applications such as Structural health monitoring of rotor blades in a chopper. Specific tasks involved in this work are:

(i) Comparison of a single beam, multi-beam and guided beam type P-VEH for low resonance frequency range up to 600 Hz.

(ii) To investigate the effect of shape of seismic mass on the electric potential generated by piezoelectric energy harvester using COMSOL Multiphysics®.

(iii) Design, FEM simulation and comparison of guided two-beam and guided four-beam type piezoelectric energy harvester using COMSOL Multiphysics®.

(iv) Fabrication of guided two-beam and guided four-beam type P-VEH in MEMS technology.

(v) Testing and Characterization of guided two-beam and guided four-beam type P-VEH for low frequency operation.

1.7 Research Methodology

Firstly, the single beam cantilever, multi-beam cantilever (array) and guided beam type piezoelectric energy harvesters will be designed and compared. Design suitable for low frequency with stable operation is obtained. Secondly, the effect of shape of seismic mass on potential generated by piezoelectric energy harvester is investigated using COMSOL Multiphysics®. The suitable design which gives better results is selected for further design and device fabrication. The selected design (guided beam) is further investigated on different parameters such as displacement, von-Mises stress and electric potential. Effect of electrodes on resonance frequency is also investigated and, optimization of position and dimension of electrodes is performed. Thirdly, the optimized designs are fabricated in MEMS technology and the device will be tested, characterized and compared.

1.8 Contributions

This research work has the following contributions:

(i) Investigation on different shapes of seismic mass has led to the conclusion that a cantilever type piezoelectric energy harvester having triangular shape seismic mass generates a higher electric potential of 53.3 mV as compared to a rectangular shape seismic mass which generates a potential of 52.4 mV.

(ii) Guided two-beam and four-beam type piezoelectric energy harvester having pyramidal shape seismic mass has been designed and investigated. Optimized

dimensions of split electrodes and pyramidal shape seismic mass have been used in the guided two-beam and four-beam design for improved response. The optimized split electrodes give a reduced resonance frequency by 4.2% when compared with previously used electrode pattern ensuring maximum potential generation for guided two-beam structure.

(iii) Fabrication of the guided two-beam and four-beam piezoelectric energy harvester has been carried out simultaneously. Reduction of the beam thickness for both devices utilizing beam thinning process has been done using DRIE. Lower the beam thickness, lower is the resonance frequency of the device. Laser Doppler Vibrometer (LDV) has been used to experimentally obtain the resonance frequency of the devices which comes at 466 Hz and 515 Hz for two-beam and four-beam device respectively. The resonance frequency reported is the lowest resonance frequency achieved with beam thinning process reported till date. Lower resonance frequency enables the device operation in very low-frequency range up to 10 Hz.

(iv) Testing and characterization of the packaged two-beam and four-beam devices were carried out. Sensitivity of both, two-beam and four-beam devices are experimentally measured on SPEKTRA SE-10 vibration exciter setup. The PCB packaged two-beam and four-beam devices under test exhibit net sensitivities of 1.5089 mV/m/$s^2$and 1.0231 mV/m/s^2respectively in the low-frequency region of 10 to 1000 Hz.

1.9 Organization of the Thesis

The organization of the thesis is as follows:

Chapter 2 reports the literature survey, which gives the current status of the cantilever based piezoelectric type energy harvesters, current design issues for the device fabricated in MEMS technology. Moreover, it helps in identifying the problem statement for the thesis. Several papers were reviewed, papers which find direct application to the topic are selected, studied and discussed.

Chapter 3 Piezoelectric type vibration energy harvester is designed, modeled and compared using FEM COMSOL Multiphysics®. Analytical equations describing displacement, resonance frequency are presented. Effect of shape of seismic mass on potential generated by cantilever type piezoelectric energy harvester is investigated.

Chapter 4 presents the simulation-based analysis of guided beam type piezoelectric energy harvester. COMSOL Multiphysics® simulation tool is used to simulate guided two-beam and four-beam type piezoelectric energy harvester. Various data sets of the two-beam and four-beam structure for different input acceleration range are produced for displacement, stress, potential generated, resonance and results are compared. Dimensions of split electrodes have also been optimized which gives reduced resonance frequency.

Chapter 5 presents fabrication of guided two-beam and four-beam P-VEH using MEMS fabrication technology. Bulk-micromachining is done using Tetra Methyl Ammonium Hydroxide (TMAH) CMOS compatible 25 wt.% wet etching to realize pyramidal shape seismic mass and deep reactive ion etching (DRIE) is done from front side to release two-beam and four-beam device. A piezoelectric layer of Zinc-oxide (ZnO) is sandwiched between top and bottom electrodes to collect charge generated under external vibrations.

Chapter 6 presents characterization of the guided two-beam and four-beam P-VEH. Structural characterization is done in which, phase orientation of materials is done using X-ray diffraction (XRD), surface morphology is obtained using Scanning electron microscope (SEM), and the topological view is obtained with Atomic force microscopy (AFM). Dynamic characterization is performed using a laser Doppler vibrometer to experimentally obtain the resonance frequency of the two-beam and four-beam device. Finally, vibration bench testing is done for measurement of electric potential and sensitivity for the two-beam and four-beam device. The variation of the voltage output with acceleration and frequency is also tested experimentally.

Chapter 7 gives the conclusion of the work presented in the thesis along with the future scope of the work.

Chapter 2

Literature Review

The research objective is design and development of a MEMS-based cantilever type P-VEH. As already discussed in the introduction, MEMS-based P-VEHs are suitable for WSNs. Therefore, in this chapter literature review focused on MEMS-based P-VEHs has been done. The keywords on which literature review has been done are: cantilever type piezoelectric vibration energy harvester, vibration energy harvesting and Piezoelectric-Vibration energy harvester (P-VEH).

A MEMS-based P-VEH can be realized by utilizing a cantilever structure free from one end and fixed at the other. Piezoelectric layer is sandwiched between the top and bottom electrodes. Displacement of the cantilever induces stress in the proximity of the fixed beam end which generates charge in the piezoelectric layer. Charge generated gets collected through the electrodes. A seismic mass deployed at the free end effectively reduces the resonance frequency of the piezoelectric energy harvester.

William and Yates [41], in 1996, presented first vibration energy based micro-electric generator. Vibration energy harvester has been modeled as a spring-mass damper system of second order and associated with a single degree of freedom (Fig. 1.3, chapter 1). The relative displacement or mechanical strain in the system results from the transmission of vibrations by the inertial frame to m, the suspended inertial mass via k and b, the spring and damper respectively. The device proposed in this paper generates power of 100 μW at 330 Hz and 1 μW at 70 Hz giving a displacement of 50 μm.

Jones et al. [62], in 2001, developed a single beam cantilever type piezoelectric energy harvester. They used thick film piezoelectric technology in the production of electrical power from environmental vibrations by developing an inertial generator. Steel substrate of 100 μm thickness was used on which, piezoceramic thick-film of Lead Zirconate Titanate (PZT) having a thickness of 70 μm has been deposited. The device has an

experimental resonance frequency of 80.1 Hz and maximum output power delivering capability of 2.1 μW.

Shahruz [63], in 2006, designed array of cantilevers having different length, width with different seismic mass at the end as seen from Fig. 2.2. As already discussed, a single beam cantilever operates as a spring-mass damper, therefore, the output at resonance is maximum and almost zero otherwise. Therefore, an array of cantilever that performs energy scavenging is deployed that acts as a band pass filter. Individual cantilevers get excited for a particular frequency alone, so the array of cantilevers generates output for a range of frequencies thereby acting as a band pass filter. The main advantage of this system is that peak output is maintained for a wider range of frequencies as shown in Fig. 2.2 (b). The dimensions of the cantilevers have been selected in such a way that the resonance frequencies are close with each other giving maximum output for wider frequency range. However, as the number of cantilevers is increased and only one cantilever operates at a time this system gives a low volume to output ratio.

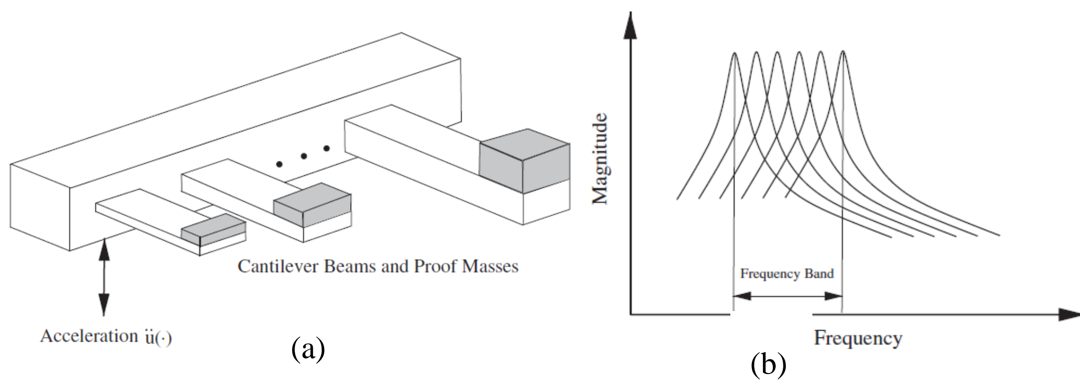

Fig. 2.1 (a) An array of cantilever beams acting as band pass filter: the beam dimensions and the proof masses at the tips are chosen in such a manner that the array acts as band-pass filter allowing a certain frequency range pass through. (b). The pass band frequency [63].

Fang et al. [64], in 2006 developed a P-VEH using UV-LIGA technology. In this work, composite cantilever with nickel metal mass has been fabricated. A PZT layer of 1.64 μm

is sandwiched between the bottom and top electrodes of Titanium/Platinum. The device resonates around 608 Hz and generates power output of 2.16 mW.

Marzencki et al. [65], in 2007, designed and fabricated P-VEH using AlN piezoelectric film in d31 mode for very low amplitude vibrations. The device resonance frequency is found to be 214 Hz. When an input acceleration 0.126 g is introduced the device generates a maximum power of 0.55 µW.

Huan Xue et al. [66], in 2008, demonstrated an effective approach of integrating many piezoelectric biomorphs (PBs) in the design and implementation of a broadband piezoelectric energy harvester. Parallel and series connections of the bimorphs cantilevers were investigated. The series connection found to increase the frequency bandwidth of the system whereas the parallel connection shifts the frequency bandwidth to the dominant frequency domain. Numerical analysis were performed on the two connections and a mixed approach i.e. combination of series and parallel bimorph cantilevers was proposed for optimal output.

Muralt et al. [67], in 2009, fabricated and characterized a cantilever-based P-VEH having a rectangular shaped seismic mass at its tip. A thick PZT (2 µm) layer was deposited on silicon substrate (5 µm) having inter-digitated electrodes were designed for higher voltage output. When excited with an input acceleration of 2 g maximum output power of 1.4 µW along with maximum output voltage of 1.6V has been achieved. The fabricated cantilever resonates at 870 Hz.

Lee et al. [68], in 2009, designed and fabricated P-VEH based on d33 and d31 modes. High quality and efficient PZT thin films of thickness up to 28 µm have been deposited using aerosol deposition method on silicon cantilevers. At 2.5 g input acceleration d31 mode gives an output power of 2.765 µW. The device resonance frequency is found to be 255.9 Hz. Similarly, the d33 mode gives a peak output power of 1.288 µW at 2g input acceleration. Resonance frequency of the device here is 214 Hz.

Marzencki et al. [53] in 2009, designed and developed clamped-free beam with one fixed end and the other free, and clamped-clamped beam or guided two-beam structure where both the ends are fixed and has a seismic mass at the center. The designed clamped-free

beam based device has seismic mass of length 800 μm and thickness of 450 μm. The beam length used is 400 μm. The resonance frequency of this structure is 1370 Hz. The fabricated device has 1 μm thick AlN layer sputtered using dc-reactive magnetron sputtering. Aluminum top electrode is used for charge collection. At input acceleration of 1g the maximum voltage generated is 0.42 Volts and maximum power generated is 0.1μW. A clamped–clamped structure with two-beams having width 2000 μm and length 1200 μm, a seismic mass having length width and thickness of 2200 μm, 3000 μm and 450 μm respectively are connected at the center. The device has a resonance around 1800 Hz and shows a non-linear behavior as compared to clamped – free structure. The device non-linearity is used for frequency adaptability from 1800 to 2450 Hz at 2g. Around resonance, the device generates power of 8.269 nW at an input acceleration of 1g. The clamped-clamped structure has a non-linearity which results in frequency adaptability of 36%. Clamped-clamped beam structure is very stable and reliable in high amplitude vibrations due to its ability to withstand higher stress, therefore, this structure is highly suitable for industrial applications where there is abundance of high amplitude vibrations which the structure will have to withstand.

Hirasawa et al. [69], in 2010, also developed P-VEH using AlN piezoelectric film. The device resonance frequency is 857 Hz and when an input acceleration of 1g is applied it generates a maximum output of 0.18 μW.

Elfrink et al. [70], in 2010, designed and fabricated an AlN based P-VEH and used vacuum packaging at the wafer-level. Pt (Platinum) bottom electrode, sandwiched AlN piezoelectric layer and Al (Aluminum) top electrodes were deposited and patterned. The device tested generates 17 μW of power at 0.64 g input acceleration and resonance frequency of 353 Hz. Packaged device generated 32 μW of maximum output power whereas the same unpackaged device generated 10.2 μW of power. Due to vacuum packaging the damping effects of air has been reduced which results in higher device output.

Blystad et al. [71], in 2010, designed a unimorph cantilever type P-VEH for random vibrations. The base of the cantilever is of Silicon, AlN is the piezoelectric layer and metal top electrode for collecting charge. Mechanical stoppers and power conditioning

circuit were designed and simulated. It was observed that maximum power level varies when different power conditioning techniques are used. The mechanical stopper models used to affect the bandwidth of the system. The elastic stopper model used increases the bandwidth of the system. This paper designed and simulated cantilever structure with different power conditioning circuit with and without a mechanical stopper in a random vibration environment.

Park et al. [72], in 2010, presented fabrication as well as characterization of a P-VEH in d33 piezoelectric mode. Here thin films of PZT were deposited by sol-gel spin-coating method. The device generated a maximum output power of 1.1μW when a load of 2.2 MΩ is considered for an input applied acceleration of 0.39 g. The device resonance frequency is 528 Hz. The device utilized interdigitated electrodes to harvest energy from d33 mode of the piezoelectric layer.

Morimoto et al. [73], in 2010, fabricated piezoelectric energy harvester by depositing PZT film on steel cantilevers ensuring higher energy conversion efficiency and robustness. Thin films of PZT were deposited on Pt/MgO substrates using RF-magnetron sputtering. The fabricated cantilever, without using a seismic mass at the cantilever tip resonated at 126 Hz. At an input excitation acceleration of 5 m/s^2, the fabricated device generated an output power maximum of 5.3μW with a load of 50 kΩ.

Durou et al. [74], in 2010, designed and developed a piezoelectric energy harvester with cantilever structure having a resonance frequency of 76 Hz. The device generated power of 13.9 μW at an input acceleration 0.2 g.

Hu et al. [75], in 2011, investigated the effect of strain gradient on a cantilever bimorph P-VEH. The strain on the cantilever structure tends to increase the natural frequency of the PB. However, it effectively improved the output power density of the P-VEH. It has been observed that the strain-gradient coupling coefficients tend to induce a frequency shift to the PB operation thereby influencing its performance.

Chang et al. [76], in 2011, designed a piezo-elastic generator for harvesting vibration energy generated by computer hard disk drives. Polyvinylidene fluoride (PVDF) layer of 25 μm thickness was used as a piezoelectric layer. Harvester having different modes of

deformation from few hertz to kilohertz were designed and fabricated. A maximum power of 0.55 W from the energy harvester has been achieved.

Karami et al. [77], in 2011, designed and developed unimorph cantilever type P-VEH. Total 24 unimorphs were fabricated using different PZT-5H, PZT-5A piezo-ceramics. The cantilevers have a resonance frequency from 500 – 600 Hz. The current output ranges from 0.1 to 1 A and the maximum power extracted was 100 μW.

Liu et al. [78], in 2011, designed and fabricated a cantilever-based P-VEH for low-frequency operation. Parallel cantilevers are connected with a heavy silicon seismic mass at one end and fixed from the other. A thick 3 μm PZT layer is sandwiched between Platinum/Titanium electrodes. The device has an operation bandwidth of 17 Hz i.e. from 30 – 47 Hz. Maximum power generation of 51.3 nW has been reported in this paper.

Hajati et al. [79], in 2011, designed and fabricated doubly clamped beams structure that is fixed at both the ends and having a proof mass at the beam center. This design utilizes the stretching strain of the beams, therefore, giving an improvement in the bandwidth and the power density. A PZT layer of 0.27 μm thickness is deposited over the beams. A thousand pairs of inter-digitated electrodes are defined on top of the PZT layer, to harvest potential in d33 mode. At 1300 Hz, the fabricated device generates a maximum power of 22 μW across the optimized load resistance of 290 kΩ.

Lei et al. [80], in 2011, designed and developed a PZT based P-VEH. The device resonates at 235 Hz. The maximum output was 14μW when 1g excitation is applied.

Defosseux et al. [81], in 2012, designed and fabricated a clamped single beam P-VEH for low amplitude vibrations. The device resonates at 200 Hz when an acceleration lower than 0.25 g is applied. Initially, the 0.1 μm Mo bottom electrode was sputter deposited followed by which DC-pulsed reactive sputter deposition of 2 μm thick AlN was done. 0.1 μm thick sputter deposited Pt forms the top electrode. At input excitation of 0.25g the developed device harvests a peak power of 0.62 μW and resonates at a frequency of 214 Hz.

Xu et al. [82], in 2012, presented a PZT thick film PB (with two piezoelectric layers) P-VEH having a proof mass made of silicon. The coupling coefficient of the system was

seen to increase due to presence of two piezoelectric layers and thus the output power density increases significantly. At an input acceleration of 1g, the harvester has maximum output of 37.1 μW.

Kanno et al. [83], in 2012, designed and fabricated cantilever based P-VEH using different piezoelectric materials. Thin films of Pb-free Sodium Potassium Niobate $(K,Na)NbO_3$ (KNN) and $Pb(Zr,Ti)O_3$ (PZT) were deposited on Platinum/Titanium/Silicon substrates via RF-magnetron sputtering. The maximum output power of the device with KNN/Si is 1.1 μW and that of PZT/Si is 1.0 μW. This paper compared the two piezoelectric materials KNN and PZT and found that both devices have around equal power output. Therefore, a lead-free material KNN can be used which generated equal output without having lead contamination.

Ahmad et al. [84], in 2012, designed and developed a cantilever-based P-VEH for free-falling droplets. The harvester is a fixed-free end cantilever having five layers of PZT stacked on top of one another. The cantilever has a resonance frequency of 315.15 Hz. For a moderate rain intensity of 230 drops per second an energy generation of 400 μJoule has been reported.

Wang et al. [60], in 2012, designed and fabricated an optimized clamped-clamped beam P-VEH for lower frequency vibrations. The mass beam length is 3780 μm and the truss beams length is also 3780 μm. Pt, AlN and Al layers are sputter deposited sequentially and are patterned in the form of capacitors. DRIE is used to define the two-beams and for releasing the structure. The fabricated device resonates at 694 Hz. When an acceleration of 1.2g is used for excitation, the maximum output power generated by the structure is 10 μW from one set of capacitor. The device exhibits a tuning range of 3 Hz.

Sang et al. [85], in 2012, designed and developed cantilever based hybrid vibration energy harvester for WSN. A cantilever beam having two piezoelectric layers with a magnet place at the tip of the cantilever is designed. The magnets on the tip and the bottom electrodes accelerate the vibration and also adjust the cantilever resonance frequency. The resonance frequency of the energy harvester is 50 Hz. At 0.4 g input acceleration, 10.7 mW power has been generated at a load end of 50Ω.

Wang et al. [86], in 2012, designed and developed cantilever type P-VEH having metal substrate. A 50 μm thick layer of stainless steel is used as a base of the cantilever. Titanium/Platinum (30/200 nm) films were sputtered on steel for bottom electrodes. PZT thick film of 4 μm is deposited using sol-gel process. Al top electrode was deposited through e-beam evaporation. Finally, a copper proof mass gets attached at the cantilever free end. The device has a resonating frequency of 89 Hz and an output power of 15.4 μW has been reported.

Tang et al. [87], in 2012, designed and developed cantilever based P-VEH. Chrome/Gold (20 nm/150nm) were deposited to form primary electrodes. PMN-PT piezoelectric layer was deposited having 10 mm thickness. Chrome/gold was again sputtered to form the top electrode. A nickel-seismic mass is introduced at the cantilever beam tip. Resonance frequency of 237.4 Hz and a maximum power generation of 2.704 μW has been reported in the paper.

Berdy et al. [88], in 2012, designed and developed piezoelectric energy harvester. PZT layer is sandwiched between nickel electrodes. The fabricated device resonates at 50 Hz. Maximum power density of 105 μW at load resistance (380 KΩ) end has been reported in this paper.

Elvin et al. [89], in 2013, investigated vibration energy harvesting due to human motion suitable for wireless implants. Human foot motion was deeply investigated using multi-axis accelerometer giving the displacement and the frequency. For a device, that can operate for a high acceleration of 30g would generate a power of 28 mW. Effect of electromechanical coupling coefficient and mechanical tuning have been investigated in this paper. A higher coupling coefficient and tuning results in increased output power.

Yun et al. [90], in 2013, designed and developed a woven piezoelectric energy harvester for wireless portable devices. Polymer threads were used in the column and the piezoelectric film weaving them in the row were designed. Due to stretching and contracting motion charges are generated and collected through polymer patches. At an operation frequency of 8 Hz due to continuous contraction and stretching a peak power generation of 0.63 mW/cm^2 has been reported.

Gao et al. [91], in 2013, designed and developed cantilever based flow energy harvester. PZT layer 127 µm thick is used in designing the energy harvester. The lowest resonance frequency achieved was 20.7 Hz. A change in flow generates a voltage fluctuation of 1V has been reported in the paper.

Usman et al. [92], in 2014, designed and developed energy harvester for acquiring, processing and transmitting the Electrocardiogram (ECG) data in a WSN. A cantilever structure having seismic mass at the end is deployed to harvest energy. PZT layer is sandwiched between Platinum electrodes. The proposed design when integrated into a system can harvest µW of power from heartbeats having a resonance frequency 39 Hz and acceleration 0.3 m/s^2.

Alsuwaiyan et al. [93], in 2014, presented an approach to harvest energy from low-frequency vibrations. Three cantilever type P-VEH having different resonance frequency of 40, 45, 53.4 Hz has been used. The maximum power generation of 440 µW has been reported in this paper.

Xu et al. [94], 2015, designed and fabricated clamped-clamped beam device for harvesting energy from low-frequency and low-amplitude vibrations. The device testing is done shows operating frequency in the range 50Hz to 150Hz at an input acceleration of 0.2g. Both macro prototype and MEMS device has been presented in this paper.

Saadon et al. [95], in 2015, designed a cantilever array for low-frequency operation range of 67-70 Hz. A PZT layer of 1.2 µm thickness is sandwiched between 0.1 µm thick Platinum electrodes. Input acceleration range of 0.2 -1.3 g maximum power generation of 6.8 µW has been reported in this paper.

Emamian et al. [96], in 2016, designed and developed a piezoelectric energy harvester using a screen printing technique. The structure consists of a thick PVDF layer of 12.5 µm sandwiched between METglas electrodes. The device has a first resonance frequency of 54 Hz. Across a load of 1MΩ maximum power generation of 0.28 µW has been reported in the paper.

Minh et al. [97], in 2017, designed and developed AlN based energy harvester on Titanium foils. A 4 µm AlN thick film is deposited over Titanium foil. Chrome/Gold was

deposited to form top electrodes. The fabricated device resonates at a frequency of 645.3 Hz. Maximum harvested power of 13.1 μW has been reported in this paper.

Wang et al. [98], in 2017, designed and characterized a double fork P-VEH, The designed harvester has first three resonance frequencies of 21, 47 and 91 Hz respectively. The bandwidth of the designed energy harvester is 8 Hz at an input acceleration of 1g.

Jackson et al. [99], in 2018, designed and developed a piezoelectric energy harvester for powering a pacemaker. AlN of thickness 0.45 μm is sandwiched between Titanium and Aluminum to form bottom and top electrodes. The device has a resonance at 28.5 and 678 Hz. Maximum power of 17 μW at 678 Hz has been reported in this paper.

Wen et al. [100], in 2018, designed and developed P-VEH for wind energy. Cantilever-based structure is designed which is actuated using magnets. The dimensions of the cantilever are length 100 mm and a thickness of 0.4 mm. The total power generated from the energy harvester at 360 rpm is 1.38 μW.

Nabavi et al. [101], in 2019, designed and developed a non-linear wideband P-VEH. The designed structure has a doubly clamped beam with three seismic mass. The device has a wideband operation of 59 Hz from 227 - 286 Hz. The power density of the device reported is 595.12 $\mu W.cm^3.m^{-2}s^4$.

Wen et al. [102], in 2019, designed and developed a novel integrated multi-stage energy harvester. Multi-objective genetic algorithm has been used to optimize the device dimensions. Across a matched load the device exhibits peak power of 50.8 mW.

2.1 Discussion and Planning: The literature survey done states the suitability of cantilever-based P-VEH for WSNs. From the survey, the P-VEH can be broadly classified into three types on the basis of their structures (i) Single beam cantilever unimorph or bimorph structures free form one end and fixed at the other. (ii) Cantilever arrays with multiple cantilever elements connected in series or parallel. (iii) Clamped-Clamped/guided beam structures fixed at both the ends and having seismic mass attached at the center. The single beam cantilever structure has low resonance frequency and gives high output because of large displacement of the beam, however, large displacement makes device unstable and results in beam fractures. Cantilever array type structure gives

peak output for wider frequency range due to large number of cantilevers, however, only one cantilever operates at a time results in low volume to output ratio. Guided beam structure gives reliable and stable device operation due to the fixed nature of beams, however, fixed beams increases the resonance frequency of the structure. Considering high amplitude vibrations, guided beam structure type P-VEH is a preferred choice due to stable operation and suitability of fabrication in MEMS technology. Therefore, we have focused our work on guided beam type P-VEH. While doing literature survey on guided beam type P-VEH the following literature gaps were observed.

(a) Resonance frequency reported by Marzencki et al. [53] for guided two-beam structure is 1800 Hz and 694 Hz reported by Wang et al. [60]. Considering low-frequency vibrations below 500 Hz, the resonance frequency of the reported devices is relatively higher. Therefore, there is a need to optimize the fabrication technology in order to further lower the device resonance frequency.

(b) Guided two-beam structure utilizes a pair of split electrodes which harvests the tensile and compressive stress [53]. However, in previous designs, the split electrode is deployed on complete beams without optimizing the dimensions of the electrodes. Therefore, optimization of dimensions of split electrodes is necessary for maximum output with the lowest resonance frequency.

(c) Shape of the seismic mass is generally square on shape because it can be easily realized in MEMS technology using DRIE. Investigation on different shapes of seismic mass such as triangular shape, pyramidal shape has not been investigated. Therefore, effect of different shapes of seismic mass on potential generated by P-VEH needs to be investigated.

(d) Design and development of guided two-beam P-VEH have been reported [53, 60], however, design and fabrication of a guided four-beam P-VEH have not been reported so far. Therefore, design, fabrication of four-beam P-VEH needs to be investigated and has to be compared with its guided two-beam counterpart.

(e) Testing of the two-beam and four-beam P-VEH in very low frequency up to 10 Hz has not been reported as devices have higher resonance frequency. Therefore, low-

frequency testing of the devices has to be investigated experimentally to test the behavior of the devices in low-frequency domain.

As, it is clear from the theory of a piezoelectric vibration energy harvester, when a cantilever beam undergoes a vibration in tune with the ambient vibrational energy, it develops a stress in its both the surfaces, and if both or one of its surfaces are coated with a piezoelectric (PE) layer, this PE layer will also be stressed along with the surface and acquires an electric charge. In this way, electric charge is generated as a result of ambient vibration energy. It will generate a voltage if PE layer is in a closed electrical loop with a load. This activity of generating charge or voltage in a PE layer on top surface of a cantilever depends on the stiffness of the cantilever. Lower is the stiffness; higher will be the charge or voltage generation, i.e. higher sensitivity. It can be further improved by putting a proof mass at the free tip of the cantilever, but it makes cantilever fragile [53]. In order to have a robust structure, we have chosen a beam with the hanging mass at its center. This is called a two-beam guided structure. The structure will be even more stable if we take four-beams at right angles to each other with a common suspended mass at their tip. This is called a four-beam guided structure. In this work, we have taken these two structures for the design of our vibration energy harvester. Therefore, taking the above research gaps into consideration, we aim at Design and Development of guided two-beam and guided four-beam P-VEH for low-frequency operation.

Chapter 3

Design, Modeling and Comparison of Piezoelectric Energy Harvesters

A piezoelectric type energy harvester can be realized using cantilever type structures and can be fabricated using MEMS technology as discussed in the literature review. Three types of structures i.e. single beam cantilever structure, cantilever array structure and guided beam structure are prominently used in realization of MEMS-based piezoelectric type energy harvester. In this chapter, design, simulation and comparison on these three types of structures are reported. Based on stable operation and ease of fabrication an optimized structure is selected and further investigated.

3.1 Single cantilever structure

A single cantilever structure made up of piezoelectric material fixed from one end and free from other is designed which operates as a piezoelectric energy harvester. Due to external vibrations deflection in cantilever beam occurs at the free end which can be seen from Fig. 3.1

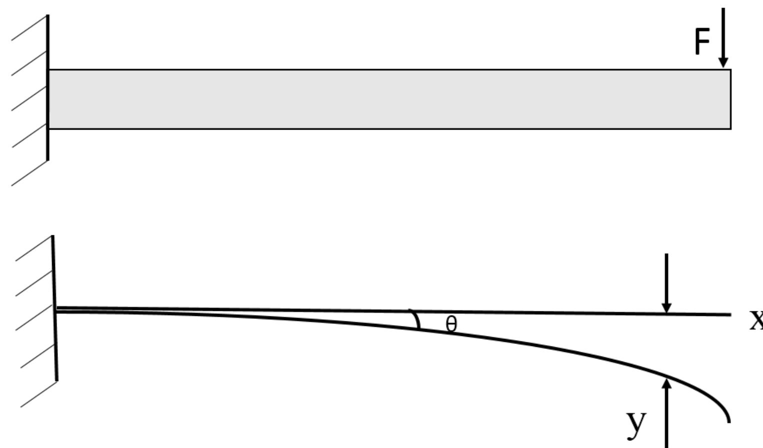

Fig. 3.1 Deflection of cantilever beam [43].

The general method for calculating the curvature of beam under small displacement is by solving a second-order differential equation of a beam given by equation 3.1[43].

$$EI\frac{d^2y}{dx^2} = M(x) \quad 3.1$$

where M(*x*) represents the bending moment at the cross section at location x and y the displacement at location x in μm and E is the Young's modulus measured in Pascal. The most common type of cantilevers are rectangular in shape [43]. The width and thickness of the rectangle cantilever is denoted by w and t, and the moment of inertia (I) with respect to neutral axis is $I = wt^3/12$.

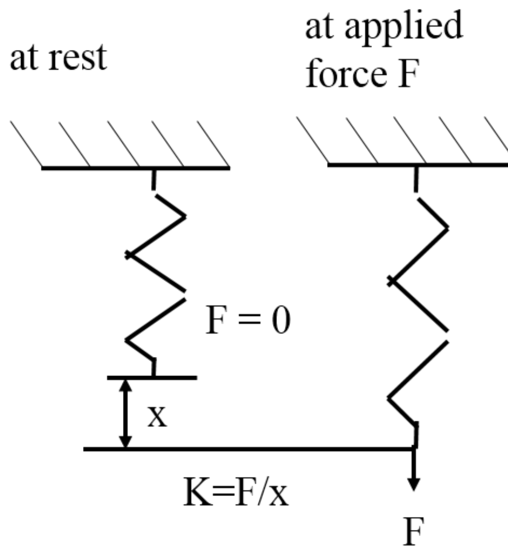

Fig. 3.2 Mechanical deformation of a coil spring under point loading force [41].

MEMS-based cantilever structures are characterized as spring mass systems. For a cantilever spring the general expression of a force constant is the force divided by the displacement as shown in Fig. 3.2. The free end of the beam will reach a certain bent angle 'θ' in degrees shown in Fig. 3.1, with the relationship between θ and applied force F in Newton given by equation 3.2 [43] where 'l' is the length of the cantilever beam in μm.

$$\theta = \frac{Fl^2}{2EI} \quad 3.2$$

The resultant vertical displacement of the beam is given by equation 3.3 [43].

$$x = \frac{Fl^3}{3EI} \tag{3.3}$$

The spring constant of the cantilever can thus be given by equation 3.4 [43].

$$k = \frac{F}{x} = \frac{3EI}{l^3} = \frac{Ewt^3}{4l^3} \tag{3.4}$$

The first criterion to generate maximum output power from the energy harvester is to tune the resonance frequency of the cantilever with the frequency of ambient vibration. The resonance frequency ‘f’ of the cantilever depends on spring constant ‘k’ of the beam and seismic mass ‘m’ at the center as given by equation 3.5 [54].

$$f = \frac{1}{2\pi}\sqrt{\frac{k}{m}} \tag{3.5}$$

As ambient vibrations are of low frequency, therefore the cantilever must have a low resonance frequency to match with ambient vibrations. Therefore, to reduce the resonance frequency of the cantilever a seismic mass m is placed at the end of the cantilever. The effect of seismic mass on the resonance frequency of the cantilever is investigated using COMSOL Multiphysics®. Two different cantilevers were designed one without seismic mass and the other with a seismic mass of dimensions 300 µm x 500 µm x 100 µm. The length, width and thickness of both the cantilever are 3500 µm, 300 µm and 10 µm respectively. The eigen frequency analysis is performed to obtain the resonance frequency of the cantilevers and the results are shown in Fig.3.3.

It can be seen from the Fig 3.3 that the free end cantilever without proof mass resonates at 1593.1 Hz whereas when a seismic mass is placed at the free end of the cantilever then the resonance frequency reduces to 764.05 Hz. Due to seismic mass the resonance frequency reduces by 829 Hz or by 52 % which is required to tune with low-frequency ambient vibrations. This is because the effective mass of the cantilever increases due to seismic mass. This statement also justifies equation 3.5. Another method to reduce the resonance frequency is to increase the length of the cantilever. As length increases, spring

constant k decreases which reduces the resonance frequency of the cantilever as seen from equation 3.4 and 3.5.

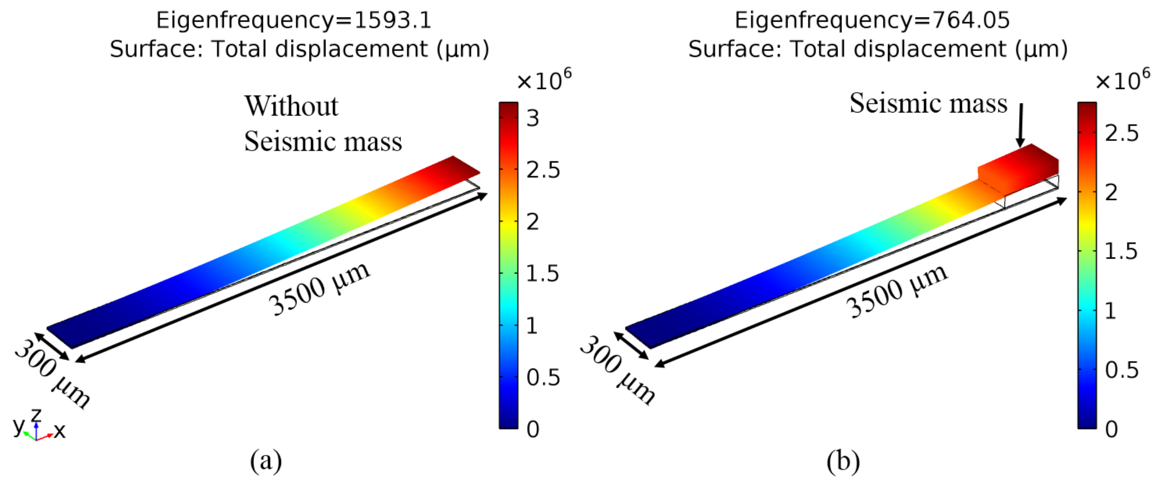

Fig. 3.3 (a) Resonance frequency of the free end cantilever is 1593.1 Hz. (b) Resonance frequency of the cantilever with proof mass is 764.05 Hz.

Therefore, the effect of variation of length of the cantilever on resonance frequency is also investigated. After initial iterations, length variation from 1600 μm to 2500 μm is selected as it gives the desired frequency range from 200 to 600 Hz. Three different thickness of seismic mass 10 μm, 15 μm and 20 μm are selected to further reduce the resonance frequency.

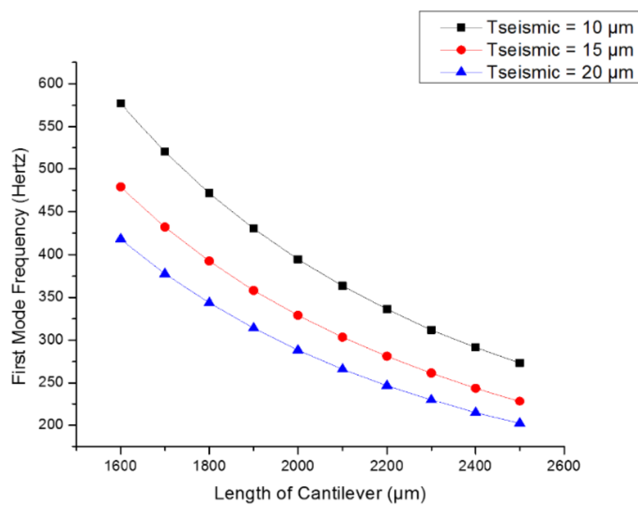

Fig. 3.4 Graph of resonance frequency vs. cantilever length.

The height of the seismic mass is selected from 10 to 20 μm because it can be easily electroplated during device fabrication. Fig. 3.4 shows the effect of increase in length and seismic mass on the resonance frequency of the cantilever structure. As length is increased from 1600 μm to 2500 μm for the seismic mass of 10 μm thickness, the resonance frequency reduces from 575 to 275 Hz and when seismic mass thickness is 20 μm the resonance frequency reduces from 425 Hz to 200 Hz. This can also be seen from the graph shown in Fig. 3.4 which also justifies equation (3.4) and (3.5). Therefore, the two main parameters that decide resonance frequency of the cantilever type energy harvester are the seismic mass 'm' and the length of the cantilever 'l'. These two parameters can be varied in order to tune with the ambient vibrations.

To further investigate the nature of displacement, stress and magnitude of electric potential generated, a cantilever structure having dimensions as length 2000 μm, width 400 μm thickness 10 μm with a proof mass at the end of 400 μm x 400 μm x 20 μm is attached and the structure is simulated using FEM simulator COMSOL Multiphysics® as shown in Fig. 3.5.

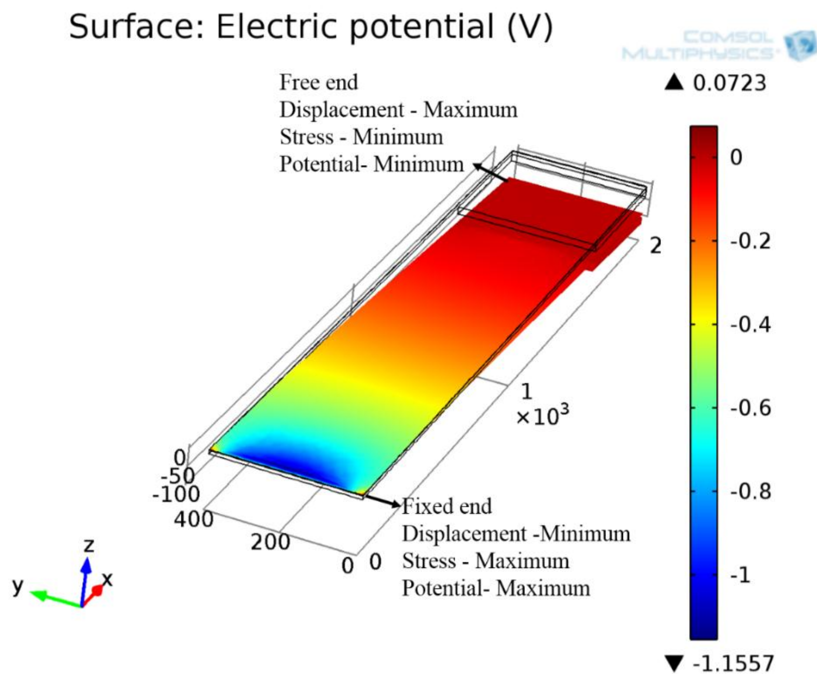

Fig. 3.5 FEM simulation of single beam cantilever

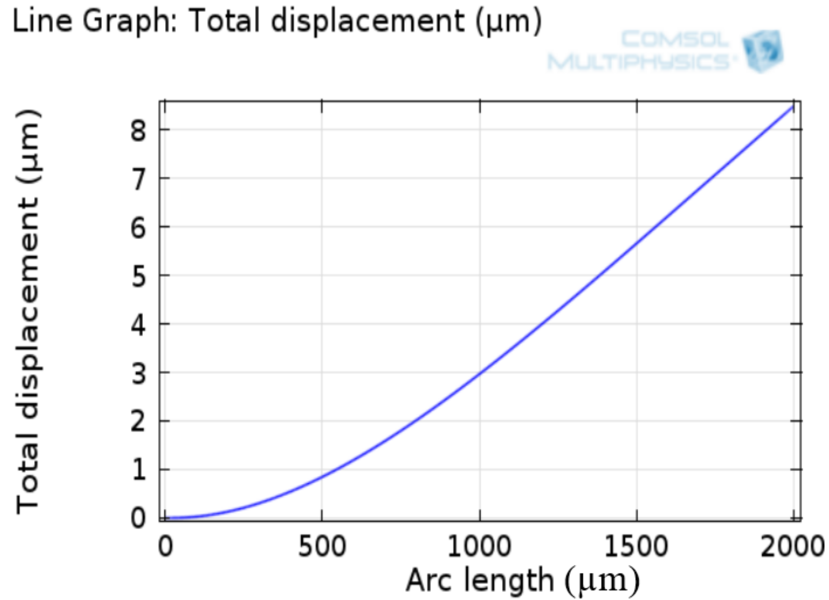

Fig. 3.6 Graph of displacement of the cantilever from fixed end towards free end.

Total displacement graph of the single cantilever structure is shown in Fig. 3.6. It can be seen that at the fixed end i.e. 0 μm the displacement is minimum because the cantilever is fixed from that end and as we move towards the free end the displacement increases, maximum displacement is 8.5 μm at the free end.

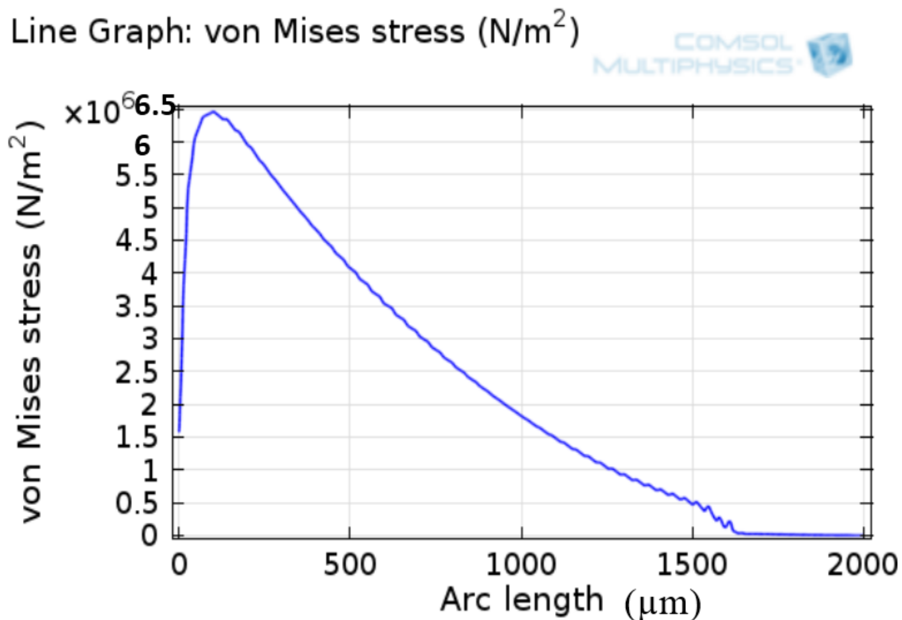

Fig. 3.7 Graph of von-Mises stress generated from fixed end towards free end.

Stress along the length of the cantilever is generated from fixed end towards free end along the x-axis. The region of maximum displacement has minimum stress due to free movement of cantilever whereas at the fixed end the stress is maximum due to minimum displacement. Fig. 3.7 gives the distribution of von-Mises stress along the cantilever length. At the fixed end the stress equals 6.5 x 10^6 N/m^2 and is maximum which reduces to minimum value as we move towards free end.

Electric potential is generated along the piezoelectric layer due to stress along the length of the cantilever length. Maximum stress at the fixed end generates maximum electric potential whereas minimum stress at free end results in minimum electric potential. Fig. 3.8 gives the distribution of the electric potential along the length of the piezoelectric layer. At the fixed end the electric potential is equal to 0.6 volts and is maximum and (negative sign for polarity) which reduces as we move towards the free end of the cantilever. The electric potential will be maximum where there is maximum stress.

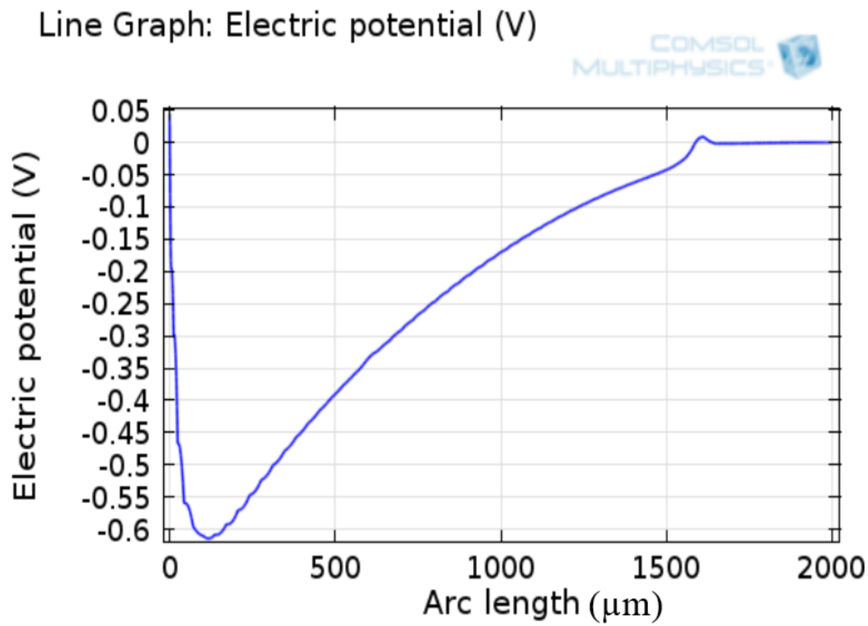

Fig. 3.8 Line graph of electric potential generated from fixed end towards free end.

3.2 Cantilever Generator array

A cantilever type P-VEH behaves as a spring mass damper system i.e. resonating only at a single frequency. Sharuz [63], in 2006, proposed a methodology of designing a

generator array by connecting cantilevers of different lengths which can increase the operation frequency range of the energy harvester. We further investigate this by designing a cantilever array structure is simulated having three cantilever beams with length 2000, 2100 and 2200 µm. All the cantilevers have the same thickness of 2 µm and width 200 µm with a proof mass of length 200 µm, width 200 µm and thickness 10 µm. First cantilever having length 2200 µm resonates at a frequency of 681.061 Hz as shown in the Fig. 3.10. At frequency of 867.671 Hz, cantilever of length 2100 µm resonates whereas at 1215 Hz cantilever of length 2000 µm resonates. The cantilever having length 2200 µm, gives a maximum displacement as 5.7351 µm in Z-axis as shown in Fig. 3.9. The second and third cantilever gives zero displacements. Similarly, the second cantilever with length 2100 µm gives a displacement of 5.80 µm and third cantilever having length 2000 µm gives displacement of 6.1 µm.

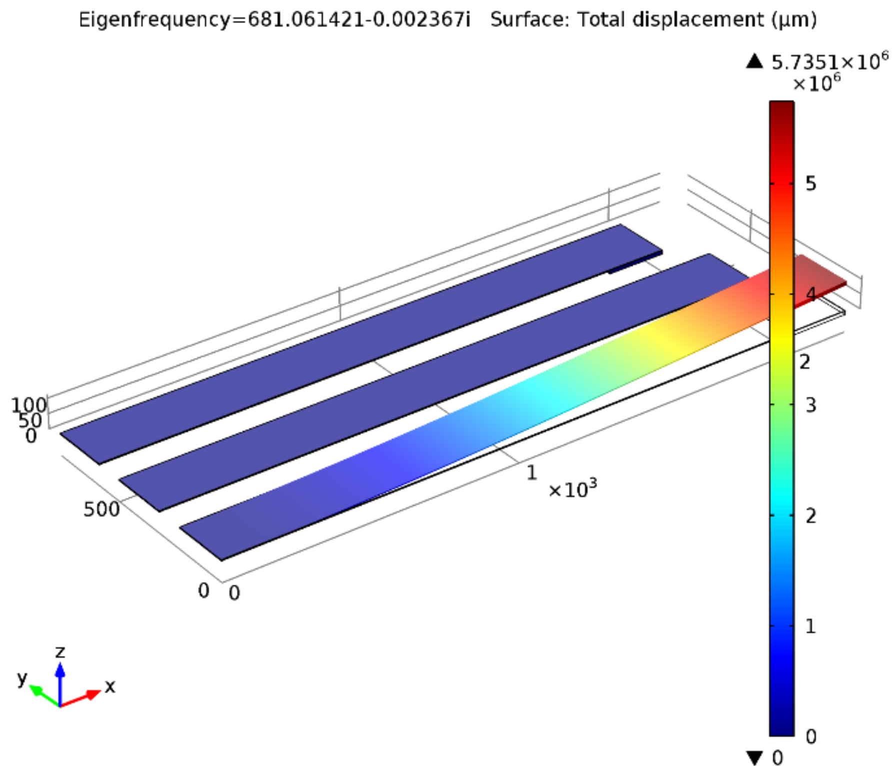

Fig. 3.9 Generator array of three cantilevers

The above design of cantilever array has three elements of different lengths from 2000 to 2200 µm. The design gives an operation for frequency ranging from 681 Hz to 1215 Hz.

Therefore, a wide operation range is achieved using cantilever array type P-VEH. However, cantilever array design has multiple cantilevers which increase the cost of fabrication of the energy harvester. As in this case, only one cantilever is excited at a single frequency, the rest two cantilevers generate no or residual output. Due to this reason, the cantilever array type P-VEH has very low output to volume ratio. During device fabrication of cantilever array type P-VEH releasing of multiple cantilevers having different dimensions is a challenge.

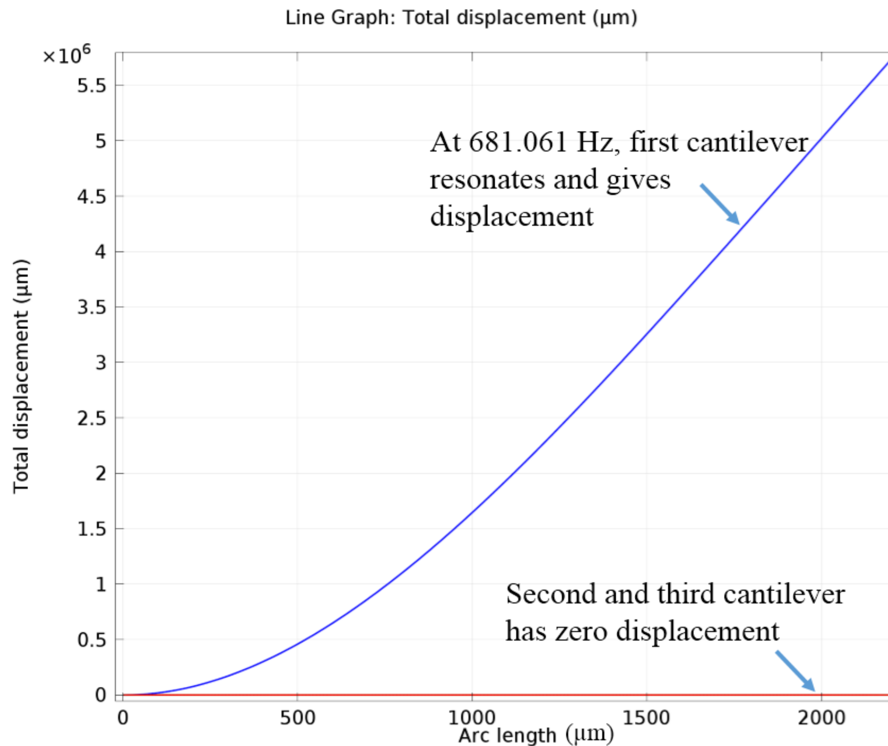

Fig. 3.10 Line graph of displacement of Cantilever array type P-VEH

3.3 Clamped-Clamped or guided beam structures

A clamped – clamped structure or guided beam structure is fixed from both ends and having seismic mass at the center. A clamped – clamped structure was first designed and fabricated by Marzencki et al. [53] in 2009. In 2012, Wang et al. [60] designed and fabricated a clamped – clamped structure with lower frequency operation of 694 Hz. Guided beam structures provide stable and reliable operation as they are fixed from both ends that enable to sustain higher stress and lesser displacement which reduces frequent

collision from cavity. However, due to fixed nature of beams guided beam structure has higher spring constant which results in higher resonance frequency. Guided two-beam device fabricated by Marzencki et al. [53] has a resonance frequency of 1800 Hz and that developed by Wang et al. has 694 Hz [60]. The resonance frequency for the guided two-beam device reported by [53, 60] is at higher end. Therefore, this motivated us to further investigate the two-beam guided cantilever structures for obtaining low frequency of operation by optimizing the design parameters.

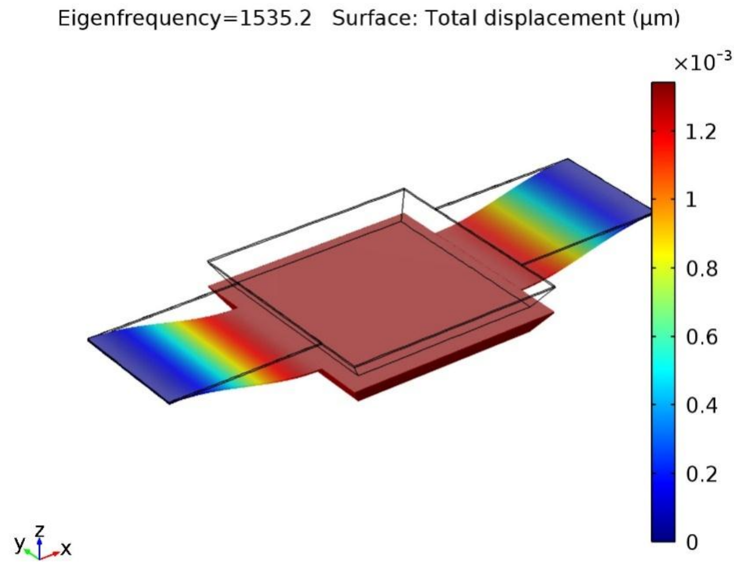

Fig. 3.11 Snapshot of eigen mode generated by the guided two-beam structure

A two-beam structure having dimensions as beam length 2500 µm width 2000 µm and thickness 20 µm, seismic mass having dimensions as 3500 x 3500 x 330 µm shown in Fig. 3.11 is simulated for obtaining the nature of displacement, stress and electric potential.

The nature of displacement of guided beam structures follows the following curve is given by equation 3.6 [60].

$$Z(x) = \frac{d}{2}\left(1 - \cos\frac{\pi x}{l}\right) \qquad 3.6$$

The beam displaces from fixed end and also at the guided end as depicted from graph in Fig. 3.11. Guided beam structure is fixed at both ends and having seismic mass at the other end, therefore, collision from the encapsulation cavity of the guided beam structure is very less.

von-Mises stress of the guided beam structure is given in Fig. 3.13. There are two types of stress present tensile stress at fixed end and compressive stress at the guided end which are opposite in nature. Electric potential is generated due to tensile and compressive stress. Opposite charges are generated at the fixed end and guided end as seen from Fig. 3.14. At fixed end due to tensile stress a maximum electric potential of 0.1 V is generated and at the guide end due to compressive stress 0.1 V of electric potential is generated. It can be seen that the individual potential generated at the fixed and guided end can be combined in series therefore the net potential generated will be 0.2 V at one side of the beam and 0.4 V on both sides of the beam.

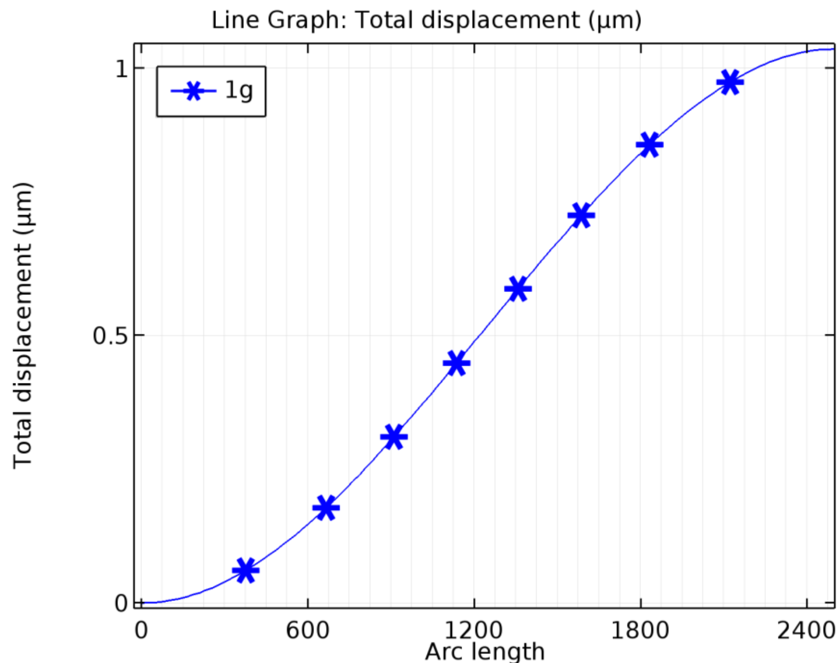

Fig. 3.12 Line graph of total displacement v/s arc length of guided beam type structure.

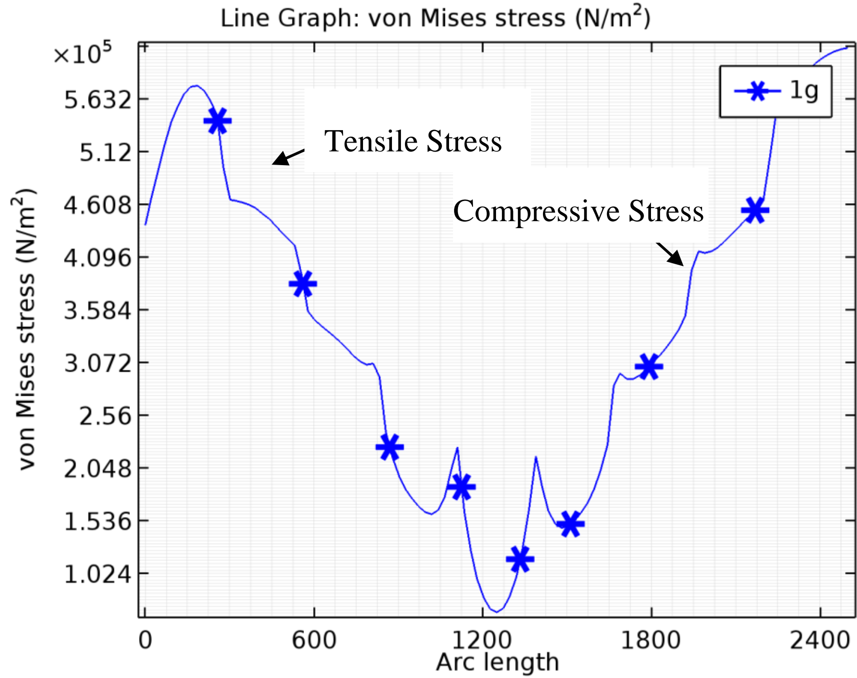

Fig. 3.13 Graph of von-Mises stress v/s arc length of guided beam structure

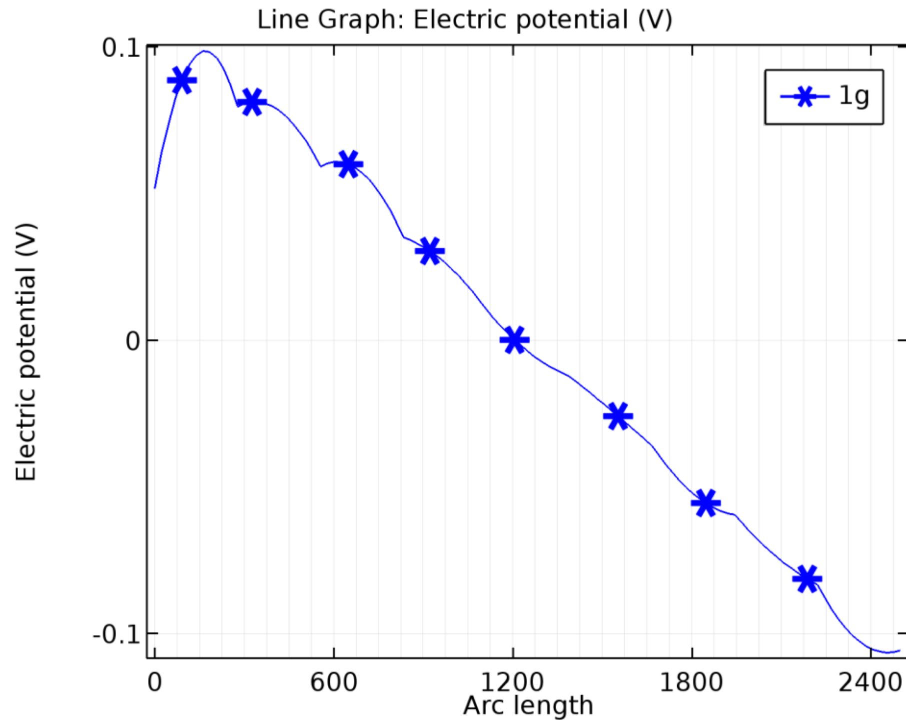

Fig. 3.14 Graph of electric potential generated at various arc length for guided beam structure.

3.4 Comparison

Three major structures used for the design of piezoelectric energy harvesters are compared.

Table 3.1 Comparison of the three structures used as piezoelectric energy harvester.

S.No:	Single Beam	Generator Array	Guided Beam	Remarks
Displacement	8.5 µm	5.7351, 5.80, 6.1 µm	1µm	Lower displacement gives better stability
Stress	6.5 x 10^6N/m^2	6.5 x 10^6N/m^2	5.6 x10^5 N/m^2	Lower stress reduces risk of beam fracture
Electric potential	0.6 V	0.6 V	0.1V and 0.4V (net)	Higher electric potential better
Resonance Frequency	764 Hz	681,867,1215 Hz	1535 Hz	Lower resonance frequency better
Residual Stress	High because free from one end	High because free from one end	Low because fixed from both ends	Lower residual stress is required
Stability	Low (due to high displacement)	Low (due to high displacement)	High (due to less displacem ent)	Less displacement reduces collision from cavity
Reliable	Low (risk of beam fractures)	Low (risk of beam fractures)	Higher (fixed beams has lower risk)	Guided structure is more reliable
Ease of fabrication	Relatively Complex due to fragile nature of free end cantilevers)	More complex due to multiple cantilevers release in fabrication	Less Complex Due to fixed beam structures.	Guided beam structures can be designed and fabricated with less complexity.

It can be seen from Table 3.1 that guided beam structure has many advantages over single cantilever and generator array type structures. Therefore, the further research work reported in this thesis is focused on guided beam type piezoelectric energy harvesters. A four-beam structure is designed and compared with a two-beam structure. Both the structures are fabricated and experimental results are compared.

3.5 Effect of shape of seismic mass on potential generated by piezoelectric energy harvester

Seismic mass 'm' is placed at the free end of the cantilever structure or at the center of the guided beam structure to reduce the resonance frequency of the energy harvester to match with ambient vibrations. Generally the shape of the seismic mass designed and realized in MEMS are square in shape [61]. The effect of shape of seismic mass on the potential generated by P-VEH has not been investigated. In this section, the effect of the shape of the seismic mass due to the change in the position of center of mass on output potential generated by P-VEH has been investigated. The geometry of the seismic mass will affect the change in the position of the center of mass of the system, resulting in a change in the potential generated. The center of mass for the device is analytically calculated by dividing the structure into the cantilever beam and the seismic mass. The center of mass for the two structures are individually calculated and the vector sum is obtained to investigate the resultant effect of the center of mass of the seismic mass on the system. The geometry of the seismic mass is changed in such a manner that the width, depth, and height of the seismic mass remain constant; therefore, the effect of shape can be investigated. The cantilever has a length: 2500 µm, width: 2000 µm and height 20 µm respectively. The substrate layer is silicon which has a thickness of 20 µm. A piezoelectric layer of Zinc oxide (ZnO) with a thickness of 2 µm is deposited on the silicon substrate. The seismic mass has dimensions from top as 3500 x 3500 µm, and height 330 µm, and slant ratio (r) which is a variable having a range between 0 and 1 that varies the bottom of the seismic mass from 0 to 3500 µm. The slant length of the shape of the seismic mass can be varied using variable r: when $r = 0$ it gives a maximum slant length which gives a triangular structure, when $r = 0.4$ it changes the shape to a pyramidal structure, and when $r = 1$ it forms a rectangular-shaped seismic mass, as shown in Figures. 3.15 (a), 3.15 (b), and 3.13 (c), respectively. The center of mass of the energy harvester that has rectangular shaped and triangular shaped seismic mass is calculated and compared. The center of mass of the cantilever beam with dimensions length 2500 µm, width 2000 µm, and height 20 µm, will be at its centroid (1250, 1000, 10) because it is cuboid in shape. Similarly, the center of mass of the rectangular shaped seismic mass

that has dimensions length 3500 μm, width 3500 μm, and height 330 μm (toward the negative z-axis) will be at its centroid (1750, 1750, −165).

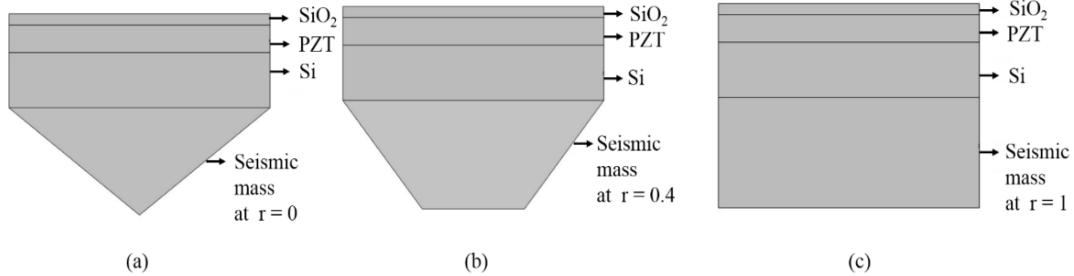

Fig. 3.15 (a) The shape of seismic mass (triangular) when the ratio r = 0, (b) the modified shape of seismic mass (pyramidal) at r = 0.4, and (c) the shape of seismic mass (rectangular) at r =1.

The resultant center of mass of these two will be the center of mass of the energy harvester, which can be calculated using equation 3.7

$$\text{Center of mass } (\mu) = \frac{m_1 r_1 + m_2 r_2}{m_1 + m_2} \qquad 3.7$$

where m_1 and m_2 are the masses and r_1 and r_2 are the locations of the center of mass. The mass of the cantilever beam and seismic mass can be calculated from the density of Polysilicon is 2320 kg⁄m^3 and the volume of the cantilever beam is 10^8 μm^3 and that of the rectangular shaped seismic mass is 4042.5 x 10^6 μm^3 which is calculated as 232 × 10^{-9} and 9378.6 × 10^{-9} kg, respectively. Calculating the center of mass using equation 3.7, the center of mass of the energy harvester with a rectangular shaped seismic mass is obtained as:

$$\text{Center of mass } (\mu) = 1737.125\,\vec{x} + 1731.1\,\vec{y} - 160.75\,\vec{z} \qquad 3.8$$

The center of mass will be at a distance of h/4 from the base when the triangular shaped seismic mass is considered, where h is the height of the triangle. The width and depth of the seismic mass remain unchanged, therefore, the center of mass for a triangular-shaped seismic mass will be (1750, 1750, −82.5), the volume of the triangular shape is 4042.5 x 10^6 μm^3, and the mass of the triangular shaped seismic mass is calculated as 9378.6 ×

10^{-9} Kg. The center of mass for the cantilever beam remains the same. The resultant center of mass is calculated using equation 3.7, the center of mass of the energy harvester with a triangular shaped seismic mass is

$$\text{Center of mass } (\mu) = 1737.125\,\vec{x} + 1731.1\,\vec{y} - 80.50\,\vec{z} \qquad 3.9$$

The centers of mass for an energy harvester having a rectangular shape and a triangular shape seismic masses are given by equations. 3.8 and 3.9 respectively.

Table 3.2 Comparison of different shape of seismic mass

Shape	Center of mass of Cantilever	Center of mass of Seismic mass	Resultant Center of mass
Rectangular Shape	(1250, 1000, 10)	(1750, 1750, −165)	1737.125, 1731.1, -160.75
Triangular Shape	(1250, 1000, 10)	(1750, 1750, −82.5),	1737.125, 1731.1, -80.50

As seen from Table 3.2, the rectangular shaped seismic mass shifts the center of mass of the cantilever by (1737.125x + 1731.1y -160.75z), whereas the triangular shaped seismic mass shifts the center of mass of the cantilever by (1737.125x + 1731.1y - 80.50z) which is (80.24z) above as compared with the center of mass of the rectangular shaped cantilever. When a boundary load of 1 bar pressure is applied on the top surface of the cantilever, the energy harvester with a triangular shaped seismic mass having center of mass shifted toward the top surface of the cantilever generates a higher potential as compared with the rectangular shaped seismic mass. The motion of the cantilever structure is around its center of mass, and when center of mass shifts upward or toward the point where force is applied, then a higher force is exerted on the center of mass resulting in higher generated potential.

3.6 Simulation of different geometries of Seismic Mass

COMSOL Multiphysics® simulation tool is used to verify the effect of the seismic mass shape of the energy harvester on the potential generated. A boundary load is applied on the top surface of the cantilever to obtain the results. Fig. 3.16 (a) represents the displacement along the surface of the cantilever, where displacement is maximum the stress is minimum due to the motion of the cantilever at the free end. The red region depicts the maximum displacement and low value of the electric potential, the yellow region depicts the medium range of the potential generated, and the blue region at the fixed end of the cantilever exhibits the minimum deflection region having maximum stress and electric potential. This distribution of electric potential can be verified from the piezoelectric layer along which the output of the energy harvester is computed from (0 to 2500 μm) termed as the arc length, while the other side of the piezoelectric layer is grounded. Fig. 3.16 (b) shows the distribution of von-Mises stress along the surface of the cantilever structure, where stress is maximum at the fixed end and minimum at the free end of the cantilever where value of stress is maximum in the region where there is minimum deflection of cantilever and decreases toward the free end of the cantilever. The potential is maximum at the fixed end of the cantilever because the stress is maximum at the fixed end of the cantilever.

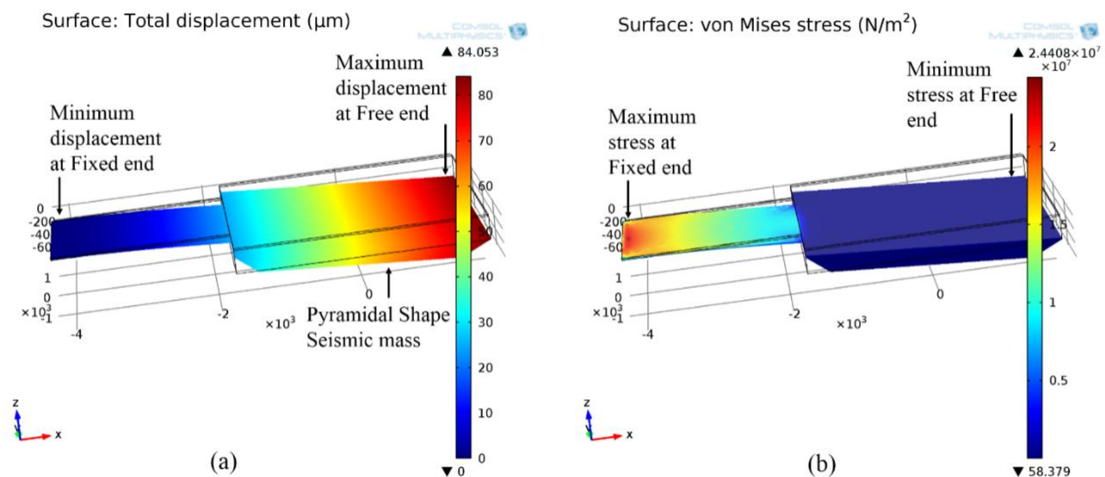

Fig. 3.16 (a) Displacement generated along the surface of the cantilever structure. (b) Distribution of von-Mises stress along the surface of the cantilever structure.

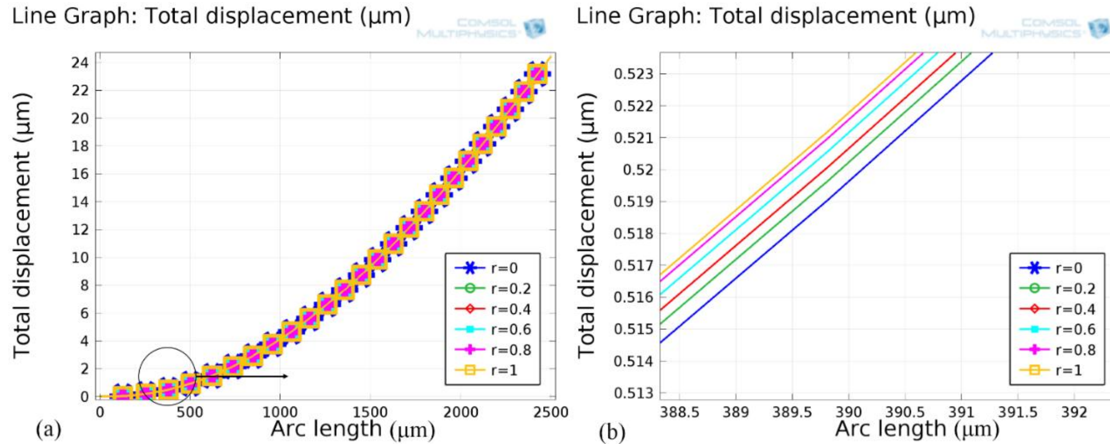

Fig. 3.17 (a) Displacement versus arc length graph for different values of r. (b) Displacement versus arc length graph extended curve from arc length 388µm to 392 µm for different values of r.

Line graphs are correlated with the region of minimum deflection which produces maximum stress generating a maximum potential near the fixed end and discussed in the next section. The different shape of the seismic mass is investigated to study the effect of shape on the output parameters of the cantilever. Parameter 'r', the ratio of the top and bottom length of the seismic mass, is varied from 1 to 0 with a step size of 0.2, which results in a variation from rectangular shaped to triangular-shaped (with the pyramidal shape as the intermediate shape) of the seismic mass. Fig. 3.17 (a) represents the displacement of the cantilever along the arc length for different shapes (r varies from 0 to 1) of seismic mass. It can be seen that the displacement is minimum near the fixed end and it increases non-linearly towards the free end of the cantilever. Fig. 3.17 (b) gives an extended view of the displacement curve from 388 µm to 392 µm, this region is considered because it is the region where the maximum potential is generated. For a triangular shaped ($r = 0$) displacement at 392 µm is 0.519 µm and for a rectangular shaped ($r = 1$) displacement at 392 µm it is 0.522 µm. Fig. 3.18 (a) gives the distribution of von-Mises stress along the length of the cantilever, at the fixed end stress is maximum where the displacement is minimum. There is an abrupt variation near fixed end from arc length 0 to 10 µm, which again justifies the investigation results that at the fixed end the stress is maximum and displacement is almost negligible. Fig. 3.18 (b) gives the extended

curve from 384 μm to 392 μm. The maximum stress is 1.771 x 10^7 N/m^2 for triangular shape (r = 0) and 1.773 x 10^7 N/m^2 for rectangular shape (r =1).

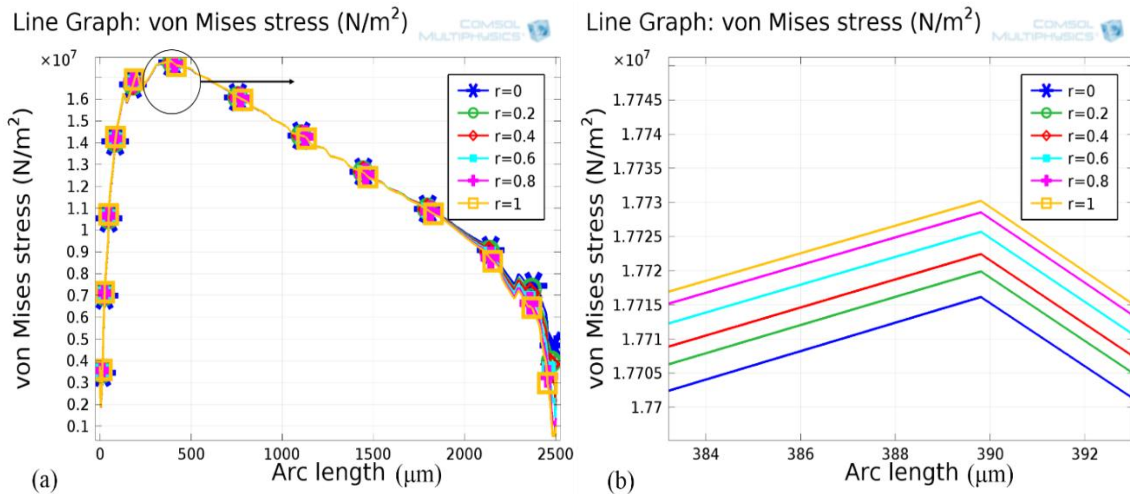

Fig. 3.18 (a) von-Mises stress versus arc length graph for different values of r. (b) von-Mises stress versus arc length graph extended curve from arc length 384 to 392 μm for different values of r.

Fig. 3.19 (a) gives the electric potential versus arc length curve from 0 to 2500 μm. Fig. 3.19 (b) is an extended view of the electric potential versus arc length curve from 330 to 390 μm, where the cantilever having a triangular-shaped seismic mass generates a potential of −1.16 V, whereas a rectangular-shaped seismic mass generates −1.13 V (negative sign signifies the polarization of the piezoelectric layer with the base axis). It can be seen that the potential generated by the triangular shape seismic mass structure is higher than the potential generated by rectangular shape seismic mass by 0.03 Volts. Which justifies the fact that there is considerable effect of the shape of seismic mass on the potential generated by the energy harvester.

3.7 Discussion

The effect of the shape of a seismic mass on the output parameters of a piezoelectric energy harvester is investigated, analyzed, and compared. A triangular-shaped seismic mass generates a potential of 2.064 V, whereas a rectangular-shaped seismic mass

cantilever structure generates a potential of 2.060 V, which clearly shows that there is a considerable increase in potential due to the variation in the shape of seismic mass.

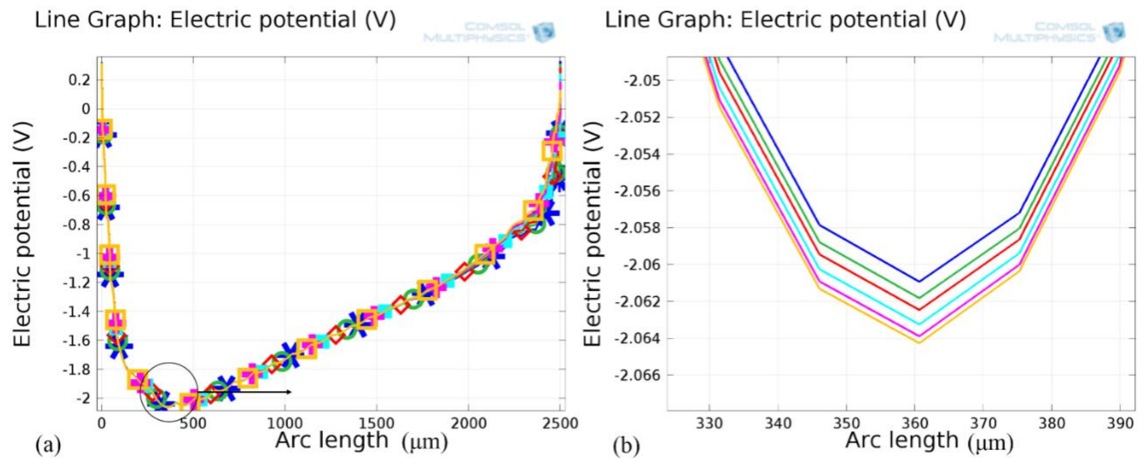

Fig. 3.19 (a) Electric potential versus arc length graph for different values of r. (b) Electric potential versus arc length graph extended curve from arc length 330 to 390 μm for different values of r.

The increased potential generated by the triangular-shaped seismic mass is due to the fact that the resultant center of mass of the geometry (cantilever structure and seismic mass section) gets shifted upward, i.e., toward the applied pressure, which results the exertion of a high force which leads to a higher potential being generated. However, to fabricate a triangular shape seismic mass (high slant ratio) requires a very high precision during bulk micromachining. Hence as an alternative, pyramidal shape seismic mass is used for the design and which can be realized using Tetra Methyl Ammonium Hydroxide (TMAH) CMOS compatible 25 wt.% wet etching which gives an etch angle of 54.6 at <100> plane. In the next chapter, this pyramidal shape seismic mass is used to design guided two-beam and four-beam structure and FEM results are obtained and compared.

3.8 Effect of piezoelectric material on guided beam piezoelectric energy harvester

FEM simulation for different piezoelectric materials; ZnO, PZT-5H and AlN have been done and the results are presented in Table 3.3 for guided four-beam P-VEH and in Table 3.4 for guided two-beam P-VEH.

Table 3.3 Comparison for different piezoelectric materials for guided four beam P-VEH

Thickness = 2 µm	Displacement	Von-Mises Stress	Potential (fixed end)	Potential (guided end)
ZnO	0.09889 µm	97801.476 N/m^2	**0.01779** V	**-0.01819** V
PZT-5H	0.1102 µm	80558.179 N/m^2	0.00231 V	-0.00233 V
AlN	0.0789 µm	140614.781 N/m^2	0.01147 V	-0.01175 V

Table 3.4 Comparison for different piezoelectric materials for guided two beam P-VEH

Thickness = 2 µm	Displacement	Von-Mises Stress	Potential (fixed end)	Potential (guided end)
ZnO	0.191 µm	191473.062 N/m^2	**0.03412** V	**-0.03551** V
PZT-5H	0.212 µm	157260.796 N/m^2	0.00442 V	-0.00455 V
AlN	0.151 µm	273237.3125 N/m^2	0.02187 V	-0.02272 V

It can be observed from the above FEM analysis that the ZnO piezoelectric material results in maximum potential generation for both guided two-beam and four-beam P-VEH. Therefore, ZnO material was selected during device fabrication.

The most important requirement for energy harvesters is to have a lower resonance frequency to tune with ambient vibrations. The physical parameters such as length, width and thickness are varied to reduce the resonance frequency of the energy harvester. Before device fabrication the device parameters for the guided beam type P-VEH have been optimized for lower resonance frequency. The electrical sensitivity depends on

piezoelectric material, layer thickness and stress exerted on the piezoelectric layer. For ZnO material, the thickness to achieve maximum electrical sensitivity is 2.5 μm, after which electrical properties gets saturated [104]. Therefore, the optimized thickness of 2.5 μm has been used during device fabrication of the energy harvester device.

The temperature has an effect on stiffness of the piezoelectric layer. As temperature increases, the stiffness in the piezoelectric layer decreases. As stiffness decreases, the resonance frequency of the device is reduced [106].

The temperature has an effect on piezoelectric properties of the material. After deposition of the piezoelectric film the annealing temperature up to 400ºC improves the crystallographic orientation and improves piezoelectric properties [104]. The ZnO layer deposited has been annealed at a temperature of 300ºC.

Chapter 4

Design and FEM Simulation of Guided Beam Piezoelectric Energy Harvester

Design of a device is always limited by the technology i.e. device is designed in such a way that it could be realized through the use of the available fabrication technology in a perfect manner to get optimum output. Therefore, dimensions of the structures in the device and the different layers are taken up in such a way that they are compatible with the available MEMS fabrication technology. Therefore, guided beam structure, fixed from four ends and having proof mass at the center gives stable, reliable and improved response as compared to single beam cantilever structure. Proof mass is supported with four-beams which gives a stable operation and ability to sustain higher stress values due to high amplitude vibrations as compared to single beam cantilever [53]. Four-beams provide higher stiffness to the structure resulting in lower displacement which reduces frequent collision of the proof mass with the encapsulation layer of the device. As the proof mass at the center is guided by four-beams, this structure gives lower residual stress as compared to single beam cantilever structure. Piezoelectric layer on four-beams generates potential due to compressive and tensile stress which can be connected in series to increase the output potential generated.

4.1 Design of guided four-beam P-VEH

In this section guided four-beam structure is designed and FEM simulation for the guided four-beam is reported and is compared analytically. The four-beams connected at center with proof mass offers centro-symmetric geometry. Guided beams have dimension as length 2500 µm, width 2000 µm and thickness 20 µm respectively. The guided four-beam structure is shown in Fig. 4.1 each beam is fixed from one end and connected with proof mass at the other end.

Shape of the proof mass affect the potential generated as discussed in the previous chapter, a pyramidal shape proof mass provides higher generated potential. This pyramidal shape of the proof mass is obtained through Wet-Bulk micromachining using Tetra Methyl Ammonium Hydroxide (TMAH) etching with suitable corner compensation structures. Dimensions for the proof mass at the top are (CD) 3500 x 3500 μm, and at the bottom (AB) equals 3033 x 3033 μm, height (h) is 330 μm and ratio 'r' (AB/CD) is 0.86 as shown in Fig. 4.2.

Guided four-beams of silicon comprise of four layers (i) oxide layer for insulation between substrate and the bottom electrode, (ii) bottom electrode of Gold (Au)/Aluminum (Al) for charge collection, (iii) Piezoelectric layer of Zinc oxide (ZnO) is sputtered over bottom electrode, (iv) Top electrode (Au/Al) is sputtered over piezoelectric layer for charge collection. A passivation layer of PECVD oxide of thickness 0.2 micron was incorporated at the bottom and top surface of the ZnO layer to save it from the deterioration due to ambient Oxygen and water vapor in the atmosphere.

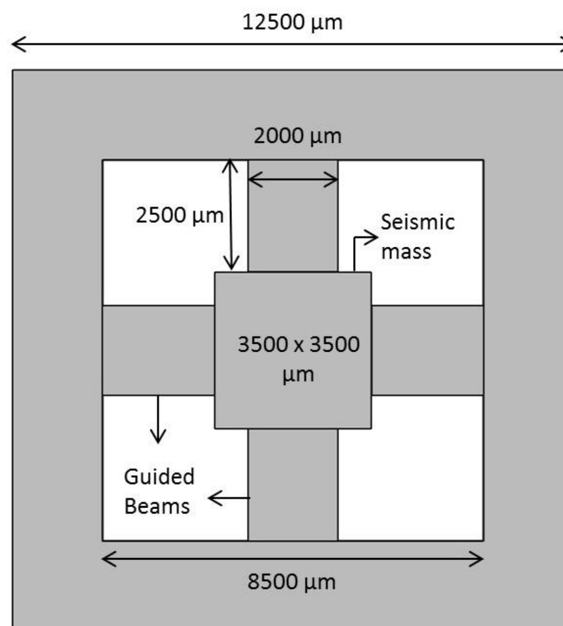

Fig. 4.1 Snapshot of design structure for guided four-beam P-VEH.

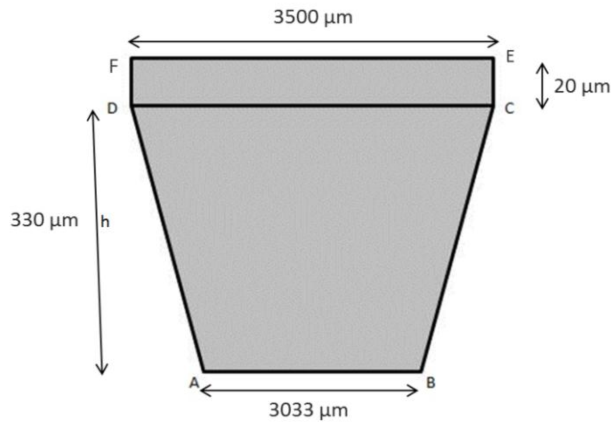

Fig. 4.2 Cross-sectional view of the proof mass.

For device fabrication a P-type silicon substrate (100) of 3 inches diameter and a thickness of 350±25 µm is suitable to obtain pyramidal shape proof mass of height 330 µm thickness. Ambient vibration displaces the guided beams which generate tensile and compressive stress in the beams resulting in the generation of charge along the piezoelectric layer due to piezoelectric effect. ZnO material has been selected because of its compatibility with CMOS fabrication technology and higher piezoelectric coefficient.

4.2 FEM analysis of guided four-beam P-VEH

In this subsection guided four-beam structure is designed and thoroughly investigated using Finite Element Method (FEM) simulator (COMSOL Multiphysics®) and compared analytically. Parameters such as resonance frequency, total displacement, von-Mises stress, output potential, are obtained as a function of input acceleration.

4.2.1 Resonance Frequency

As already discussed the first criterion to generate maximum output power is to tune the resonance frequency of the guided beam cantilever to the frequency of ambient vibration. The resonance frequency of the guided cantilever depends on spring constant (k) of the beams and seismic mass (m) at the center as given by equation (4.1).

$$f = \frac{1}{2\pi}\sqrt{\frac{k}{m}} \tag{4.1}$$

$$k = \frac{2EWt^3}{l^3} \qquad \text{(for guided two − beam)} \qquad (4.2)$$

$$k = \frac{4EWt^3}{l^3} \qquad \text{(for guided four − beam)} \qquad (4.3)$$

Guided beam cantilever with seismic mass is modeled by spring mass damper systems having a fixed resonance frequency. Seismic mass (m) reduces the resonance frequency of the system which is required to tune with ambient vibrations of low frequency. Spring constant of the cantilever depends on Young's modulus (E), width (W) thickness (t) and the length (l) of the cantilever as given by equation (4.2). Resonance frequency for the guided cantilever beam is obtained using FEM simulator for different thickness (from t = 5 μm to 20 μm) of the beam and compared analytically. Length (l) and width (W) of the four guided beams are fixed at 2500 μm and 2000 μm respectively. Seismic mass having dimensions 3500 x 3500 x 330 μm and weight 8.155 x 10^{-6} kg is attached at the center of the four-beams to lower the resonance frequency. FEM simulation gives resonance frequency at 335.96 Hz for a beam thickness of 5 μm as shown in Fig. 4.3.

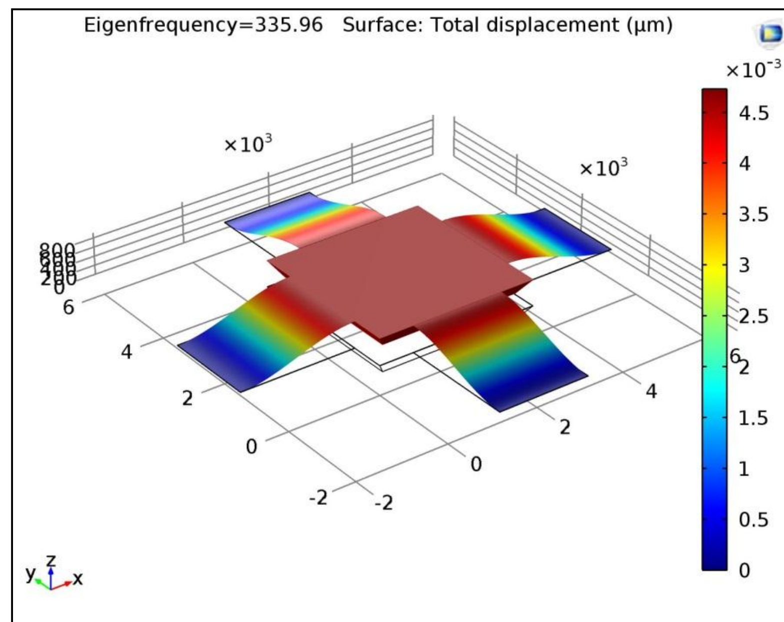

Fig. 4.3 Resonance frequency for four-beam guided cantilever structure at a beam thickness of 5μm is 335.96 Hz obtained using FEM.

Resonance frequency when calculated analytically using equation (4.1 and 4.3) at a thickness of 5 µm of the silicon beam comes out to be 337.72 Hz. As thickness of the silicon beam increases the resonance frequency of the system increases non-linearly as given by equation (4.3). When the beam thickness is increased to 20 µm, the resonance frequency obtained is 1631.4 Hz using FEM simulation which justifies equation (4.3). Resonance frequency when calculated analytically using equation (4.1) at a thickness of 20 µm increases to 1754.85 Hz which is reported in Fig. 4.4. It can be observed from Fig. 4.4 that the resonance frequency obtained using FEM simulator and calculated analytically are in close agreement to each other.

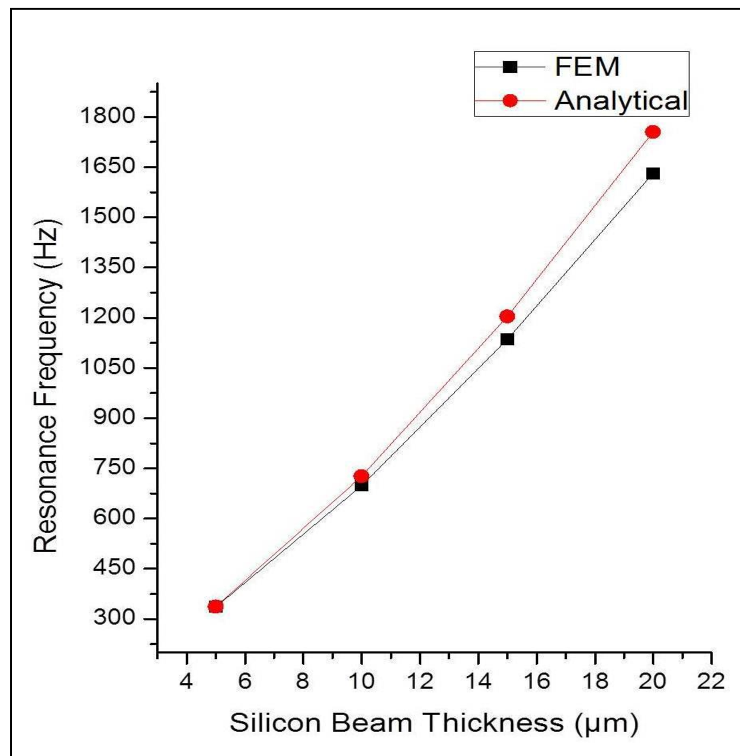

Fig. 4.4 Resonance frequency at a thickness of 5 µm to 20 µm of the silicon beam. The minimum and maximum resonance frequency obtained at 335.96 Hz and 1631.4 Hz for beam thickness of 5 µm and 20 µm respectively.

Resonance frequency obtained at different thickness of guided beam from 5 µm to 20 µm is in lower frequency region which is suitable for energy harvesting applications. Previous designs of the guided beam structures have resonance frequency of 1800 Hz [53] and 694 Hz [60]. The results reported in Fig. 4.4 conclude that a four-beam guided

cantilever structure is capable of operating at lower frequency range (below 500 Hz) so as to resonate with the frequency of the ambient vibrations. Therefore, the design suggested and reported is suitable for piezoelectric type energy harvester device applications which can be fabricated using MEMS technology. In the proceeding sections guided beam cantilever type piezoelectric energy harvester is investigated with external vibrations. The acceleration is varied from a range of 1g to 5g and parameters such as displacement, von-Mises stress and electric potential are obtained and reported in the subsequent sections.

4.2.2 Displacement

In this section, displacement of the guided four-beam structure is discussed. Displacement of the guided beam from fixed end towards the guided end is obtained for input acceleration ranging from 1g to 5g. In dominant frequency mode of operation the guided beam structure displaces in ±Z direction as was shown in Fig. 4.3. Arc length is the length from fixed end of the beam to the guided end of the beam where proof mass is attached. The arc position selected is the interface of the top surface of piezoelectric layer and the top electrode where charge is generated and collected. Displacement versus arc length graph for the guided beam at an input acceleration ranging from 1g to 5g is shown in Fig. 4.5. It can be seen from the graph that a displacement of 0.095 µm is obtained at an input acceleration of 1g which gradually increases with the input acceleration and reaches to a maximum value of 0.479 µm at an acceleration of 5g. The graph in Fig. 4.5 justifies that the maximum displacement occurs at the guided beam end attached to seismic mass and it reduces towards the fixed end of the beams. Deflection of the beam is minimum at the fixed end therefore displacement is minimum which results in higher stress generation at the fixed end of the guided beam structure. The device operation should be in dominant mode to have resonance with low-frequency ambient vibrations; therefore, displacement curves for dominant mode are of significance.

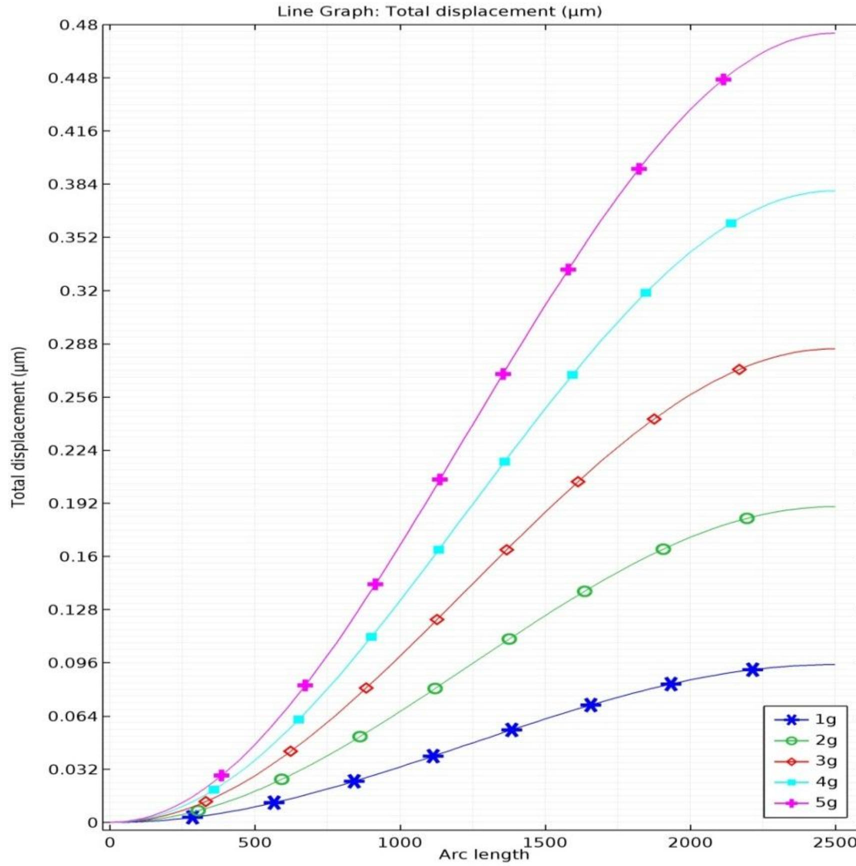

Fig. 4.5 Displacement versus arc length graph for the guided beam for input acceleration from 1g to 5g. Displacement values of 0.095 µm and 0.479 µm are obtained at an input acceleration of 1g and 5g respectively.

Displacement of the device is a key parameter in determining the depth of the cavity for the device encapsulation, larger the value of displacement larger the depth of the cavity is required otherwise due to collisions, fracture of beams will take place. A four-beam guided structure is fixed from four ends which results in lower displacement and lead to the stable operation of device, furthermore, the problem of residual stress is also not dominant in the reported structure as the beams have larger width and are fixed from four ends. Displacement of the guided beam is also compared with the displacement of single beam cantilever structure as shown in Fig. 4.6. One end of the cantilever is fixed and seismic mass is attached at the other end. The dimensions of cantilever structure are length 2100 µm, width 200 µm and thickness 5 µm which is designed using FEM.

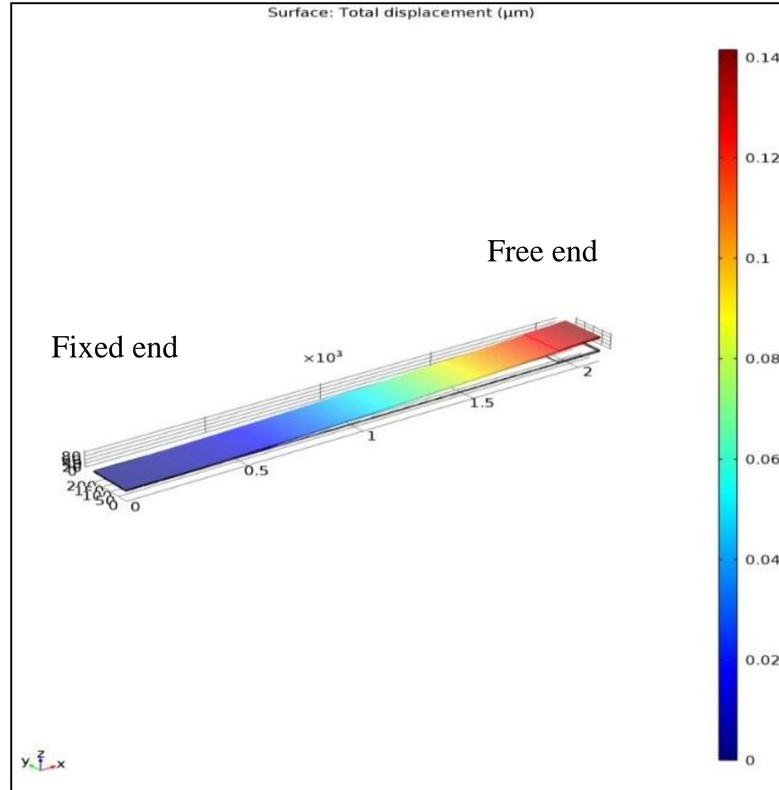

Fig. 4.6 Single beam cantilever with proof mass having resonance frequency of 1611.9 Hz gives displacement of 0.14 µm at an input acceleration of 1g.

When an input acceleration of 1g is applied the single beam cantilever gives a displacement of 0.14 µm which resonates at a frequency of 1611.9 Hz. However the proposed guided beam structure gives a displacement of 0.095 µm at 1g input acceleration which is less by 32.14% as compared to displacement obtained by single beam cantilever structure.

4.2.3 von-Mises Stress:

Displacement of the device generates stress along the length of the guided beams. Tensile and compressive stress is generated at the fixed end and guided end of the device. Fig. 4.7 shows von-Mises stress versus arc length graph for the four-beam guided cantilever for input acceleration from 1g to 5g. Maximum stress of 9.4 x 10^4 N/m^2 is observed at an input acceleration of 1g whereas at an input acceleration of 5g maximum stress is 4.7 x 10^5 N/m^2 is observed across the piezoelectric layer (Fig. 4.7). At fixed end of the beam stress is maximum which decreases along the length of the beam and reaches

to a minimum value at a length of 1250 µm. Further as the length increases towards the guided end stress increases and reaches to its maximum value at length 2500 µm which justifies generation of tensile and compressive stress shown in Fig. 4.7. Maximum stress values are well below the fracture stress for silicon, therefore, the design can withstand input acceleration of 5g or even higher.

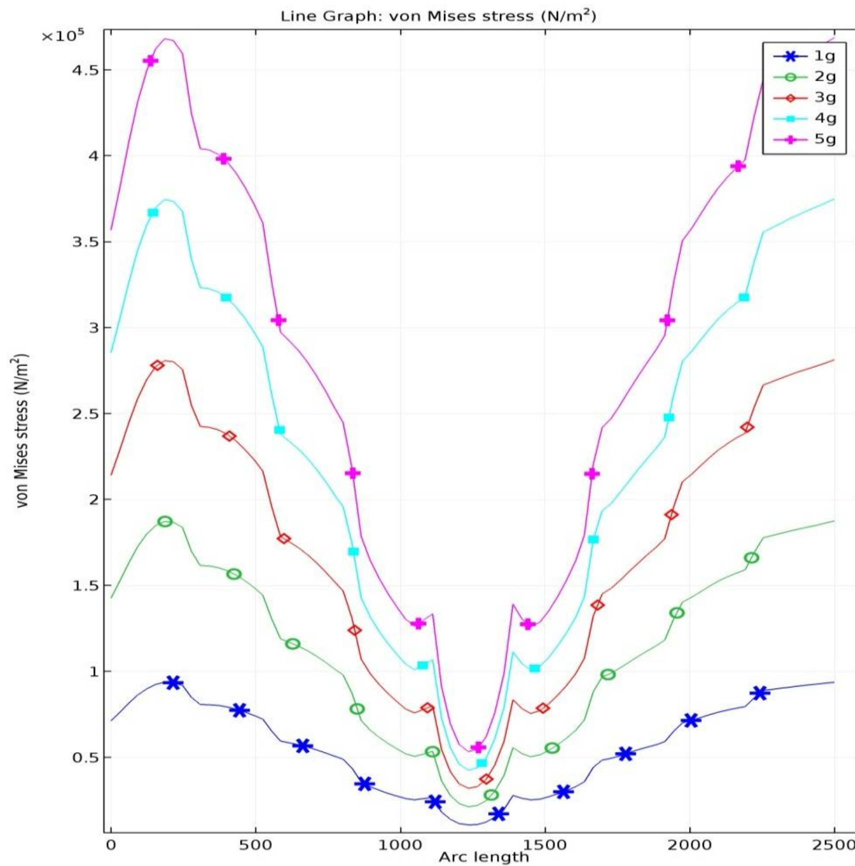

Fig. 4.7 von-Mises stress versus arc length graph for the guided beam for input acceleration from 1g to 5g. Maximum stress values of 9.4 x 10^4 N/m^2 and 4.7 x 10^5 N/m^2 is obtained at an input acceleration of 1g and 5g respectively

4.2.4 Electric Potential:

Stress in the guided beam results in generation of charge along the piezoelectric layer due to piezoelectric effect. Tensile and compressive stress generates charges of opposite polarities along the length of the piezoelectric layer. Fig. 4.8 shows electric potential

versus arc length graph for the guided four-beam structure for input acceleration from 1g to 5g.

Maximum potential generated at an input acceleration of 1g is 17.84 millivolts and at 5g is 89.21 millivolts which can be seen from Fig. 4.8. Electric potential generated across the piezoelectric layer is maximum at the point of maximum stress (i.e. fixed end and guided beam end) which gradually reduces towards the minimum stress region (i.e. at the center of the beam). The graph justifies that electric potential is generated with opposite polarities due to tensile and compressive stress near fixed and guided beam end. The advantage of using guided beam structure is that two separate set of electrodes can be deployed to harvest this potential having opposite polarities thus adding to the total potential harvested [60].

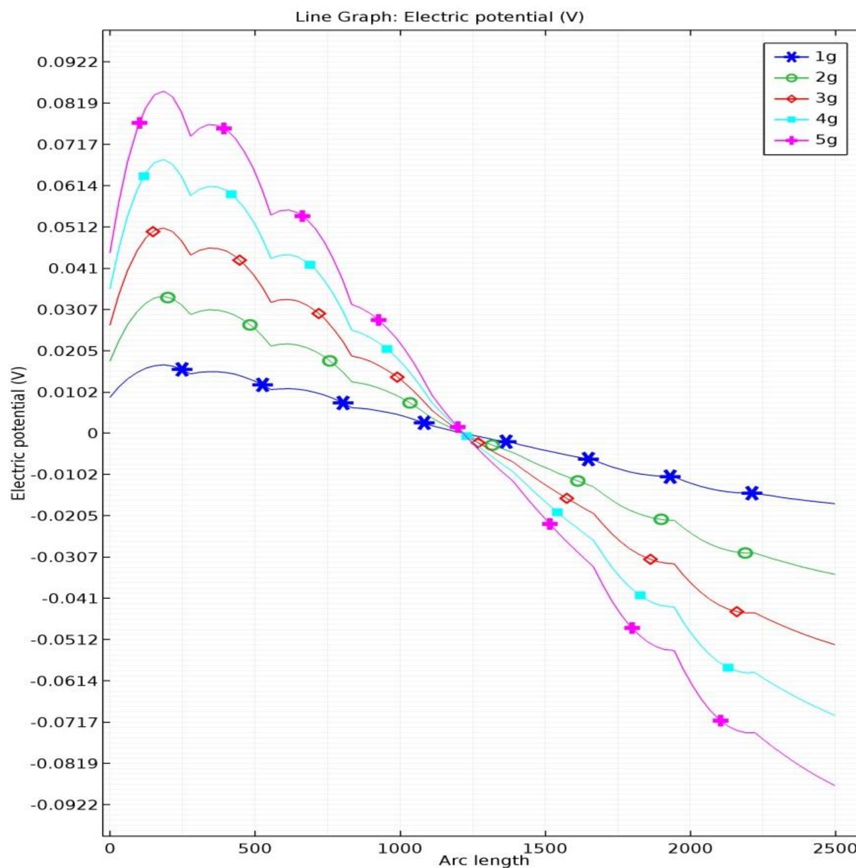

Fig. 4.8 Electric potential versus arc length graph for the guided beam for input acceleration from 1g to 5g. Maximum electric potential of 17.84 millivolts and 89.21 millivolts is obtained at an input acceleration of 1g and 5g respectively.

It can be observed that the potential generated due to tensile and compressive stress are quite similar in magnitude but with opposite polarities which are given in Table 4.1 for one beam. The same potential will be generated across the four-beams of four guided beam structure which can be connected in series or in parallel to increase the net electric potential harvested.

Table 4.1 Electric potential generated by one beam due to tensile and compressive stress at fixed end and guided end of four-beam guided cantilever structure.

Input acceleration	Electric potential at Fixed End (millivolts)	Electric potential at Guided End (millivolts)
1g	17.32	-17.84
2g	34.68	-35.68
3g	51.97	-53.52
4g	69.29	-71.37
5g	86.62	-89.21

4.2.5 Selection of Proof Mass

The design layout is prepared for thickness of 350 µm (3 inch). Beam thickness of 20 µm is kept so that it is achieved using TMAH etching and also withstands proof mass. Therefore the maximum thickness of the proof mass is fixed at 330 µm (which is selected for minimum resonance frequency). The length and the width of the proof mass is optimized by selecting three values i.e. 2500 x 2500 µm, 3500 x 3500 µm and 4500 x 4500 µm. Resonance frequency, stress and electric potential for the three variations are analyzed and then appropriate dimension for proof mass is selected.

As seen from Table 4.2 for case I proof mass of dimension 2500 x 2500 µm gives a resonance frequency of 2216.2 Hz and von Mises stress at 1g is 0.8×10^5 N/m^2 and reaches to a maximum value of 4 $\times 10^5$ N/m^2 at 5g. Electric potential generated is 9.3 millivolts and 46.5 millivolts at 1g and 5g respectively. Lower the mass dimension higher is the resonance frequency as given by equation (4.1). Furthermore, it reduces the displacement which further reduces the stress and potential generated.

Whereas for case III with proof mass dimension of 4500 x 4500 µm a resonance frequency of 1286.4 Hz is observed. von-Mises stress at 1g is 2 $\times 10^5$ N/m^2 and reaches to a maximum value of 10 $\times 10^5$ N/m^2 at 5g. Electric potential generated is 28.64 millivolts

and 143.2 millivolts at 1g and 5g respectively. As the mass dimension is high the resonance frequency generated is low but it results in higher stress values which may lead to fracture point of beams [60].

Table 4.2 Displacement, von-Mises stress and Electric potential at different dimensions of proof mass.

	1g	2g	3g	4g	5g
Case I 2500 x 2500 μm					
Displacement (μm)	0.050	0.100	0.140	0.200	0.250
von-Mises Stress (N/m^2, Maximum)	$0.8x10^5$	$1.6 x10^5$	$2.5 x10^5$	$3 x10^5$	$4 x10^5$
von-Mises Stress (Piezoelectric layer)	$0.5 x10^5$	$1.1 x10^5$	$1.6 x10^5$	$2.1 x10^5$	$2.6 x10^5$
Electric Potential (Volts)	0.0093	0.0186	0.0279	0.0372	0.0465
Case II 3500 x 3500 μm					
Displacement (μm)	0.095	0.190	0.286	0.382	0.479
von-Mises Stress (N/m^2, Maximum)	$1.5 x10^5$	$3 x10^5$	$5 x10^5$	$6 x10^5$	$8 x10^5$
von-Mises Stress (Piezoelectric layer)	$0.94 x10^5$	$1.8 x10^5$	$2.8 x10^5$	$3.7 x10^5$	$4.7 x10^5$
Electric Potential (Volts)	0.01732	0.03468	0.05197	0.06929	0.08662
Case III 4500 x4500 μm					
Displacement (μm)	0.140	0.300	0.450	0.600	0.700
von-Mises Stress (N/m^2, Maximum)	$2 x10^5$	$4.5 x10^5$	$7 x10^5$	$9 x10^5$	$10 x10^5$
von-Mises Stress (Piezoelectric layer)	$1.5 x10^5$	$3 x10^5$	$4.5 x10^5$	$6 x10^5$	$7.5 x10^5$
Electric Potential (Volts)	0.02864	0.05729	0.08593	0.11458	0.14322

Finally for Case II with dimension of 3500 x 3500 μm a resonance frequency of 1631.4 Hz is observed. von-Mises stress at 1g is $1.5 x10^5$ N/m^2 and reaches to a maximum value of $8 x10^5$ N/m^2 at 5g. Electric potential generated is 17.32 mV and 86.62 mV at 1g and 5g

respectively. As this dimension of proof mass gives considerable output with lower stress values hence chosen for designing the guided four-beam cantilever structure.

Guided four-beam cantilever type piezoelectric energy harvester is reported and investigated. The resonance frequency obtained analytically and compared using FEM tool is in agreement with each other and frequency range obtained is between 335.96 Hz. to 1631.4 Hz which is suitable for energy harvesting applications. Electric potential ranging from 17.84 mV to 89.21 mV is generated due to tensile and compressive stress for input acceleration ranging from 1g to 5g. Output potential can be increased further by connecting the individual output in series of the four-beams. This energy harvester is featured by a low displacement of 0.095 µm which is 32.14% less as compared to displacement obtained by single beam cantilever designed for the same resonance frequency. Low displacement of the guided beam structure reduces the probability of the collision of proof mass with the encapsulation layer of the device providing stable and reliable operation.

4.3 Comparison of guided two-beam and four-beam piezoelectric energy harvester

In this section FEM results obtained for the guided two-beam and four-beam piezoelectric energy harvester are compared. Parameters such as resonance frequency, total displacement, von-Mises stress, output potential, are obtained as a function of input acceleration and compared for the guided two-beam and four-beam structures respectively.

4.3.1 Comparison of guided two-beam and four-beam piezoelectric energy harvester

The guided two-beam and four-beam cantilever structure designed is fixed from both ends and has a pyramidal shaped seismic mass at the center as shown in Fig. 4. 9 (a) and 4.9 (b). The device has centrosymmetric nature with length of one beam is 2500 µm, width is 2000 µm and thickness 20 µm which can be seen from Fig. 4.9. These beams are fixed from the end and supported with seismic mass at the center. A grid of 2000 µm is designed which act as fixed end for the beams and also provide area for contact pads for bottom and top electrodes.

4.3.2 Resonance frequency

The first criterion for energy harvester to deliver optimum power is that the resonance frequency of the device should match with the frequency of ambient vibration. Energy harvester operating in resonance with the ambient vibration frequency gives maximum displacement which results in maximum output power.

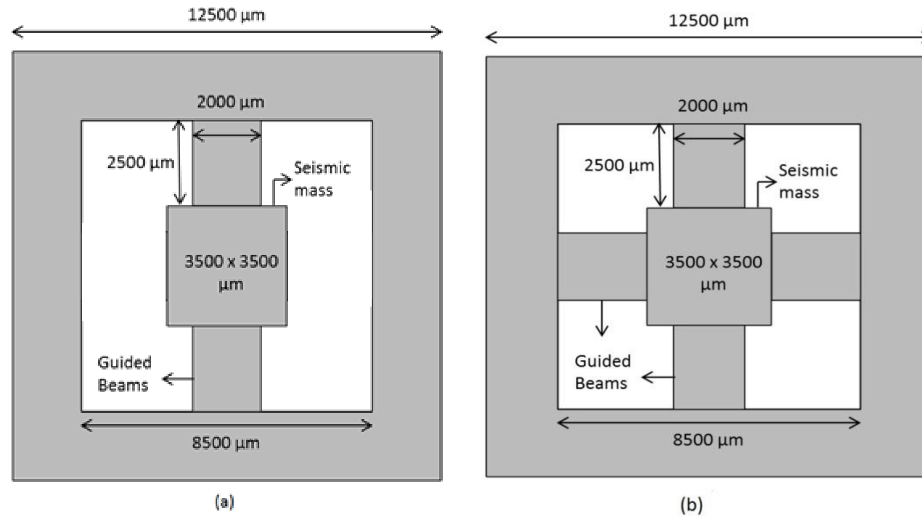

Fig. 4.9 Snapshot of design structure for (a) guided two-beam and (b) guided four-beam P-VEH.

This thickness of beam is selected as 25 µm for FEM eigen frequency analysis and piezoelectric device study so that a realistic comparison from the experimental results can be done. Fig. 4.10 (a) gives the first mode resonance frequency obtained from the simulator for the guided two-beam cantilever structure and it comes at 1535.2 Hz whereas the resonance frequency obtained for guided four-beam cantilever structure is 2141.1 Hz as shown in Fig. 4.10 (b). The resonance frequency calculated analytically at beam thickness of 25 µm for the guided two-beam cantilever structure using equation (4.1 & 4.2) is 1622 Hz whereas for the guided four-beam cantilever structure when calculated analytically using equation (4.1 & 4.3) comes at 2294 Hz. Second mode for the guided two-beam structure comes at 1798.9 Hz whereas for guided four-beam structure second mode is at 2141.1 Hz. Third mode for the guided two-beam structure comes at 4618.8 Hz whereas for guided four-beam structure third mode is at 35203 Hz.

The first mode of operation is the dominant mode having lowest resonance frequency at 1535.2 Hz for two-beam structure and 2141.1 Hz for four-beam structure.

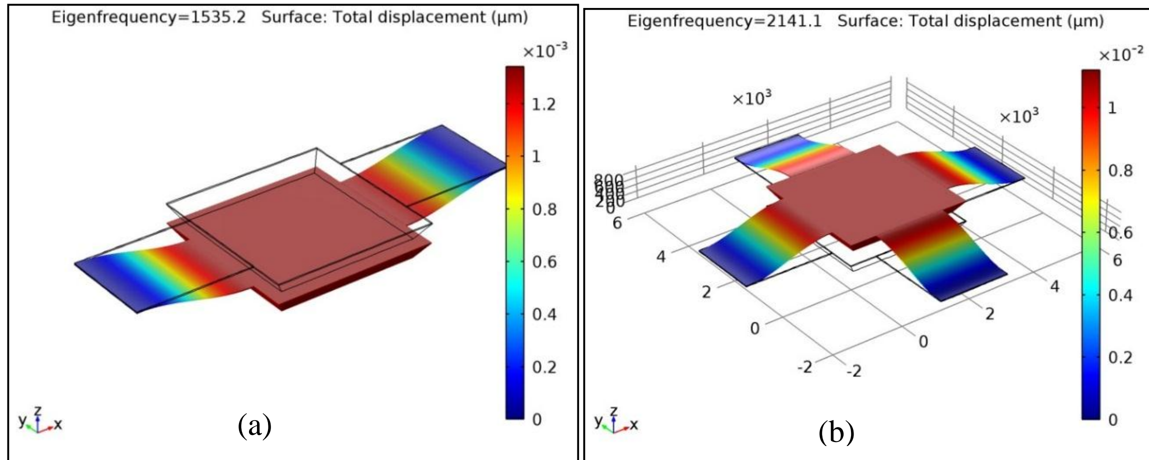

Fig. 4.10 (a). Snapshot of first mode at 1535.2 Hz for guided two-beam P-VEH. (b). Snapshot of first mode at 2141.1 Hz for guided four-beam P-VEH.

The dominant mode of operation gives displacement in ±Z direction which is the desired mode of operation for the energy harvesting device. Second mode is non-dominant mode along y-axis at 1798.9 Hz and 2141.1Hz which is not desired as it can severely affect the dominant mode device operation. Third mode is also non-dominant at 4618.8 Hz which is at higher frequency. It can be seen that for the first mode the resonance frequency obtained from FEM (i.e. 1535.2 Hz) and calculated analytically (i.e. 1622 Hz) are in close approximation with each other.

4.3.3 Displacement

Ambient vibration frequency when match with the resonance frequency of the device then maximum displacement in ±Z direction is obtained. In this section displacement of the beam from the fixed end towards the guided end (where proof mass is attached) is obtained for an input acceleration ranging from 1g to 5g for the two structures. Fig. 4.11 (a) and 4.11 (b) depicts the variation of displacement along the length (arc length) of a beam from fixed end towards the guided end for the two-beam and four-beam structure respectively. The graph justifies that the value of displacement is minimum at the fixed end which gradually increases towards the guided end attached with the proof mass. The

maximum displacement obtained at an input acceleration of 1g is 0.107 µm, as the acceleration is increased displacement also increases which reaches to a maximum value of 0.537 µm at an acceleration of 5g for guided two-beam cantilever structure as shown in Fig. 4.11 (a). Fig. 4.11 (b) gives maximum displacement obtained for guided four-beam cantilever structure at an input acceleration of 1g is 0.055 µm, as the acceleration is increased displacement also increases which reaches to a maximum value of 0.279 µm at an acceleration of 5g. Table 4.3 compares the maximum displacement for the guided two-beam and four-beam cantilever structure at an input acceleration range from 1g to 5g. As four-beams are attached with the proof mass at the center provides higher stiffness (k) which results in lesser displacement as compared with guided two-beam cantilever structure which is approximately double as 0.107 µm at 1g. As maximum displacement reduces the probability of frequent collision with the encapsulation of the devices reduces.

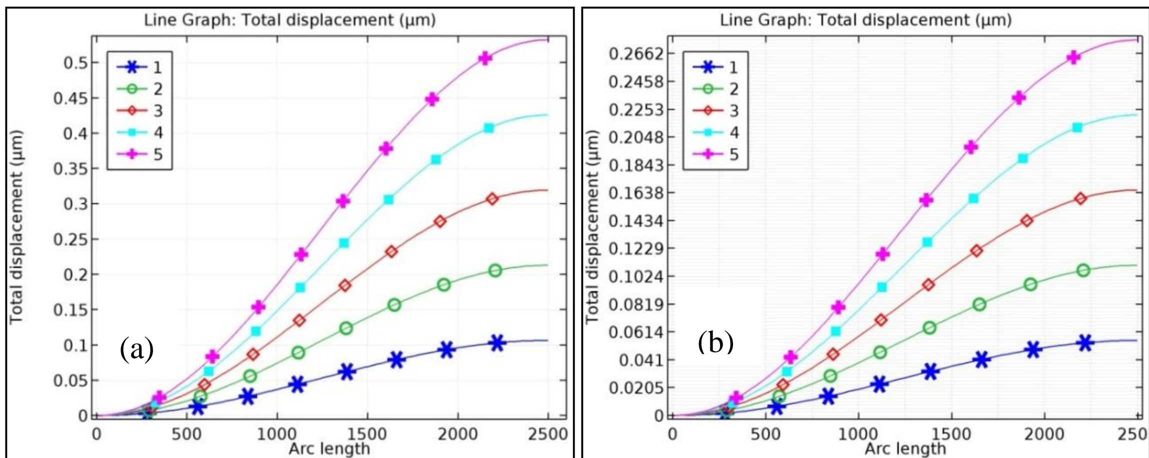

Fig. 4.11 (a). Displacement versus arc length graph for the guided two-beam for input acceleration from 1g to 5g. Maximum displacement 0.107 µm and 0.537 µm is obtained at an input acceleration of 1g and 5g respectively. (b). Displacement versus arc length graph for the guided four-beam for input acceleration from 1g to 5g. Maximum displacement 0.055 µm and 0.279 µm is obtained at an input acceleration of 1g and 5g respectively.

Table 4.3 Comparison of maximum displacement at an input acceleration range of 1g to 5g for guided two-beam and four-beam cantilever structure.

Input acceleration	Maximum displacement for guided two-beam structure	Maximum displacement for guided four-beam structure
1g	0.107 μm	0.055 μm
2g	0.215 μm	0.111 μm
3g	0.322 μm	0.167 μm
4g	0.430 μm	0.223 μm
5g	0.537 μm	0.279 μm

Therefore guided four-beam cantilever structure provides higher stable operation as compared with guided two-beam cantilever structure.

4.3.4 von-Mises Stress

Displacement in the guided beam generates stress along the length of the beam. Tensile and compressive stress is generated at the fixed end and guided end of the beam respectively. A maximum stress of 1.29 x 10^5 N/m^2 is generated at an input acceleration of 1g and 6.49 x 10^5 N/m^2 at an acceleration of 5g across the length of the piezoelectric layer for guided two-beam structure as given by Fig. 4.12 (a). At the fixed end the stress has maximum value which gradually reduces and reaches minimum value at the center (1250 μm) of the beam. As the length increases from center towards the guided end the stress increases gradually and reaches maximum at guided end (2500 μm) which justifies the tensile and compressive stress shown in Fig. 4.12 (a).

Maximum stress of 0.67 x 10^5 N/m^2 is generated at an input acceleration of 1g and 2.6 × 10^5 N/m^2 at an acceleration of 5g across the length of the piezoelectric layer for guided four-beam structure as given by Fig. 4.12 (b). Table 4.4 gives the von-Mises stress values for the guided two-beam and four-beam cantilever structure at an input acceleration range from 1g to 5g. As four-beams are attached with the proof mass at the center therefore, stress is equally distributed on the four-beams generated due to deflection of the seismic mass. Therefore, each beam in guided four-beam cantilever structure exerts lesser stress i.e. 0.67 x 10^5 N/m^2 (at 1g) as compared to guided two-beam cantilever structure where each beam exerts a stress of 1.29 x 10^5 N/m^2. Reduced stress value will further reduce the

risk of fracture of guided beams, therefore guided four-beam cantilever structure will provide a reliable operation as compared to guided two-beam cantilever structure.

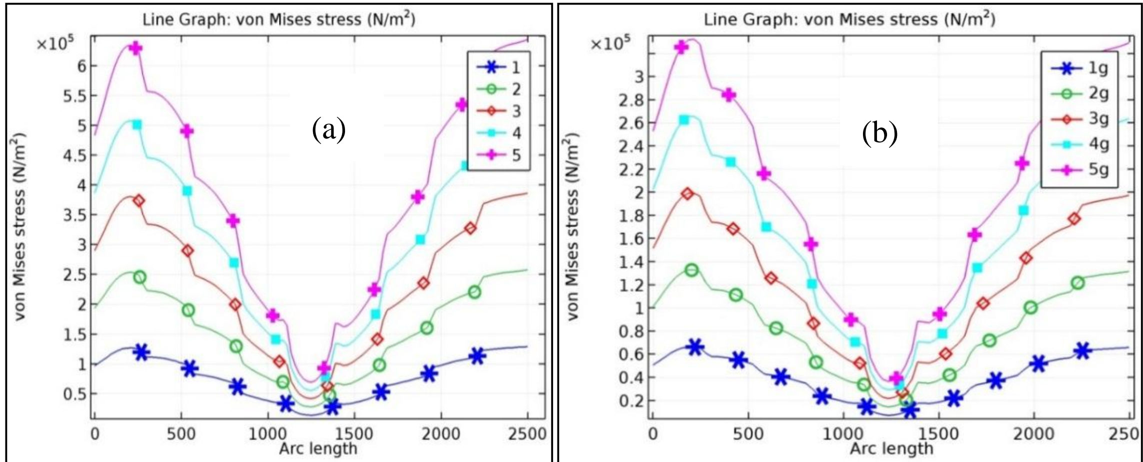

Fig. 4.12 (a). von-Mises stress versus arc length graph for the guided two-beam for input acceleration ranging from 1 to 5 g. Maximum stress values of 1.29 x 10^5 N/m^2 and 6.49 x 10^5 N/m^2 is obtained at an input acceleration of 1g and 5 g respectively. (b) von-Mises stress versus arc length graph for the guided four-beam for input acceleration ranging from 1 to 5 g. Maximum stress values of 0.67 x 10^5 N/m^2 and 2.6 $\times$ 10^5 N/m^2 is obtained at an input acceleration of 1g and 5 g respectively.

Table 4.4 Comparison of von-Mises stress at an input acceleration range of 1g to 5g for guided two-beam and four-beam cantilever structure.

Input acceleration	von-Mises stress for two-beam structure	von-Mises stress for four-beam structure
1g	1.29 x 10^5 N/m^2	0.67 x 10^5 N/m^2
2g	2.59 x 10^5 N/m^2	1.3 x 10^5 N/m^2
3g	3.89 x 10^5 N/m^2	2.01 x 10^5 N/m^2
4g	5.19 x 10^5 N/m^2	2.6 x 10^5 N/m^2
5g	6.49 x 10^5 N/m^2	3.3 x 10^5 N/m^2

4.3.5 Electric potential

Stress across the arc length of the beam generates charge along the piezoelectric material due to inverse piezoelectric effect. Charge of opposite polarities is generated due to tensile and compressive stress at the fixed end and at the guided end of the beam respectively. At the fixed end a maximum potential of 23.62 mV is generated whereas at

the guided end maximum potential generated is -24.28 mV at 1g for guided two-beam structure shown in Fig. 4.13 (a). Maximum potential generated at input acceleration of 1g is -24.28 mV and at acceleration of 5g is -121.38 mV for guided two-beam cantilever structure. Electric potential generated has maximum value at the fixed end due to maximum stress which gradually reduces towards the center of the beam which is minimum stress region. Further electric potential generated increases moving from center of the beam and is maximum at the guided end due to maximum stress as shown in Fig. 4.13 (a).

Guided four-beam structure generates a maximum potential of -12.22 mV at 1g and -61.12 mV at 5g as shown in Fig. 4.13 (b). Table 4.5 compares the values of electric potential generated due to tensile and compressive stress at fixed end and guided of one beam for guided two-beam and four-beam cantilever structure at an input acceleration ranging from 1g to 5g respectively. It can be seen from Table 4.5 that the electric potential generated across a beam for guided two-beam structure is 24.28 mV at 1g which is twice the potential generated across a beam for guided four-beam structure which is 12.22 mV.

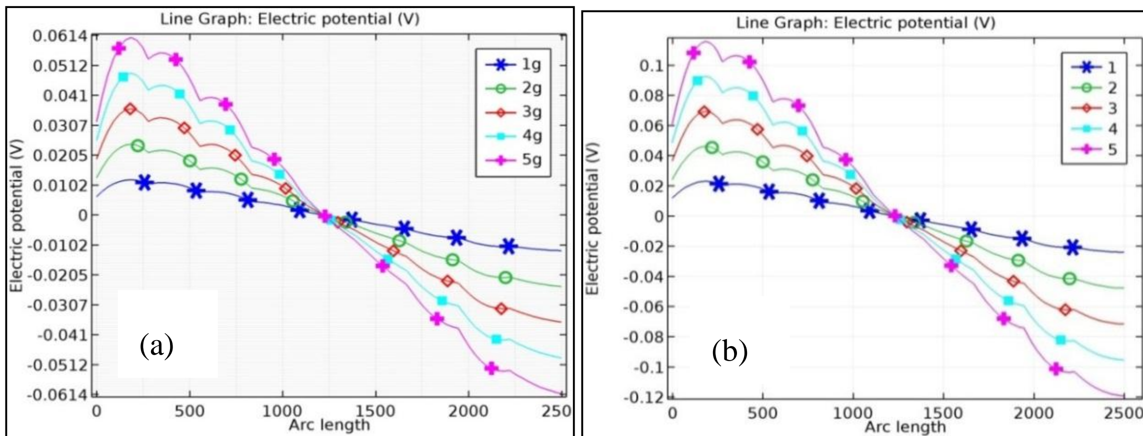

Fig. 4.13 (a). Electric potential versus arc length graph for the guided two-beam for input acceleration from 1g to 5 g. Maximum electric potential of 24.28 mV and 121.38 mV is obtained at an input acceleration of 1g and 5 g respectively. (b). Electric potential versus arc length graph for the guided four-beam for input acceleration from 1g to 5 g. Maximum electric potential of 12.22 mV and 61.12 mV is obtained at an input acceleration of 1g and 5 g respectively. Single beam of guided four-beam structure

generates half the potential (12.22 mV) compared to guided two-beam cantilever structure but the net potential generated by the four-beams would be 48.88 mV (4x 12.22 mV) which is equal to the electric potential generated by two-beams of the guided two-beam cantilever structure.

The case discussed above is based on FEM results where the displacement is exactly double for guided two-beam cantilever structure to that of guided four-beam cantilever structure and could be considered a special case. Experimental results discussed in next chapters show that the displacement for the two structures is not proportional and guided four-beam structure will generate higher potential.

Table 4.5 Summarizes the electric potential generated by one beam of guided four-beam cantilever structure due to tensile and compressive stress at fixed end and guided end.

Input acceleration	Electric potential at fixed end two-beam (mV)	Electric potential at guided end two-beam (mV)	Electric potential at fixed end four-beam (mV)	Electric potential at guided end four-beam (mV)
1g	23.62	-24.28	12.05	-12.22
2g	47.24	-48.55	24.11	-24.45
3g	70.87	-72.83	36.16	-36.67
4g	94.49	-97.11	48.21	-48.9
5g	118.11	-121.38	60.27	-61.12

Guided four-beam cantilever structure gives higher electric potential at smaller displacement and stress which improves the stability and reliability of device operation. Therefore, we conclude that a two-beam and four-beam structures of dimensions 2000 x 2500 μm with central pyramidal proof mass of top dimensions 3500 x 3500 μm and bottom dimensions of 3033 x 3033 μm serve our purpose of generating potential in the range of millivolts under the ambient vibrations.

4.4 Design and Optimization of Split Electrodes for Guided Beam Piezoelectric Energy Harvester

As already discussed, two different tensile and compressive stress are present at the fixed and the guided end of the guided beam type piezoelectric energy harvester. Due to different stress, opposite polarities of charges are generated at fixed and guided end.

Therefore to harvest these charges set of split electrodes are required to collect charges. Marzencki et al. [53] designed and fabricated a guided two-beam piezoelectric energy harvester by designing set of electrodes over the entire beam length. However designing split electrodes is complex and this pattern needs to be optimized. Therefore in this section we optimize the design of the split electrodes for the guided beam type piezoelectric energy harvester. Fig. 4.14 shows variation of displacement and von-Mises stress along the arc length of a beam which is investigated in detail to optimize the dimension and position for the split electrodes. Arc length is the length from fixed end of the beam (0 µm) to the guided end (2500 µm) of the beam where seismic mass is attached. The arc position selected is the interface of the top surface of piezoelectric layer and the top electrode where charge is generated and collected. In Fig. 4.14, region A gives the displacement of the beam from fixed end to 675µm length. Non-linear tensile stress is generated along the beam (region A) which can be described by equation (4.4) with a correlation coefficient of 0.999. Maximum tensile stress of 4.41234×10^5 $N/m^2$is generated at the fixed end which gradually reduces towards the free end.

Maximum tensile stress of 4.41234×10^5 N/m^2 is generated at the fixed end which gradually reduces towards the free end.

$$f(x) = 9.567 \times 10^{-7} x^{1.867} - 0.0010 \qquad 4.4$$

Electrode T1 from 0µm to 675µm defines the split electrode at the fixed end which harvests the maximum tensile stress generating maximum electric potential. Region B from 675 µm to 1825 µm is mostly a linear region which follows equation (4.5) with a correlation coefficient of 0.999. Fig. 4.14 shows that region B is minimal stress region where both the tensile and compressive stress becomes minimal at 1250 µm which is the center point of the beam.

$$f(x) = 0.001073\, x^{1.867} - 0.2917 \qquad 4.5$$

Displacement curve in region C starting from 1825 µm to 2500 µm gives displacement of the beam at guided end.

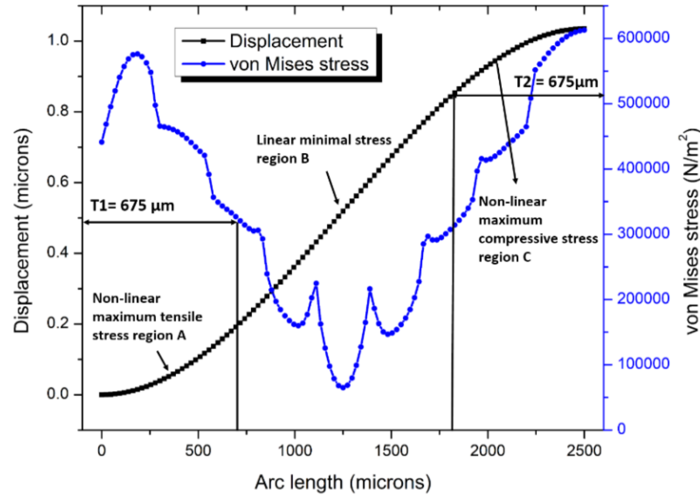

Fig. 4.14 Displacement and von-Mises stress along the length of the beam at1g. Electrodes T1 and T2 placed at region A and C of maximum tensile and compressive stress.

Maximum non-linear compressive stress is generated in the region C as shown in Fig. 4.14 which follows the equation (4.6) with a correlation coefficient of 0.9967.

$$f(x) = -12.549 \times 10^5 x^{-4.126} + 1.118 \qquad 4.6$$

Electrode T2 positioned from 1825 µm to 2500 µm and defines the split electrode at the guided end (where seismic mass is attached). This electrode will harvest maximum compressive stress generating maximum electric potential. Exponentials from equation (4.4) and (4.6) for region A is 1.867 and for region C is - 4.126 which indicates the opposite and unequal behavior of tensile and compressive stress. Compressive stress is higher as it is near to seismic mass where displacement is maximum, Maximum value of compressive stress at guided end is 6.12738 x10^5 N/m^{2}generating maximum potential of -0.10554 volts. Whereas tensile stress at fixed end has maximum value of 4.41234 x10^5 N/m^2 generating maximum potential of 0.098519 volts. From the above analysis it is clear that the split electrodes T1 and T2 each having dimensions as length 675 µm and width 2000 µm operates in maximum tensile and compressive stress regions will generate maximum electric potential. Compressive stress at guided end is higher as compared to tensile stress, due to this higher potential is generated at the guided end. Previous split electrode designs such as discussed by Marzencki et al. [53] deployed set of electrodes on

almost complete beam length, however, the approach suggested in this paper gives better results for harvesting ambient vibrations. Moreover, the designed electrodes reduces the resonance frequency of the energy harvester and increases the total charge generated which is discussed in the next section.

4.4.1 Effect of length of split electrode on resonance frequency

In this section effect of dimension of split electrodes on the resonance frequency of the guided two-beam piezoelectric energy harvester is described.

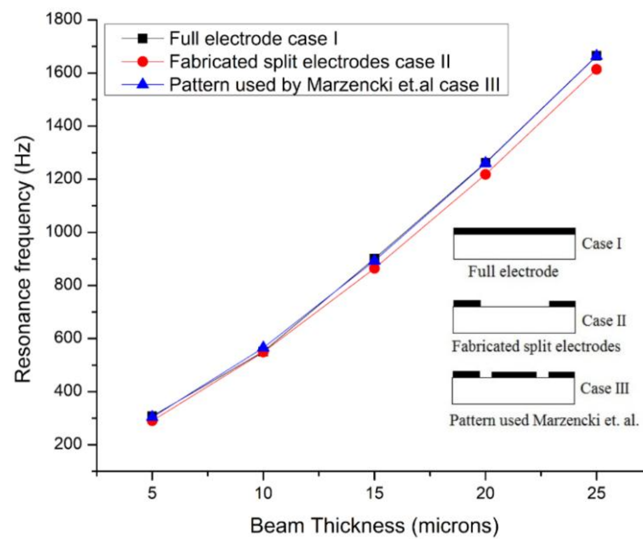

Fig. 4.15 Beam thickness vs. resonance frequency at different electrode pattern.

The three different electrode pattern is shown in Fig. 4.15 are designed and investigated using FEM. Table 4.6 shows the dimensions along with resonance frequency achieved for these three electrode patterns Dimensions of electrodes as for Case I; length as 2500 µm, Case II length as 675 µm and Case III three electrodes pattern used by Marzencki et al. [53] width in all three cases as 2000 µm and thickness as 1 µm. Resonance frequency for beam thickness of 5 µm for Case I is 308 Hz, Case II 290 Hz and for Case III 303 Hz. Resonance frequency for case II is reduced by 18 Hz or 5.8% as compared to case I and 13 Hz or 4.2% as compared to case III which can be seen from Fig. 4.15. At beam thickness of 25µm resonance frequency for Case I is 1664 Hz, Case II is 1613 Hz and for Case III 1663 Hz. Resonance frequency for Case II is reduced by 51 Hz or 3% by case I

and 50 Hz or 3% by case III as shown in Fig. 4.15. Thus Case II gives the least resonance frequency among all the three cases. Also the resonance frequency gets reduced by 18 Hz in low-frequency region which is of interest while tuning the energy harvester in ambient vibration. Therefore, Case II electrode pattern gives better results and therefore this pattern is selected during mask layout design for device fabrication.

Table 4.6 Comparison of resonance frequency for three different electrode patterns

S. No:	t= 5 μm	t = 25 μm	Remarks
Case I	308 Hz	1664 Hz	
Case II	290 Hz	1613 Hz	4.2% less than case III
Case III	303 Hz	1663 Hz	

4.4.2 Effect of length of split electrode on change in capacitance

Displacement in the piezoelectric energy harvester generates stress along the piezoelectric layer which generates electric charge across the electrodes. The change in the capacitance due to displacement of the beam under external vibration is proportional to the charge and potential generated. The effect of length of electrodes on the displacement and change in capacitance on the guided two-beam piezoelectric energy harvester is investigated. Displacement of the guided two-beam structure for electrode length from 675 μm to 2500 μm is obtained using FEM and shown in Fig. 4.16. Displacement of the beams for electrode length of 675 μm at an input acceleration of 1g is 3.11422 μm which gradually reduces with increase in length and is minimum for electrode length of 2500 μm i.e. 2.51441 μm. Thus as the length of the electrode is increased the displacement of the beam reduces, the maximum variation of displacement observed is 0.59981 μm or 19.26 %. The change in capacitance for the piezoelectric energy harvester is calculated using equation (4.7) [103].

$$\Delta C = \frac{xC}{d} \qquad 4.7$$

where ΔC is the change in capacitance, x is the displacement of the beams, C is the static capacitance which is 153 pF experimentally obtained from capacitance-voltage (CV) test, d is the distance between the electrodes which is 2.5 μm (thickness of ZnO layer). In Fig. 4.16 the change in capacitance (ΔC) at different length of electrodes from 675 μm to

2500 μm is shown. Maximum change in capacitance is 190.59026 pF for electrode length of 675 μm which gradually reduces as length of electrode is increased and its minimum value is 153.88189 pF at electrode length of 2500 μm. It is clear that for electrode length of 675 μm change in capacitance value is higher by 36.70837 pF as compared to electrode of length 2500 μm is shown.

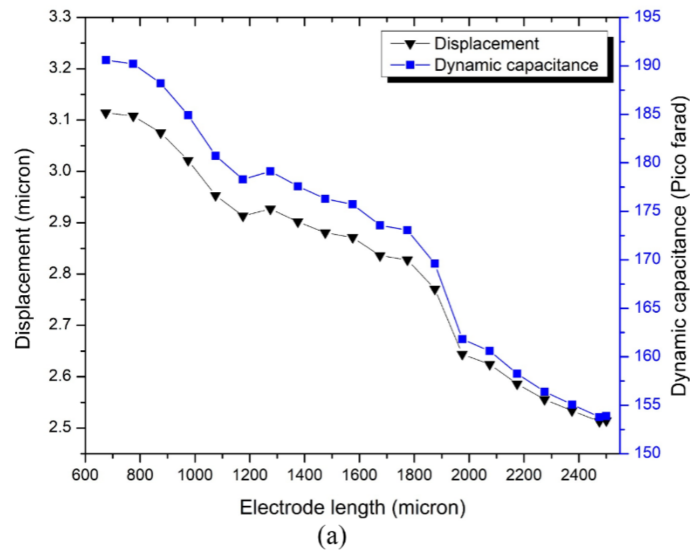

Fig. 4.16 Change in displacement and capacitance due to variation of electrode length from 675 μm to 2500 μm.

Therefore split electrodes of length 675 μm gives maximum displacement and change in capacitance which generates higher electric potential.

The above analysis clearly states that the optimized pattern of split electrodes gives better results by reducing the resonance frequency and by giving higher change in capacitance. Therefore this optimized pattern is selected and fabricated. The individual sensitivity of the split electrodes is also experimentally obtained during vibration bench testing which is presented in detail in Chapter 6.

Chapter 5

Fabrication of Guided Beam Piezoelectric Energy Harvester

5.1 Introduction

Fabrication technology is one of the most significant steps in the realization of a device. It is the technology which puts forward several kinds of limitations in terms of materials used in the device, their processibility, growth, deposition and patterning, realization of mechanical structures, mechanical and physical properties of the material layers, fabrication of electrical and electronic components. A great care is required to develop and to characterize each unit process leading to the technology development for the fabrication of a specific device. The successful technology development is said to be complete when it delivers repeatable and reliable results. Fabrication of MEMS vibration energy harvester, apart from the usual unit processes, which are used in the fabrication of general MEMS devices, requires stringent micromachining techniques [42] for both the devices. However, their fabrication is compatible with our technology and available processing facilities.

In both of these devices a combination of wet and dry bulk micromachining techniques have been utilized. Elaborate experimentation has been done on the development of micromachining processes based on both wet and dry etching techniques in which aqueous TMAH etching for wet bulk micromachining, RIE (reactive ion etching) and DRIE (deep reactive ion etching) have been used for dry bulk micromachining processes.

5.1.1 Fabrication Methodology

The fabrication methodology has to be very well planned as mechanical as well as electrical and piezoelectronic sub-systems have to be fabricated simultaneously. For the

current devices, the fabrication technology is somewhat different [42], and hence need a special care in their development.

In this chapter fabrication of guided two-beam and four-beam piezoelectric energy harvester is presented in detail.

5.2 Design of Mask Layouts

Each fabrication process starts with a set of masks which are used for the fabrication of each material layer or structure in the device. After fixing the dimensions of different structures and layers in the device through design and simulation in Chapter 4, the device has to be fabricated using MEMS fabrication technology. We need different masks for the fabrication of each layer or a structure. A five-level mask process was designed to realize the device. All these masks are summarized in Table 5.1.

Table 5.1 Mask details Device: MEMS-VEH: Die size: 12.5 x 12.5 mm

Sr. No.	Mask ID	Layer Name	Mask Polarity	GDS II No.	Function of the Mask
1	VEH-1	Active	Bright Field	GDS_02_DT_00	TMAH Etching
2	VEH-2	Metal 1	Bright Field	GDS_10_DT_00	Bottom Electrode Patterning (Gold)
3	VEH-3	Metal 4	Bright Field	GDS_16_DT_00	Piezoelectric layer patterning
4	VEH-4	Poly	Bright Field	GDS_04_DT_00	Top Electrode Patterning (Gold)
5	VEH-5	Metal 2	Dark field	GDS_12_DT_00	DRIE for releasing the structure

The combined view of all the five-level masks for two-beam and four-beam devices designed using L-edit is shown in Fig. 5.1 (a) and (b). Mask #1 is for is for wet TMAH etching for pyramidal shape seismic mass. Mask #2 is for bottom electrode patterning. Mask #3 is for ZnO patterning. Mask #4 is for top electrode patterning having dimensions as 675 µm for the two electrodes T1 and T2. Mask #5 is for release of guided beams by DRIE from the front side. Grid of 2000 µm is designed to define the fixed end

of the beams and to define the electrode pads of 600x 600 µm on both sides as shown in Fig. 5.1 (a). These masks are now described in detail.

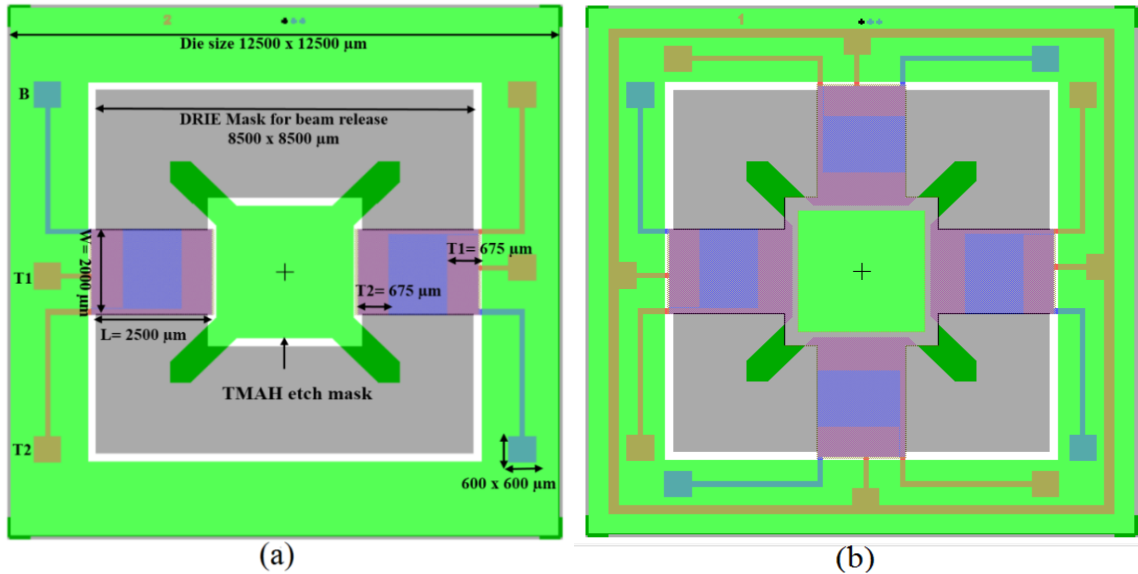

Fig. 5.1 (a) 5 - Level mask layout for guided two-beam device (b) 5 - Level mask layout for guided four-beam device.

5.2.1 Mask #1: TMAH Etch mask for Pyramidal shape seismic mass

As already stated, the pyramidal shape seismic mass in our design is realized using TMAH CMOS compatible 25 wt.% wet etching because it gives an etch angle of 54.74 º for <100> plane. Mask #1 is designed for TMAH etching to realize pyramidal shape seismic mass. Fig. 5.2 (a) gives the layout of TMAH opening mask from the back side. The designed mask is a bright field mask, the bottom opening area for the TMAH mask is calculated from equation 5.1 where b1 is the bottom side opening area, b0 is from front side area and t_d is etch depth.

$$b1 = b0 + \sqrt{2}t_d \tag{5.1}$$

For an etch depth (t_d) of 330 µm and b0 as 8500 x 8500 µm bottom opening b1 is calculated 8966.690 x 8966.690 µm. Where b0 is the dimension from front side i.e. 8500 x 8500 µm. Lateral etching during TMAH process must be taken into account which gives the bottom opening of 8916 x 8916 µm. Similarly the seismic mass dimension from bottom is also calculated using equation 5.1 and after lateral etching compensation gives

dimensions of seismic mass as 3083 x 3083 μm from the bottom side as seen from Fig. 5.2 (a).

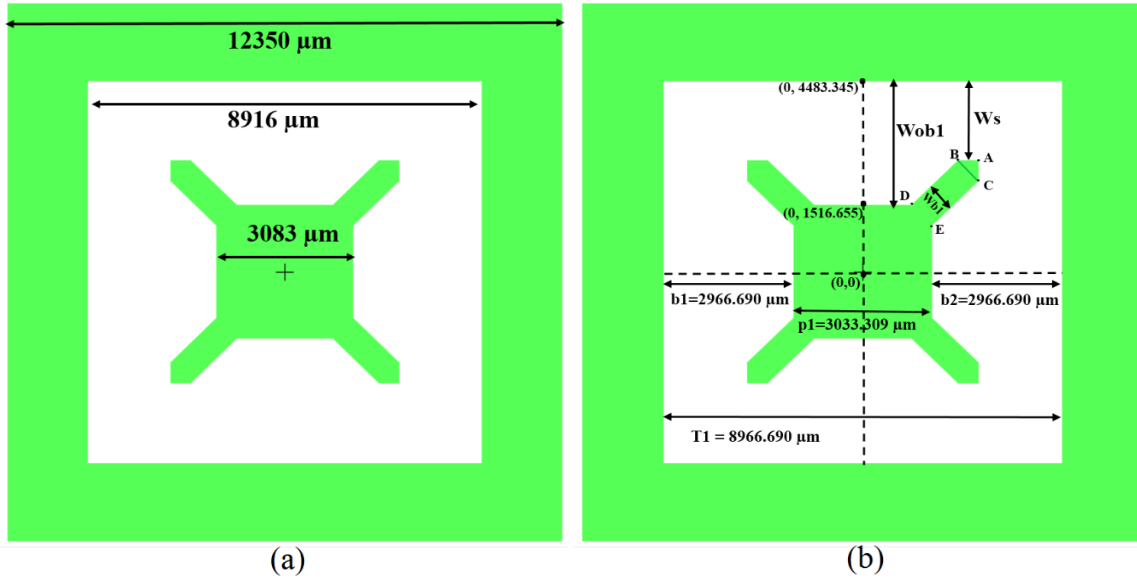

Fig. 5.2 (a) TMAH opening mask #1 for pyramidal shape seismic mass. (b) Corner compensation design to obtain perfect edges of seismic mass

5.2.1.1 Corner Compensation

As we know that convex corners of a structure become round or rather de-shaped because of the presence of high index planes at the corners in wet bulk micromachining, we need to mask these corners with structures which are known corner compensating structures. Therefore, corner compensation is used to obtain perfect edges at the bottom vertex for pyramidal shape seismic mass. Thin bar corner compensation is used for the energy harvester device. From Fig. 5.2 (b) gives dimensions of Wob1 as 2966.690 μm, Wb1 the width of the bar is 660 μm (2td). Ws is calculated from equation 5.2 having dimension 1926.127 μm. Where ratio (R(311)/R(100)) is 2.23.

$$W_{ob1} = W_s + 1.414\frac{R(311)}{R(100)}t_d \quad 5.2$$

From Ws, coordinates for A point is obtained as (2557.217, 2557.217). Point B is calculated as (2090.526, 2557.217) (cos45 °x 660 = 466.690). Similarly point C, (2557.217, 2090.526), point D, (1049.964, 1516.654) and point E as (1516.654,

1049.964) respectively. Length of the bar (BD) is obtained from the coordinates and is calculated as 1471.577 µm.

5.2.2 Mask #2: Bottom electrode patterning

Mask #2 is a bright field mask designed for bottom electrode patterning. The electrodes are placed on the guided two-beam and four-beam device. The dimensions of the electrodes are 2700 x 1980 µm and the pads for connections are 600 x 600 µm as shown in Fig. 5.3 (a), (b).

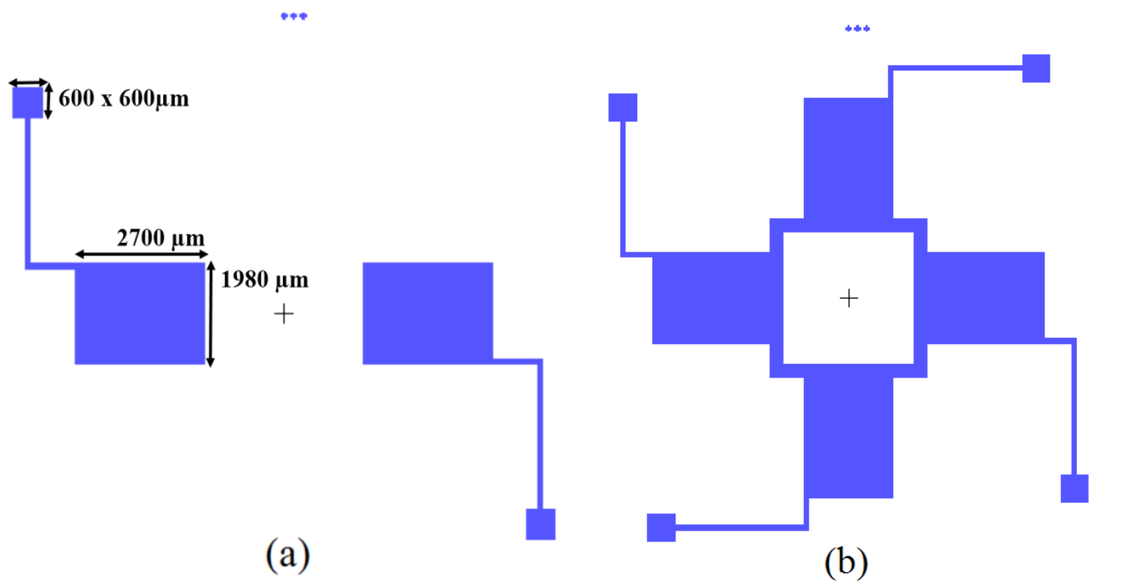

Fig. 5.3 Mask #2 for bottom electrode patterning for (a) two-beam device (b) four-beam device.

5.2.3 Mask #3: Piezoelectric layer patterning

Mask #3 is a bright field mask designed for piezoelectric layer patterning. The piezoelectric film is patterned on the beams having dimensions 2800 x 2000 µm as shown in Fig. 5.4 (a), (b).

5.2.4 Mask #4: Top electrode patterning

Mask #4 is a bright field mask designed for top electrode patterning. The split electrodes are placed on the guided two-beam and four-beam device. Electrode T1 is at the fixed end of the beam and electrode T2 is at the guided end of the beam. The dimensions of both electrodes T1 and T2 is 675 µm as shown in Fig. 5.5 (a), (b).

Fig. 5.4 Mask #3 for piezoelectric layer patterning (a) two-beam device (b) four-beam device.

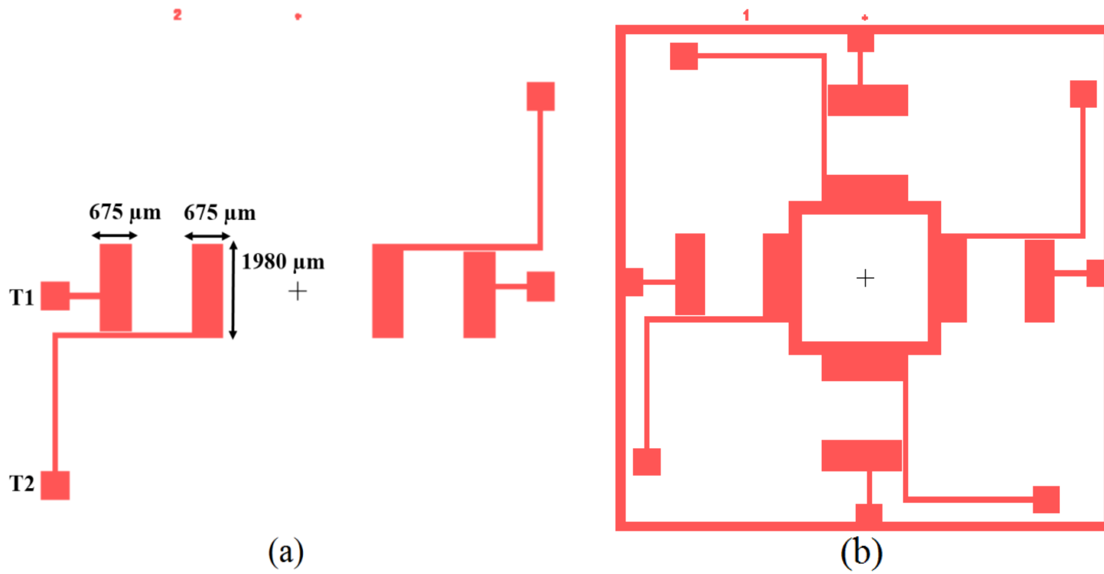

Fig. 5.5 Mask #4 for top electrode patterning (a) two-beam device (b) four-beam device.

5.2.5 Mask #5: DRIE Etch

Mask #5 is a dark field mask designed for beam release using DRIE from front side. The two and four-beams are realized by etching the silicon using DRIE from front side using mask patterns as shown in Fig. 5.6 (a), (b).

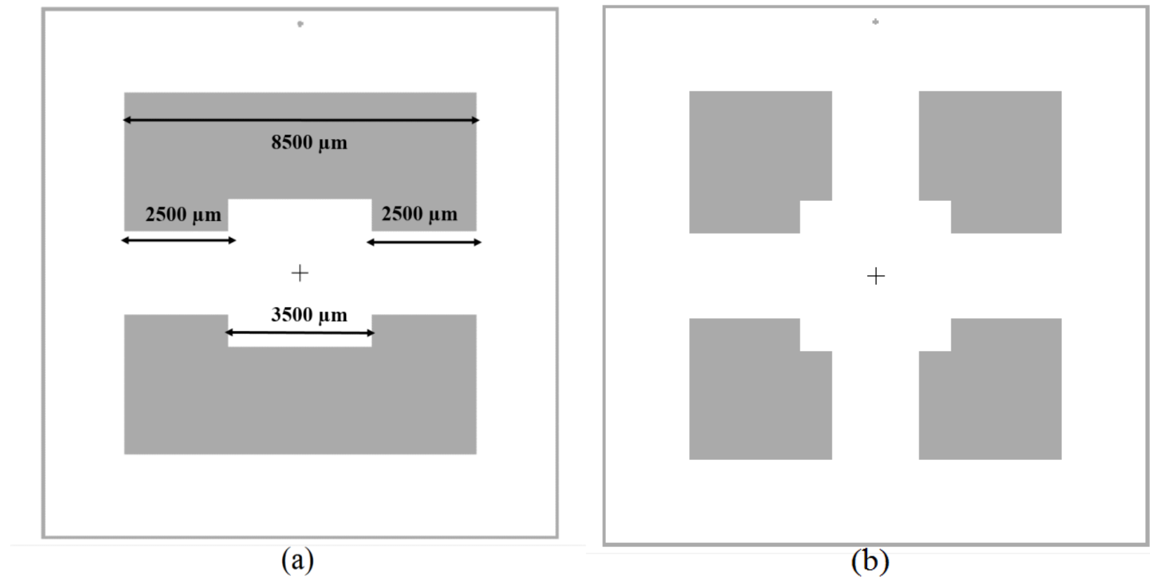

Fig. 5.6 Mask #5 DRIE etching (a) two-beam device (b) four-beam device.

5.3 Fabrication of guided beam piezoelectric energy harvester

Guided two-beam and four-beam energy harvester devices are fabricated using MEMS fabrication processes. Bulk-micromachining is done using Tetra Methyl Ammonium Hydroxide (TMAH) CMOS compatible 25 wt.% wet etching to realize pyramidal shape seismic mass and deep reactive ion etching (DRIE) is done from front side to release two-beam and four-beam structures in the device.

5.3.1 Device Fabrication Flow

The major process steps for the fabrication of the energy harvester device are tabulated in Table 5.2, whereas the fabrication process flow is illustrated in Fig. 5.7.

Table 5.2 Fabrication Steps

1.	Thorough cleaning of wafers: degreasing and chemical cleaning
2.	Wet Oxidation: 0.6 μm thick [103]
3.	Deposition of LPCVD nitride 0.2 μm
4.	Back side patterning **(Lithography M#1)** and Oxide + nitride etching: definition of proof mass
5.	Wet bulk micromachining (WBMM) in TMAH: formation of proof mass [103]
6.	Front side etching of LPCVD nitride and oxide [104]
7.	Dry oxidation: quality oxide for electrical isolation
8.	RF sputtering : Cr/Au for bottom Electrode [103]
9.	Patterning **(Lithography M#2)**and etching of Cr/Au: Bottom Electrode formation
10.	Deposition of ZnO Piezoelectric Layer by Reactive sputtering of Zn
11.	Patterning of ZnO **(Lithography M#3)** [104]
12.	Wet etching of ZnO layer [104]
13.	Metal deposition for top split electrodes: RF sputtering: Cr/Au [104]
14.	Patterning **(Lithography M#4)** definition of top electrodes [104]
15.	Wet Etching: Cr/Au: formation of Top electrodes
16.	**Lithography M#5** for release of beams from front side [105]
17.	DRIE of Si from front side: release of guided beams (developed)
18.	Separating the dies: self-release through DRIE of Si (developed)
19.	Packaging of device in pre-fabricated PCBs (developed)
20.	Wire bonding (on PCB) optimized
21.	Testing and characterization (designed and developed circuitary)

The process flow is illustrated in the following flow diagram:

5.3.2 Device fabrication (Batch 1)

Device fabrication was started with a batch of six number of P-type silicon single crystal <100> double side polished (DSP) wafers of diameter 3 inches and thickness 350±25 μm and having resistivity 1-10 ohm.cm. These specifications of the wafers were selected on the basis of their suitability to realize the designed dimensions of pyramidal shape seismic mass using wet TMAH etching [103]. The device fabrication is carried out as per the process flow steps in Table 5.2. Thorough cleaning of the wafers was done in two steps: degreasing and chemical cleaning. After degreasing of the wafers, chemical cleaning was done using piranha. Piranha cleaning of the wafers is done using H_2SO_4 and H_2O_2 in the ratio of 3:1 followed by thorough deionized water (DI) water rinsing [104]. HF and DI water solution (1:100) dip are given to remove the oxide followed by

thorough DI rinsing [103]. The 0.6 μm thermal oxide layer is grown at 1000ºC followed by 0.2 μm of LPCVD nitride deposition which acts as mask during TMAH etching.

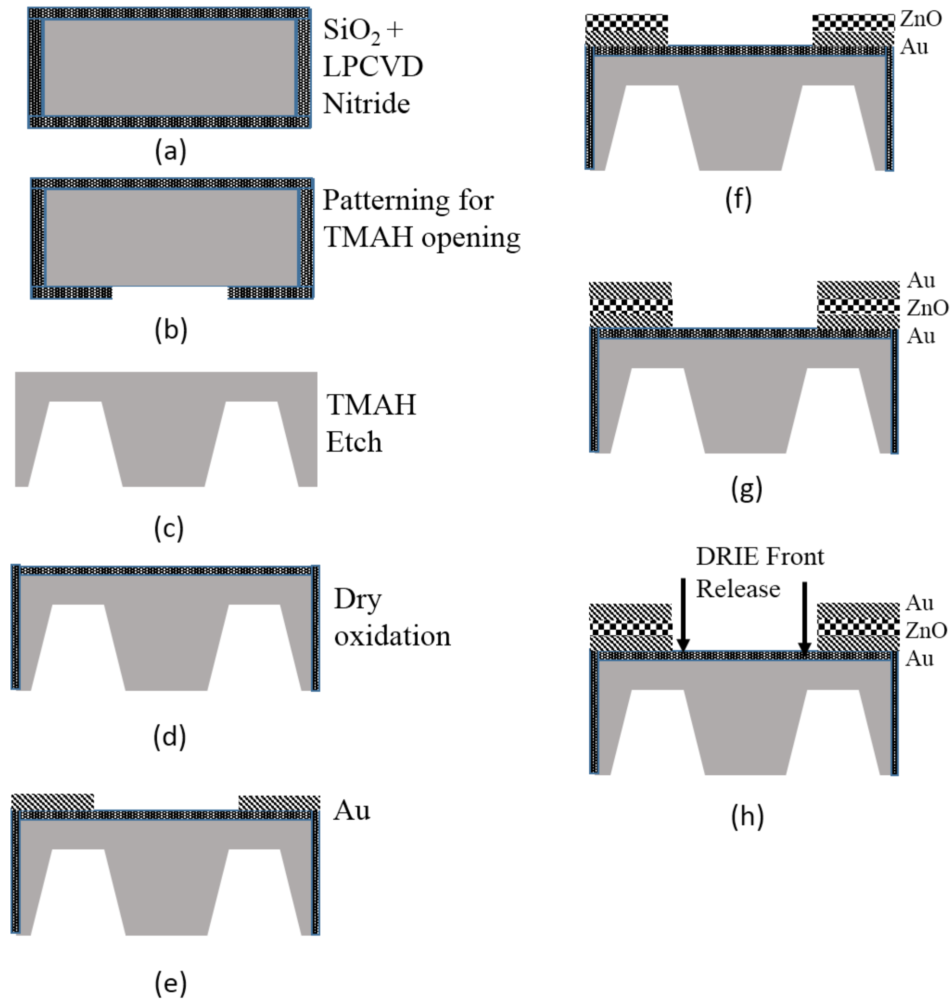

Fig. 5.7 Fabrication flow steps of the device (a) Thermal oxidation and LPCVD nitride deposition (b) Oxide patterning for pyramidal shape seismic mass (mask #1)and etching (c) TMAH etching. (d) Dry oxidation (e) Cr-Gold deposition and patterning (mask #2)(f) ZnO deposition and patterning (mask #3) (g) Gold deposition and patterning (mask #4). (h) Patterning for release of guided beams (mask #5).

Photolithography (Mask #1) is performed for TMAH opening to perform wet etching. Positive photoresist S1818 is used and CD26 its corresponding developer for masking the desired pattern followed by reactive ion etching (RIE). Wafers are subjected to bulk-micromachining of Si in 25% wet TMAH etching at 79ºC giving an etch rate of 20

μm/hr. Dry oxidation of 0.1 μm is performed to act as an insulation between silicon and bottom electrode. Gold sputtering (0.2 μm) followed by patterning (mask #2) and etching is done to form the bottom electrode. A 2 μm thick ZnO layer using RF magnetron sputtering is deposited followed by patterning (mask #3) and wet etching to form the piezoelectric layer. Gold sputtering (0.2 μm) followed by patterning (mask #4) and etching is done to form the top electrode. The photolithography (Mask #5) is done using positive photoresist S1818 and wafer is patterned from front side. DRIE is performed from the front side of the wafer to release the two-beam and four-beam device.

5.4 Detailed unit processes

In this section, the unit processes used for the fabrication of the devices are described in detail.

5.4.1 Cleaning

Piranha cleaning of the wafers is done on inorganic wet chemical bench using H_2SO_4 and H_2O_2 in the ratio of 3:1 for 15 minutes followed by multiple times thorough deionized (DI) water rinsing holding wafers vertically in a Teflon boat as shown in Fig. 5.8 (a). After piranha cleaning, HF and DI water solution (1:100) dip are given in a Teflon beaker to remove the oxide formed due to piranha cleaning followed by thorough DI water rinsing as shown in Fig. 5.8 (b). The silicon wafer surface becomes hydrophobic after HF dip giving clean silicon surface required for thermal oxidation.

Fig. 5.8 (a) Piranha cleaning of wafers. (b) HF dip of wafers for oxide removal.

5.4.2 Thermal oxidation and LPCVD nitride

Thermal oxidation followed by LPCVD nitride deposition is done which act as mask during TMAH etching. The batch of clean wafers is loaded to furnace for thermal oxidation as shown in Fig. 5.9 (a). Thermal oxidation is done at 1100° C for 10-60-10 minutes (dry-wet-dry) giving oxide thickness of ~ 0.6 µm. Low-pressure chemical vapor deposition (LPCVD) nitride deposition is done immediately after the oxidation process. Wafers are loaded in LPCVD furnace as shown in Fig. 5.9 (b) for nitride deposition. A uniform thickness of nitride ranging from 0.17 to 0.2 µm is deposited which act as masking layer during TMAH etching.

Fig. 5.9 (a) Wafers loading in thermal oxidation furnace. (b) Wafers loading in LPCVD nitride furnace.

5.4.3 Lithography (Mask #1) for pyramidal shape seismic mass

Lithography using Mask #1 is done for wet TMAH etching to realize the pyramidal shape seismic mass using bulk micromachining. The wafers are thoroughly cleaned using piranha cleaning followed by DI water rinsing. The wafers are kept in oven for moisture bake for 30 minutes at 120ºC. Fig. 5.10 (a) shows the lithography spin coating bench where photoresist (PR) is coated. Positive photoresist S1818 is coated on the wafer using recipe from spin coater which gives required PR thickness of 3 µm as shown in Fig. 5.10 (b). The batch of six wafers is PR coated with the same recipe. After PR coating the wafers are soft baked (pre-baked) for 30 minutes at 90ºC. The wafer is aligned with Mask #1 with the SUSS MicroTec lithography machine as shown in Fig. 5.11(a).

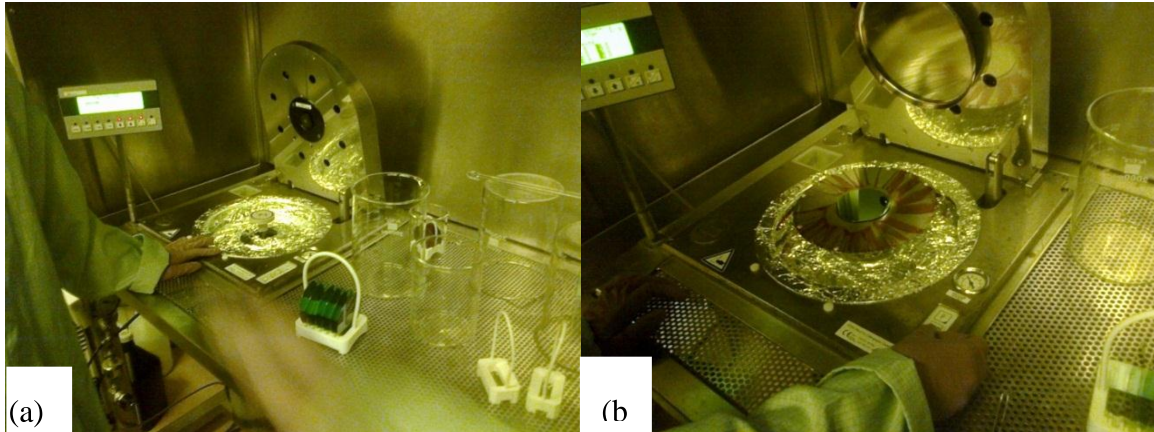

Fig. 5.10 (a) Wafers after moisture bake for photoresist coating. (b) Positive photoresist S1818 coating process on spin coater.

After proper alignment, the Ultraviolet (UV) exposure is done using the SUSS Micro Tec. UV exposure of 6 sec is done for three times as seen from Fig. 5.11 (b).

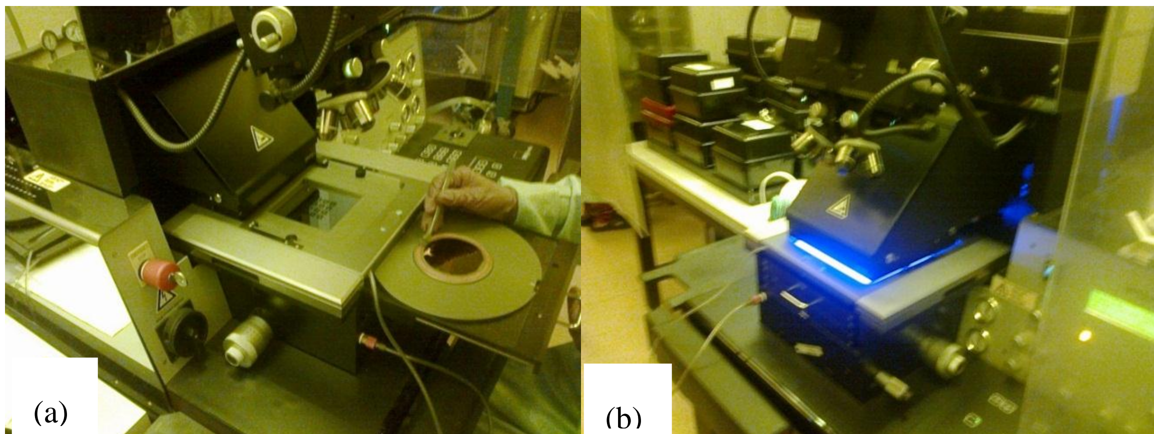

Fig. 5.11 (a) PR coated wafer alignment with mask #1. (b) Exposure of the wafer through mask #1.

After the exposure, the pattern is developed using developer CD26 (shown in Fig. 5.12 (a)) corresponding to the positive photoresist S1818. The developing process is done by dipping the wafers in the developer for 50 seconds followed by rinsing in DI water as shown in Fig. 5.12 (b). This process is repeated for the batch of six wafers. After thorough rinsing, the wafers are nitrogen dried and are hard baked (post baked) for 30 minutes at 120ºC.

Fig. 5.12 (a) Developer CD26 (left) and two DI water beakers. (b) Developing UV exposed PR coated wafer in CD26 developer.

5.4.4 Reactive ion etching (RIE) for oxide and nitride etch

After the lithography with mask #1 is done the oxide (0.6 μm) and nitride (0.2 μm) is selectively etched using reactive ion etching. The white area as shown in mask #1 (Fig. 5.3 (a)) is TMAH opening for wet etching from where oxide and nitride are etched using RIE. Process parameters are gas flow SF6 (2.1 sccm), CF4 (34.9 sccm), power 100 Watt. Fig. 5.13 (a) shows the loading of the six wafers into RIE. Fig. 5.13 (b) shows the plasma generation during etching process. The plasma etches the unprotected PR area.

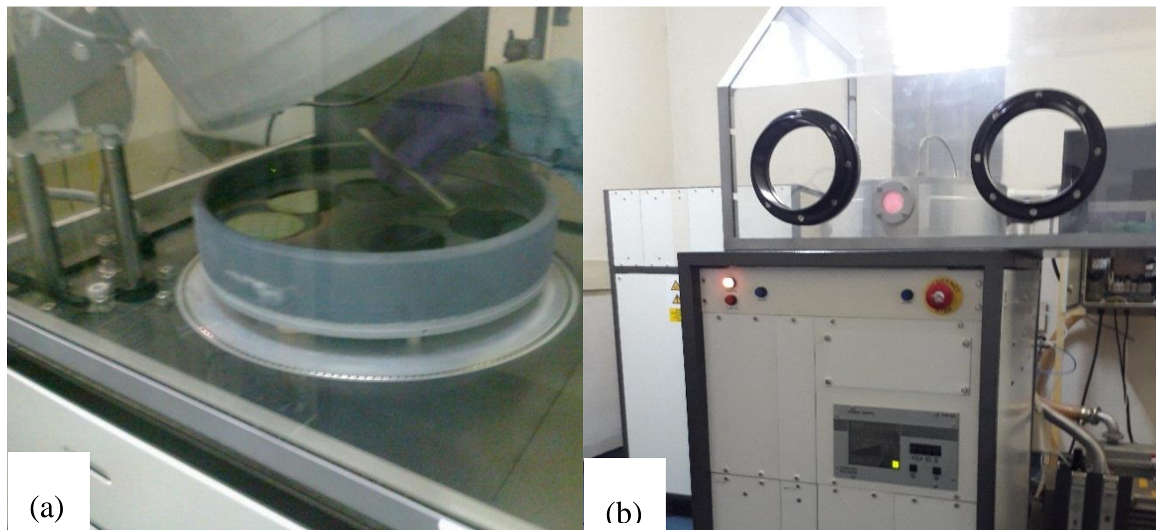

Fig. 5.13 (a) Wafers loading in RIE machine (b) Plasma etching during the process.

5.4.5 Bulk-Micromachining of silicon for pyramidal shape seismic mass

After RIE of nitride and oxide, PR removal for the wafers is done by rinsing in acetone first and again boiling in acetone for 10 minutes. (boiling temperature of acetone is 56° C). After DI water rinse and nitrogen drying the wafers are put in TMAH setup as shown in Fig. 5.14 (a), at a temperature of 90°C first for 4 hours and using profilometer the thickness measured is 140 μm giving an etch rate of 35 μm per hour. Second interval for TMAH 90°C is done and 256.3 μm is etched measured using profilometer. TMAH etch for wafers done in the third interval for 3.5 hours etching 292 microns in fourth interval for 30 minutes and 8 minutes in fifth interval reaching a final thickness of 345 to 352 μm. Fig. 5.14 (b) shows the pyramidal shape seismic mass obtained after TMAH etching. The diaphragm thickness left is 20 – 25 μm.

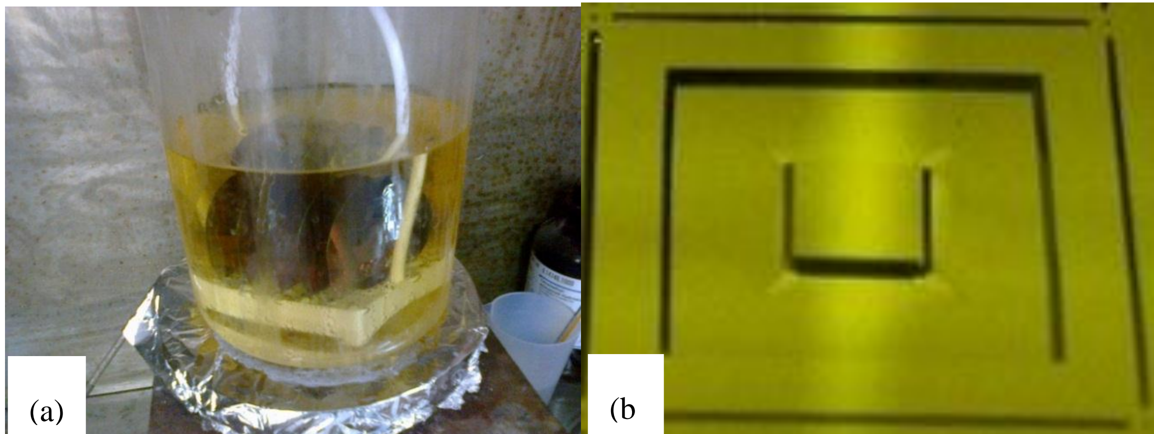

Fig. 5.14 (a) TMAH setup during etching process. (b) Seismic mass obtained after etching.

After TMAH etching the wafers are undergone piranha cleaning (mild). Concentrated HF dip is given to the wafers for oxide and nitride removal as shown in Fig. 5.15 (a). Dry thermal oxidation of ~0.1 micron is grown on the wafers shown in Fig. 5.15 (b) which actas insulation layer between silicon and electrodes on the front side of the wafer.

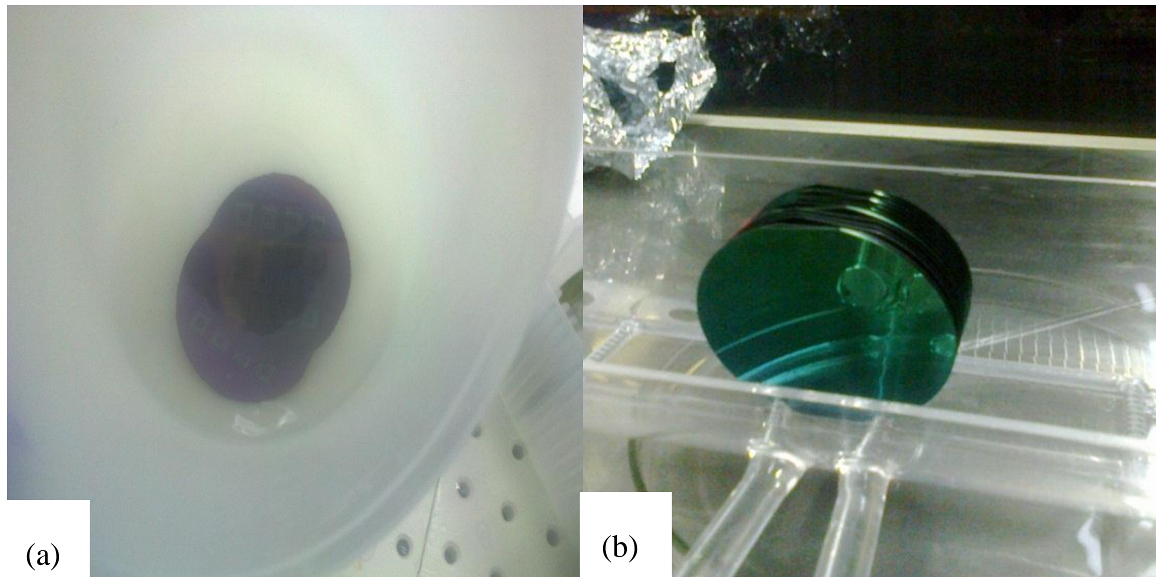

Fig. 5.15 (a) HF dip of wafers for oxide and nitride removal (b) Dry oxidized wafers.

5.4.6 Gold sputtering and bottom electrode patterning (Mask #2)

After dry oxidation, piranha cleaning of the wafers is done followed by DI water rinsing and N2 drying. Sputtering of Chrome/gold (0.02/0.2μm) is done on the front side of the wafers. Mask #2 is used to pattern the wafers to form the bottom electrodes. Same lithography procedure is followed as described above. The PR of thickness 1.3 μm is coated. The TMAH etching is done on the bottom-side of the wafer and the gold deposited is on the front-side of the wafer, this requires back-side alignment of the wafers from mask #2. This is done by aligning the front side from the rectangle shaped alignment marks specifically designed to sustain TMAH etching as shown in Fig. 5.16 (a). The UV exposure is given for 6 seconds two times and is developed as shown in Fig. 5.16 (b).

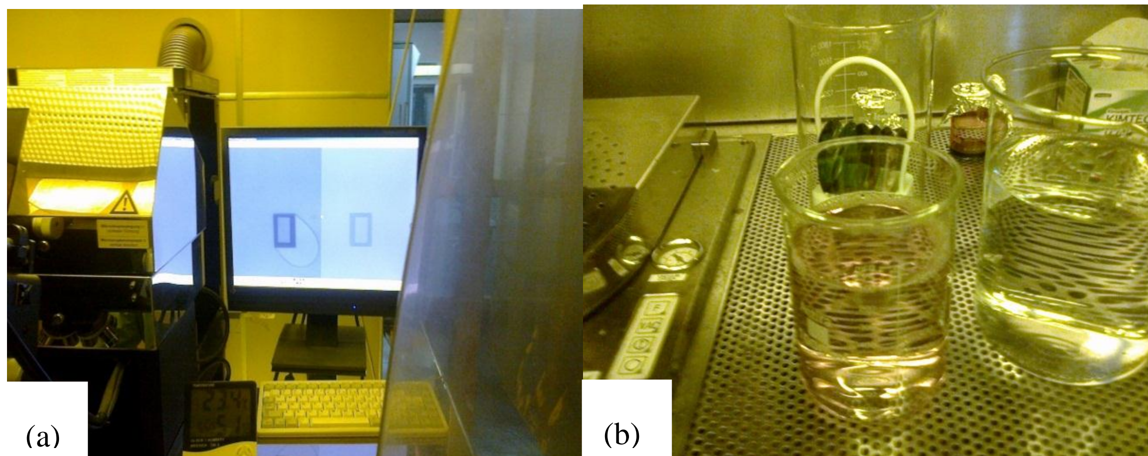

Fig. 5.16 (a) Back side alignment for bottom electrode patterning. (b) Developing pattered wafers.

The wafers are hard baked and then wet etching of the patterned wafer is done. The gold etchant is used to etch the gold and the PR is removed and then chromium is etched in chrome etchant. The wafers are rinsed in DI water after etching as shown in Fig. 5.17 (a). Fig. 5.17(b) shows the patterned bottom electrode wafer.

Fig. 5.17 (a) Chrome/gold etching of wafers. (b) Patterned bottom electrode wafer.

5.4.7 Piezoelectric layer (Zinc oxide) sputtering and patterning (mask #3)

Zinc oxide (ZnO) is the piezoelectric material selected for deposition as it has good piezoelectric properties and is CMOS compatible. A highly c-axis oriented piezoelectric film is deposited using Reactive magnetron sputtering (Hind High Vacuum, Pvt. Ltd.). The following parameters are used for ZnO deposition: Power: 450 Watt, gases used are

Argon: 26 sccm and Oxygen: 39 sccm, pressure: 26 mtorr giving a deposition rate of 0.5 µm/hr. The total deposition time is 4 hours giving a thickness of 2 µm. Wafer having bottom electrodes are cleaned by degreasing process. Wafers are boiled in trichloroethylene (TCE) for 15 minutes, followed by acetone boiling for 15 minutes and then isopropyl alcohol (IPA). After thorough rinsing by DI water and nitrogen drying the wafer is mounted on holder of the sputtering machine as shown in Fig. 5.18 (a). Fig. 5.18 (b) shows the ZnO deposition in process.

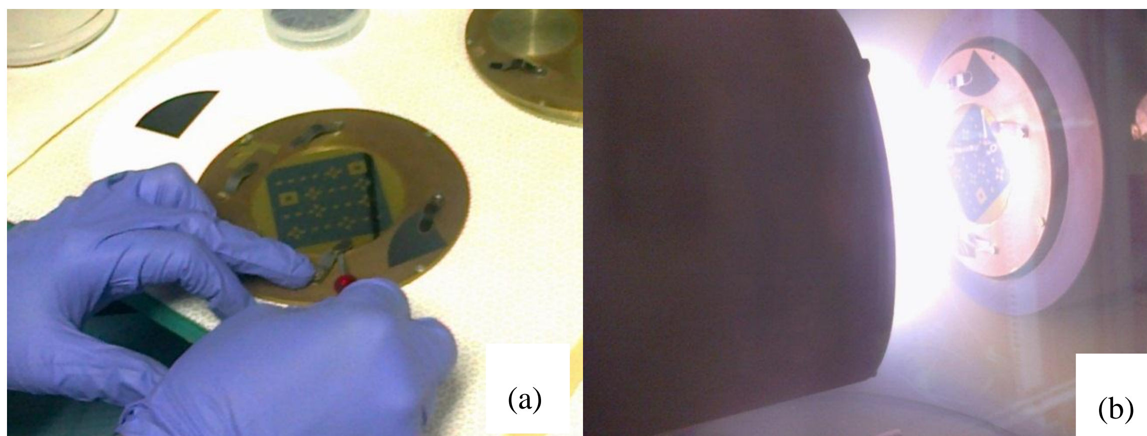

Fig. 5.18 (a) Wafer mounting on holder of ZnO sputtering machine. (b) ZnO deposition in process.

Mask #3 is used to pattern the ZnO layer using the positive PR and the etching of ZnO layer is done using dilute HCl solution.

5.4.8 Gold sputtering and top electrode patterning (Mask #4)

Degreasing is done to clean the wafers. Sputtering of Chrome/gold (0.02/0.2µm) is done on the front-side the wafers. Mask #4 is used to pattern the wafers to form the top electrodes. Same lithography procedure is followed as described above. The PR of thickness 1.3 µm is coated. The gold etchant is used to etch the gold and the PR is removed and then chromium is etched in chrome etchant. Fig. 5.19 (a) shows the patterned top electrode wafer. The Zeta image of top electrode pattern is shown in Fig. 5.19 (b).

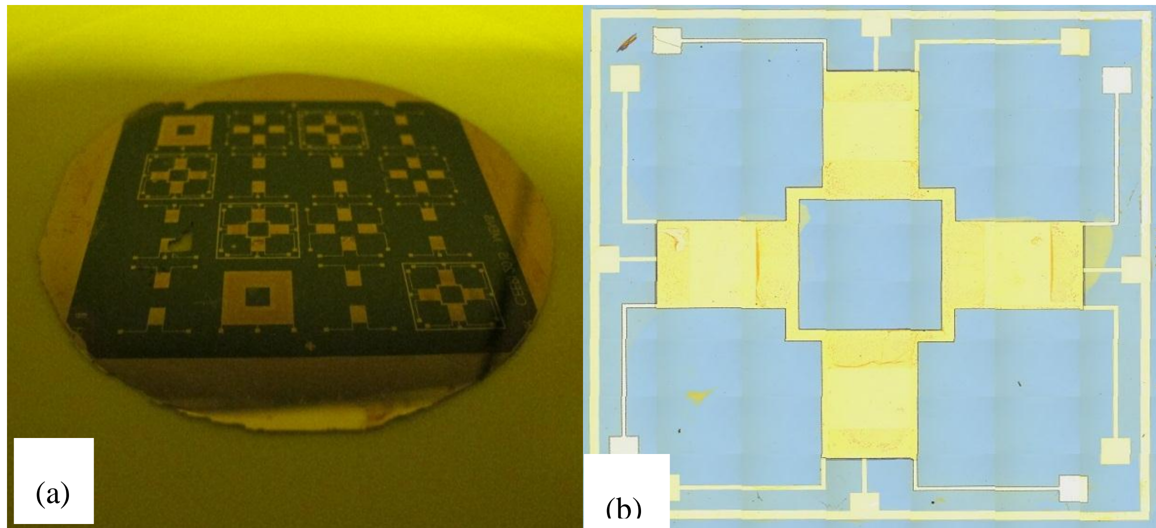

Fig. 5.19 (a) Patterned top electrode wafer (b) Zeta image of the device from the front showing the top and bottom electrode pattern.

5.4.9 Lithography mask #5 and beam release using DRIE

The two-beam and the four-beam devices are released from the front side using deep reactive ion etching (DRIE). Mask #5 is used to pattern the front side of the wafer for drie, after lithography the wafer is stick to six-inch wafer as the DRIE machine takes six-inch samples. Fig. 5.20 (a), (b) shows top and lateral view of the process wafer stick to six inch wafer.

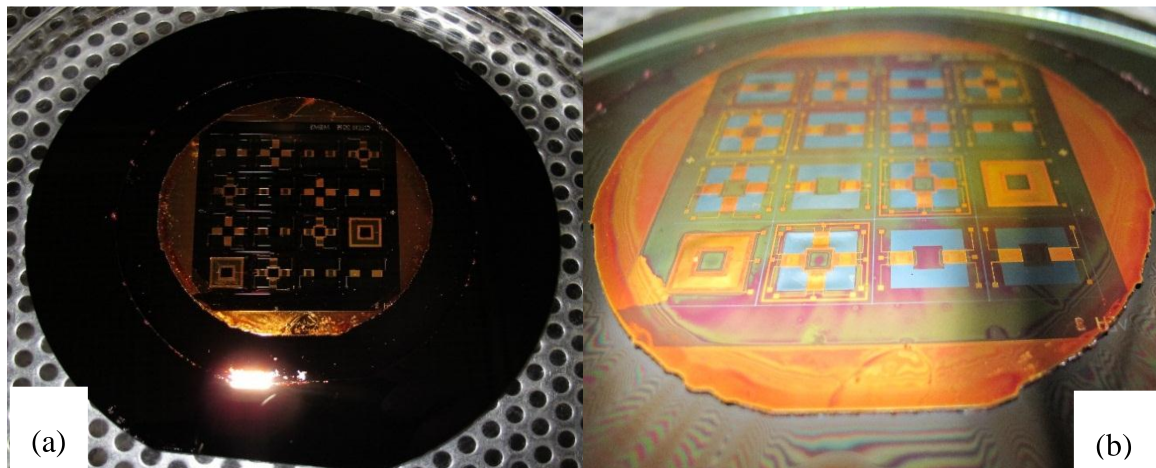

Fig. 5.20 (a) Wafer stick to six-inch wafer after lithography. (b) Lateral view of the wafer.

DRIE is done from the front side of the wafer, after etching around 25 µm of silicon from the front the guided two and four-beam are released. Fig. 5.21 (a), (b) shows the top view and lateral view of beam release after DRIE.

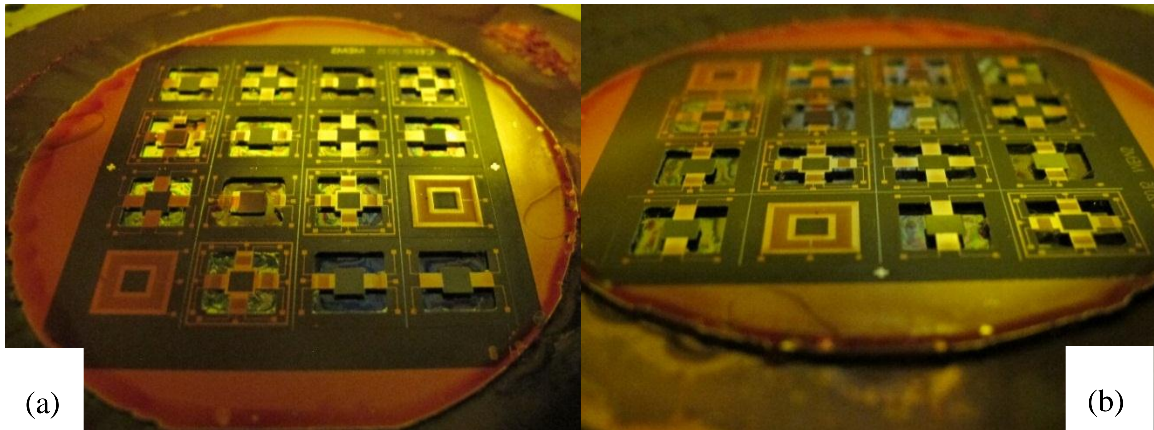

Fig. 5.21 (a) Beam release after DRIE. (b) Lateral view of the released beams.

After DRIE, positive photoresist is removed in acetone shown in Fig. 5.22 (a) and the wafer with released beams is obtained as shown in Fig. 5.22 (b)

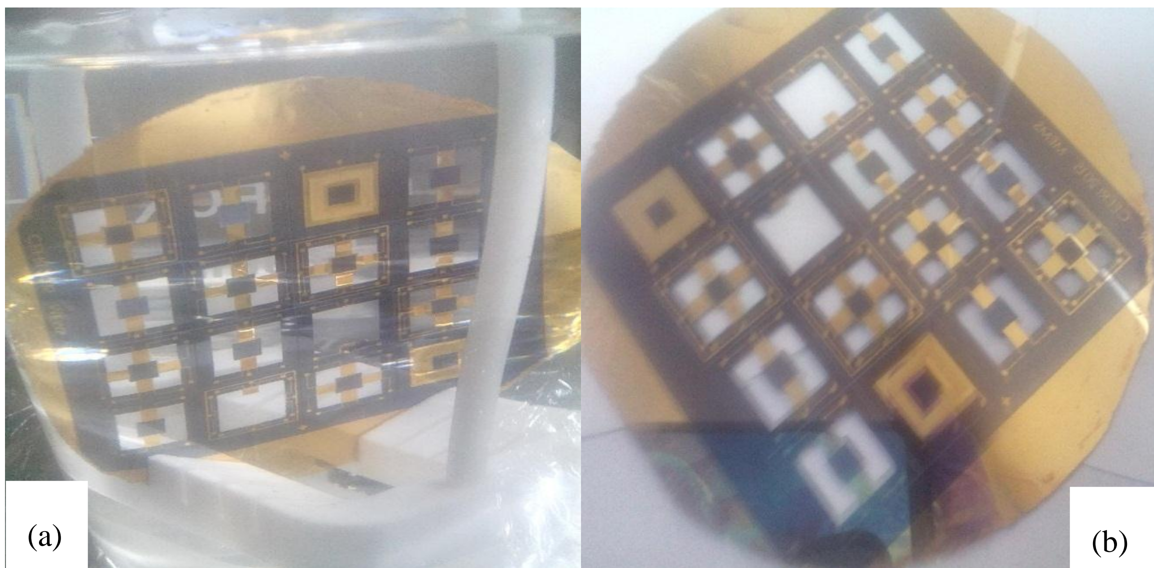

Fig. 5.22 (a) PR removal after DRIE. (b) Wafer with released beams.

5.4.10 Dicing and device release

The devices are diced manually from the grid line designed in mask #1 and mask #5. Fig. 5.23 (a), (b) shows the snapshot of fabricated guided (a) two-beam and (b) four-beam piezoelectric energy harvester.

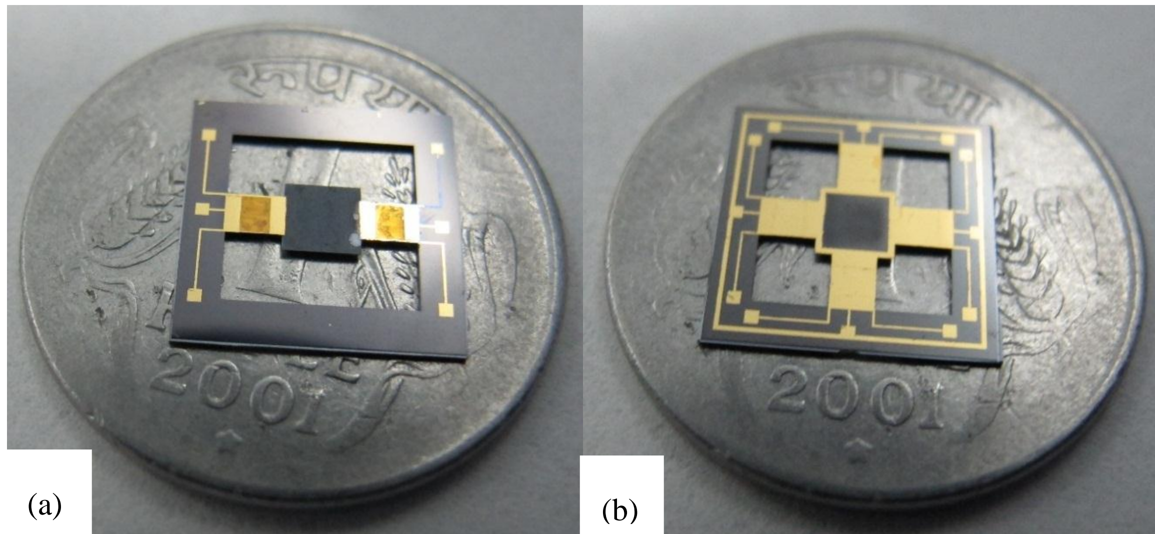

Fig. 5.23 Snapshot of fabricated guided (a) two-beam and (b) four-beam piezoelectric energy harvester.

5.4.11 Discussions

The fabricated devices are successfully separated and tested for resonance frequency. A laser Doppler vibrometer test is done which is used to determine the resonance frequency of the two-beam and four-beam device. The device operates in dominant frequency mode and gives displacement in ±Z direction which is discussed in detail in the next chapter. The resonance frequency measured experimentally for two-beam device is 1971 Hz and for four-beam device is 2540 Hz. The cross-section SEM image of the beam is shown in Fig. 5.24 (a). The beam thickness measured is around 25 μm. FEM and analytical calculations at 25 μm thickness give resonance frequency for two-beam device as 1535.2 Hz and 1622 Hz and for four-beam device is 2174.7 Hz and 2294 Hz. The experimental and theoretical results are in close agreement with each other. Due to fabrication imperfections, there is drift in the resonance frequency. The resonance frequency especially for the four-beam device is high for energy harvesting applications because

ambient vibrations are of low frequency up to 1 KHz. Therefore the thickness of the beam must be reduced so that the device can have lower resonance frequency.

Fig. 5.24 (b) shows the zeta image of the ZnO pattern after etching. It can be seen that 19.8 µm of lateral etching of ZnO occurs while etching 2 µm thickness of ZnO layer. This results in poor connection of bottom and top electrode. The fabrication process is optimized to reduce the beam thickness and for proper passivation between bottom and top electrode.

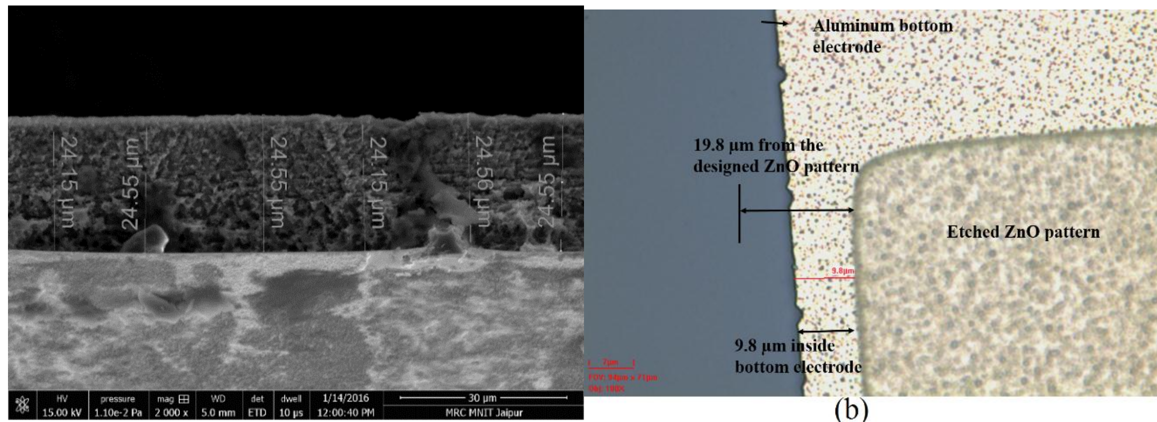

Fig. 5.24 (a) Cross-sectional SEM image of the beam. (b) Zeta image of the ZnO pattern after etching.

5.5 Fabrication process optimization and device fabrication (Batch2)

To further reduce the resonance frequency of the device the thickness of the beams has to be further reduced. As from the fabrication flow the TMAH etching is done at first, therefore, the thickness of the beams cannot be reduced because the handling of the wafer becomes difficult in the subsequent steps. Therefore, to overcome this issue first the front side patterning of bottom electrode, piezoelectric layer and top electrode is done then TMAH etching is done followed by DRIE. To improve the step coverage Plasma enhanced chemical vapor deposition (PECVD) oxide is deposited after bottom electrode patterning and after ZnO patterning.

5.5.1 Fabrication flow

Process sequence optimization for fabrication of guided two-beam and four-beam piezoelectric energy harvester device is shown in Fig. 5.25. Front side processing is done first and followed by TMAH and DRIE.

5.5.2 Fabrication of structure on front side of wafer

On front side of wafer, aluminum (Al) of 350 nm thickness is deposited using e-beam technique. (Mask #1) is performed for patterning of bottom electrode. Positive photoresist S1818 is used and CD26 its corresponding developer for masking the desired pattern followed by wet etching using Al etchant. After Al etching 0.5µmof SiO_2 layer is deposited using PECVD technique which is followed by deposition of 2.5µm thick ZnO layer using RF magnetron sputtering (with following environmental parameters; power400 W, gas composition as 40%Ar + 60%O2, pressure = 30 mtorr and deposition rate 0.5 µm/hr). Thickness of ZnO is kept 2.5 µm because after this thickness piezoelectric properties gets saturated. Photolithography (mask #2) for patterning ZnO film is done using positive photoresist S1818. The etching of ZnO layer is done using dilute HCl solution. A 0.5 µm of PECVD SiO_2 layer is again deposited over patterned ZnO film for passivation. Aluminum of thickness 1 µm is sputtered over SiO_2 layer and using photolithography (mask #3) Al is patterned to form split electrodes.

5.5.3 Bulk-Micromachining of silicon for pyramidal shape seismic mass

TMAH etching is done after front side patterning because etching can be done at greater depth, handling of wafers becomes easier and it results in higher yield. Front side protection of the processed wafer from TMAH solution during bulk-micromachining is done using 3-inch wafer holder zig (by AMMT) as shown in Fig. 5.26. Photolithography for TMAH opening is done by patterning the thermal oxide using positive photoresist S1818 and is dry etched using Reactive ion etching (RIE). After oxide opening as the wafer is subjected to bulk-micromachining of Si in 25%wet TMAH etching at 79ºC giving an etch rate of 20 µm/hr. A pyramidal shape seismic mass having smooth surface and perfect edges due to corner compensation is realized.

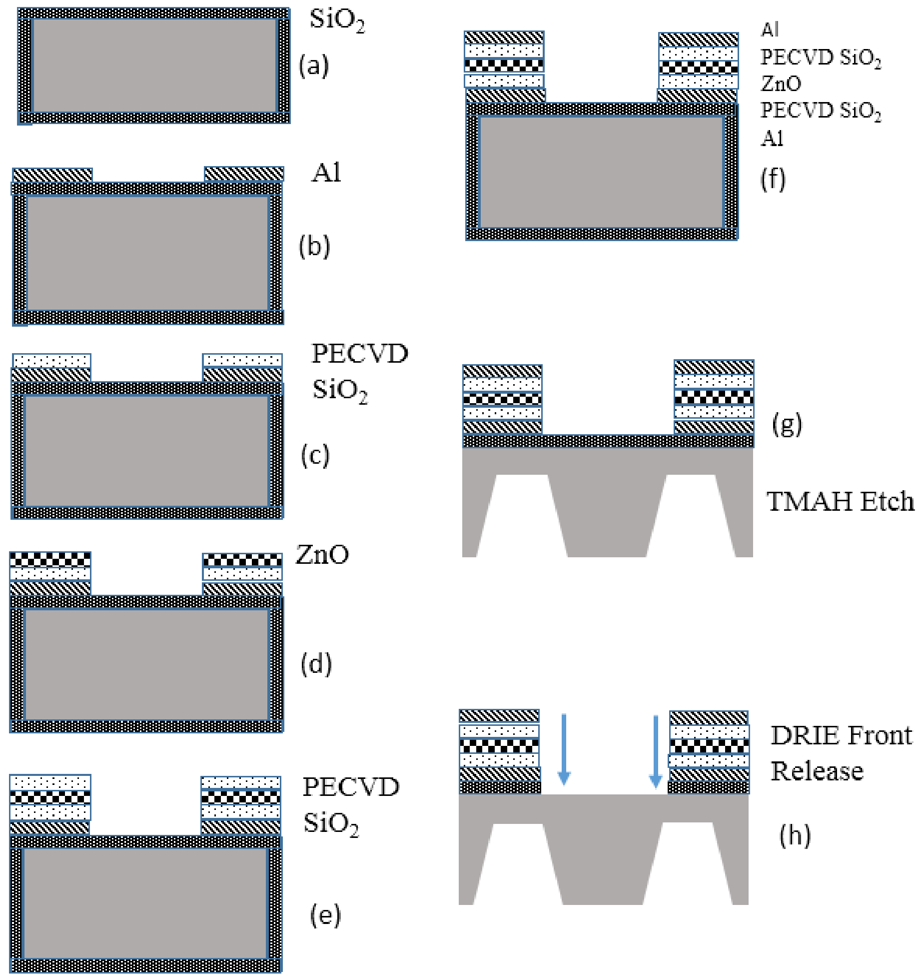

Fig. 5.25 Fabrication steps for device (a) Thermal oxidation (b) Aluminum deposition and patterning (mask #1). (c) PECVD SiO_2 deposition. (d) ZnO deposition and patterning (mask #2). (e) PECVD SiO_2 deposition. (f) Aluminum deposition and patterning (mask #3). (g) Oxide patterning for pyramidal shape seismic mass (mask #4) and TMAH etching. (h) Patterning for guided beams (mask #5), DRIE front release and dicing.

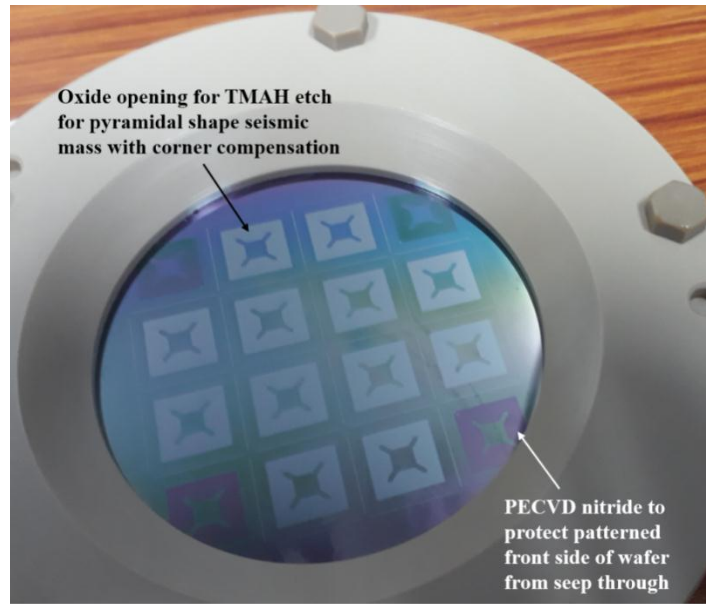

Fig. 5.26 Snapshot of the front side protection of the processed wafer with Zig for TMAH etching.

5.5.4 Guided beam release and thinning using deep reactive ion etching (DRIE)

The photolithography (Mask #5) is done using positive photoresist S1818 and wafer is patterned from front side. DRIE is performed from the front side of the wafer to form the beam structure as shown in Fig. 5.27 (a). After DRIE from the front side beam thinning is performed from the back side to achieve beam thickness of 10 µm or lesser which can be seen from Fig. 5.27 (b). This process of DRIE release of beams from front side of wafer and thinning from back side of wafer was optimized in several different runs as it is the most critical step in defining the beam thickness and therefore the resonance frequency of the energy harvester. The process is done with Alcatel AMS100 DRIE machine. The details of DRIE process parameters are as follows: Pressure= 4.8 x 10^2 mbar, Source RF1 = 1000 Watt, Chuck RF2 = 20 Watt. SF6= 600 sccm. Front side etching of the Silicon is done with the above mentioned parameters for 8 minutes, which etches Si to a depth of 25 µm (front side) giving an etch rate of 3.125 µm/minute. DRIE of Si from back side of the wafer is performed using the same recipe but in two intervals of 2 minutes each.

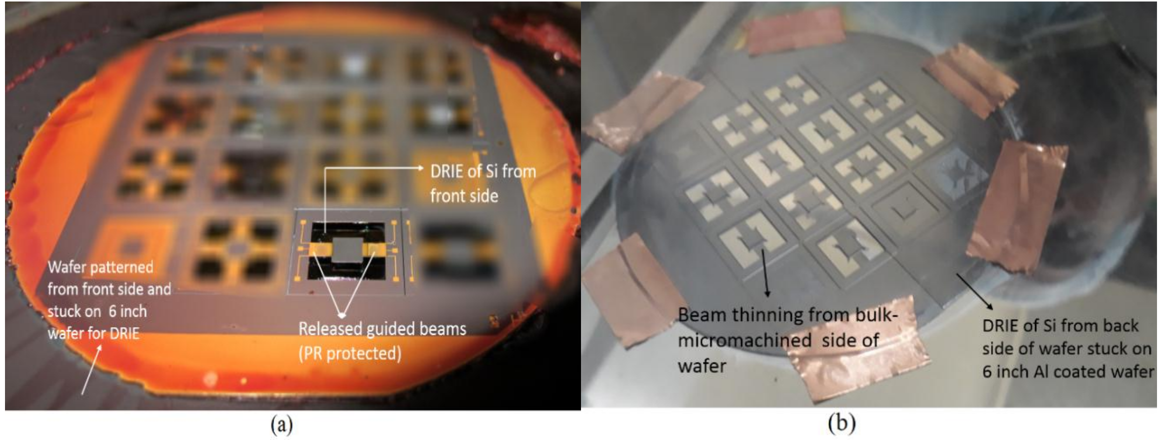

Fig. 5.27 (a) Snapshot of wafer after DRIE etch of Si from front side. (b) Snapshot of bulk-micromachined side of the wafer in process during beam thinning process.

5.5.5 Dicing and device release

The devices are diced manually. Fig. 5.28 (a), (b) gives the snapshot of fabricated guided (a) two-beam and (b) four-beam piezoelectric energy harvester.

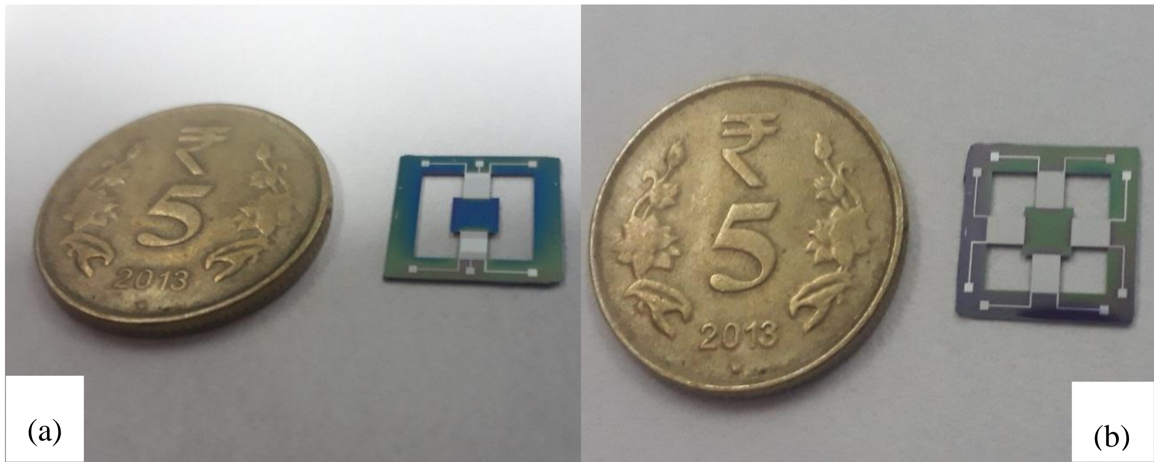

Fig. 5.28Snapshot of fabricated guided (a) two-beam and (b) four-beam piezoelectric energy harvester.

The device fabrication is completed successfully and both two-beam and four-beam devices are successfully diced for testing.

5.6 Design of the PCB and packaging

After self-dicing and separating the chips, they have to be tested in different ways. For resonance frequency determination, an LDV is used. For LDV testing, the bare chip is

used on a piezoelectric exciter. The devices have to be further tested for their outputs in vibration ambiance. For vibration testing, the device is mounted on a vibration table (shaker) and we have to take out the connections from the output pads of the device. Therefore, a special kind of PCB was designed having gold plated pads suitable for wire bonding. PCB designed for both two-beam and four-beam devices are shown in Fig.5.29 (a) and Fig. 5.29 (b) shows the device mounted on PCB package using non conducting epoxy and curing it at 130º C for 30 minutes. The device is mounted on PCB and wire bonded from the chip to the PCB. To connect the device to the analyzer for vibration bench testing connectors are to be connected for proper testing of devices. Therefore, a special kind of PCB attachment was designed with a built-in connector and attached to the PCB so that the coaxial cable can be connected to the analyzer. The device packaged in this way has to be mounted on the vibration table and output of the device can be directly taken from the coaxial output connectors as shown in the Fig.5.30.

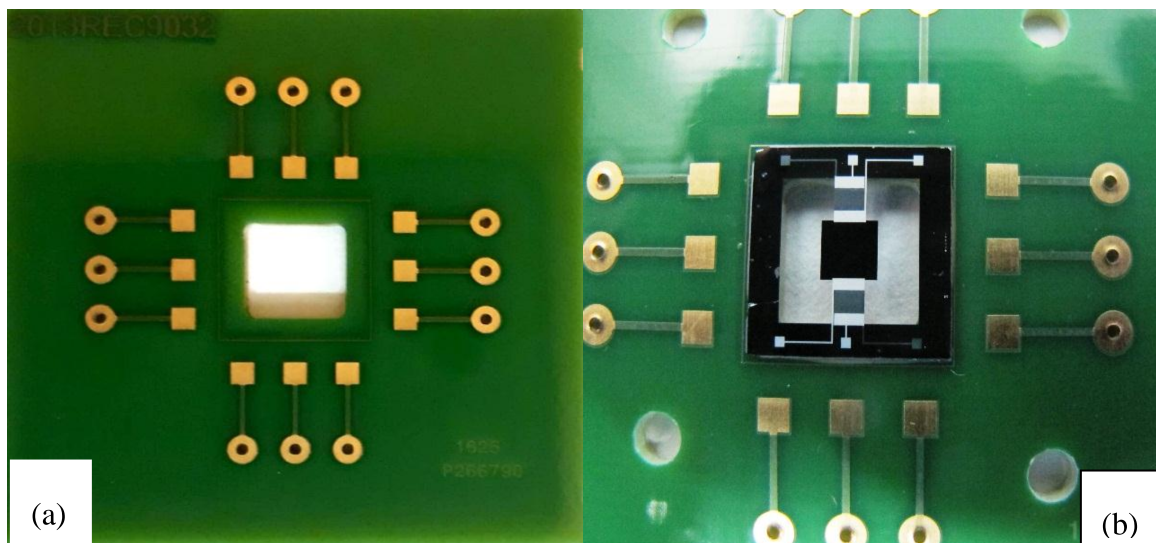

Fig. 5.29 (a) Snapshot of PCB package. (b) Device mounted on a PCB package.

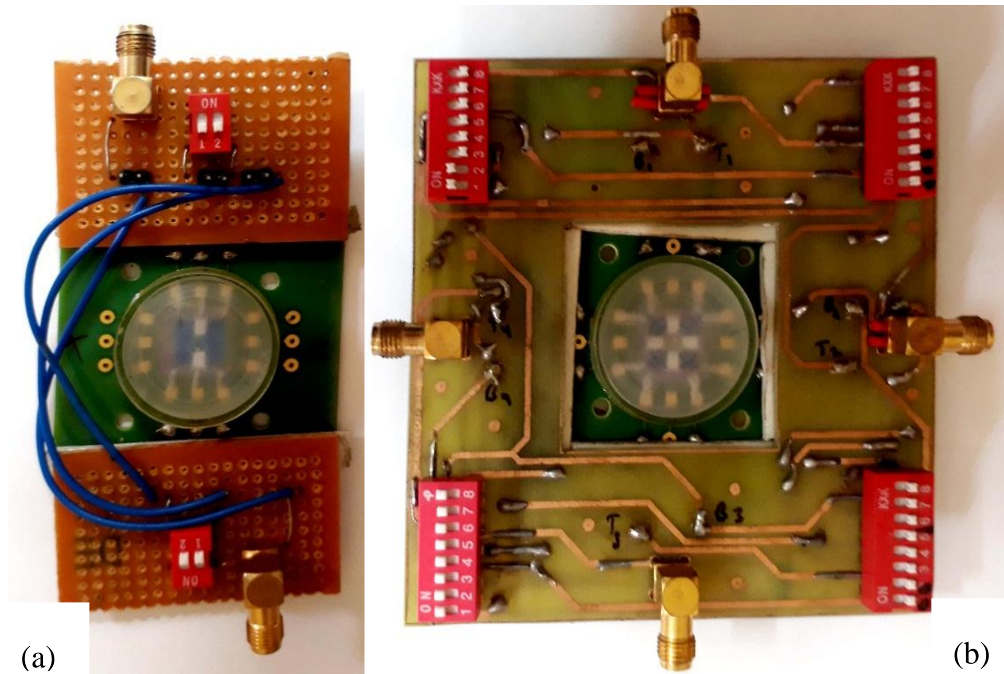

Fig. 5.30 (a), (b) PCB with connectors to connect the devices to the vibration analyzer.

Therefore, the devices are ready to be tested for vibration shaker testing, laser Doppler vibrometer testing and also for structural characterization which is presented in the next chapter6.

The comparison for the guided two-beam and four-beam device for the optimized process is given in Table 5.3.

Table 5.3 Comparison for two-beam and four-beam device.

Parameter	Designed (two-beam/four-beam)	Fabricated (two-beam)	Fabricated (four-beam)
Beam length	2500	2490	2470
Beam width	2000	1959	1978
Seismic mass (top)	3500 x 3500	3552 x 3548	3532 x 3517

Seismic mass (bottom)	3033 x 3033	3081 x 3094	3090 x 3095
Seismic mass (height)	330	336	335.8
Beam (pre-thinning)	20	25.63	25.23
Beam (post-thinning)	10	13	12
Frequency (pre-thinning)	1535/2174 Hz	1971.9 Hz	2540.6 Hz
Frequency (post-thinning)	483/519 Hz	466 Hz	515 Hz

Chapter 6

Testing and Characterization of Guided Beam Piezoelectric Energy Harvester

In this chapter, an elaborate characterization of both kind of fabricated devices two-beam and four-beam devices has been done. Some of the characterization has been carried out during the fabrication process itself, that is, the wafer-level characterization, required to ensure the correct dimensions of different structures such as beams and suspended mass. In order to obtain the optimum output from the device, it is necessary to characterize the device at each level including the fabrication steps. It is quite difficult to obtain the correct dimensions of different structures in wet bulk micromachining, still very close dimensions have been achieved.

The elaborate characterization includes structural, material, morphological, topological, dynamic and electrical characterization of the device. Different tools have been utilized to carry out all these characterizations. Structural characterization is done in which, phase orientation of materials is done using X-ray diffraction (XRD), surface morphology is obtained using Scanning electron microscope (SEM), and topological view is obtained with Atomic force microscopy (AFM). Dynamic characterization is performed using a laser Doppler vibrometer (LDV) to experimentally obtain the resonance frequency of the two-beam and four-beam devices. Finally, vibration bench testing is done for measurement of electric potential and sensitivities of the two-beam and four-beam devices.

6.1 Structural Characterization

Structural characterization for the device has been performed at Material Research Centre at MNIT, Jaipur, India. XRD of the device using Powder XPERT PRO from Panalytical is done to determine the phase orientation of the deposited zinc oxide (ZnO) and gold

(Au) materials. The XRD pattern of the device is shown in Fig. 6.1 (a). There are clearly two dominant peaks seen from Fig. 6.1 (a), the first peak comes at 34.4° which represents the peak of ZnO material deposited and the second peak comes at 38.18° which represents peak of gold (Au) material deposited to form the bottom and top electrodes.

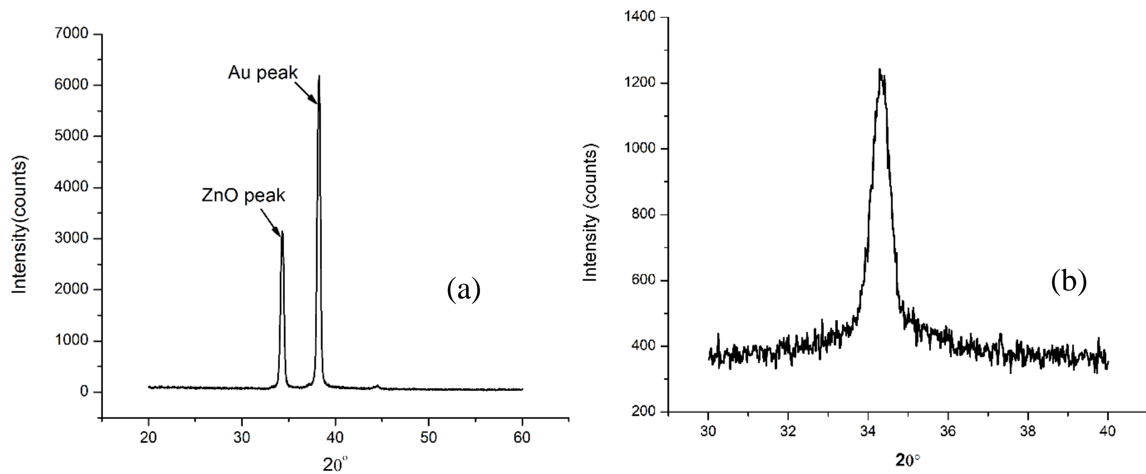

Fig. 6.1 (a) XRD pattern of the device (b) XRD pattern of ZnO deposited on a bare silicon wafer.

Fig. 6.1(b) gives XRD pattern of deposited ZnO thin film on a bare silicon wafer. Thickness of ZnO is kept 2.5 µm because above this thickness piezoelectric properties get saturated [104]. It is observed that the growth of the film is highly oriented along the c-axis normal to the substrate because there only one peak corresponding to (002) reflection of Wurtzite phase of ZnO. At an angle of $2\theta = 34.4°$, the ZnO film exhibits a strong peak, which indicates that the ZnO film grains have good orientation exhibiting good piezoelectric properties.

NOVA NANO FESEM 450 from FEI is used to take SEM images of devices. Fig. 6.2 shows the SEM image done using of the bottom view of pyramidal shape seismic mass. The dimensions of the seismic mass from the bottom are found to be 3084 x 3094 µm as seen from SEM image which is similar to designed dimensions of 3083 x 3083 µm. The corner edges of the seismic mass are smooth due to corner compensation structures designed for TMAH etching.

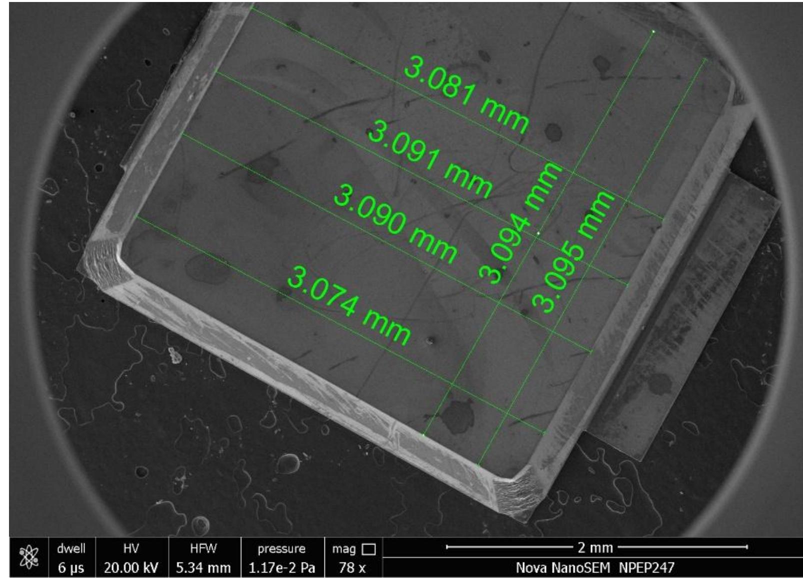

Fig. 6.2 SEM image of the bottom view of the pyramidal shape seismic mass.

Fig. 6.3 shows the SEM image of the top view of pyramidal shape seismic mass. The dimensions of the seismic mass from the top are 3554 x 3353 μm as seen from SEM image which is similar to designed dimensions of 3500 x 3500 μm. The designed dimensions of the proof mass are obtained in device fabrication.

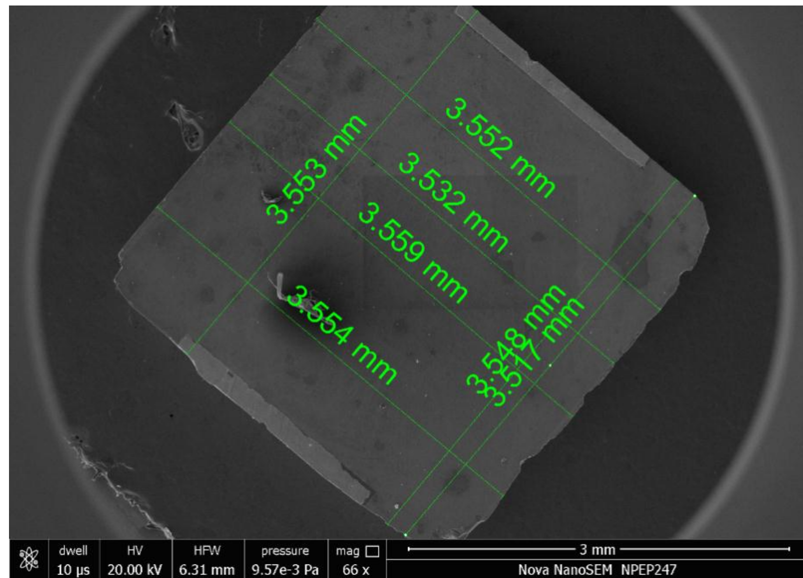

Fig. 6.3 SEM image of the top view of the pyramidal shape seismic mass.

Fig. 6.4 shows the SEM image of the beam with bottom electrode. The dimensions of the fabricated bottom electrodes are 2543 x 1978 µm which are quite close to the designed dimensions of 2500 x 1980 µm.

Fig. 6.4 SEM image of the beam with bottom electrode.

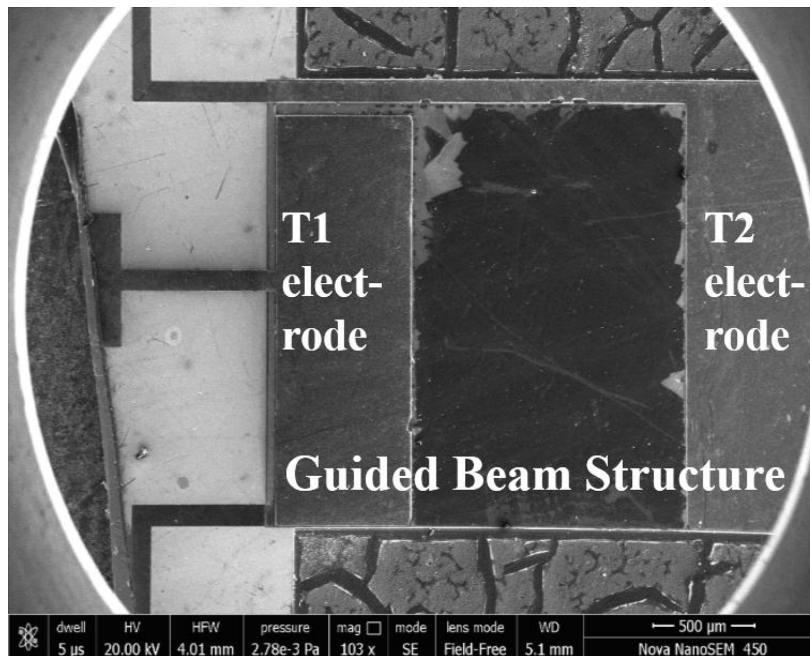

Fig. 6.5 SEM image of the split electrodes each having dimensions of 675 µm.

Fig. 6.5 shows the SEM image of the beam with bottom top split electrodes. The dimensions of the fabricated split electrodes are 675 x 675 µm.

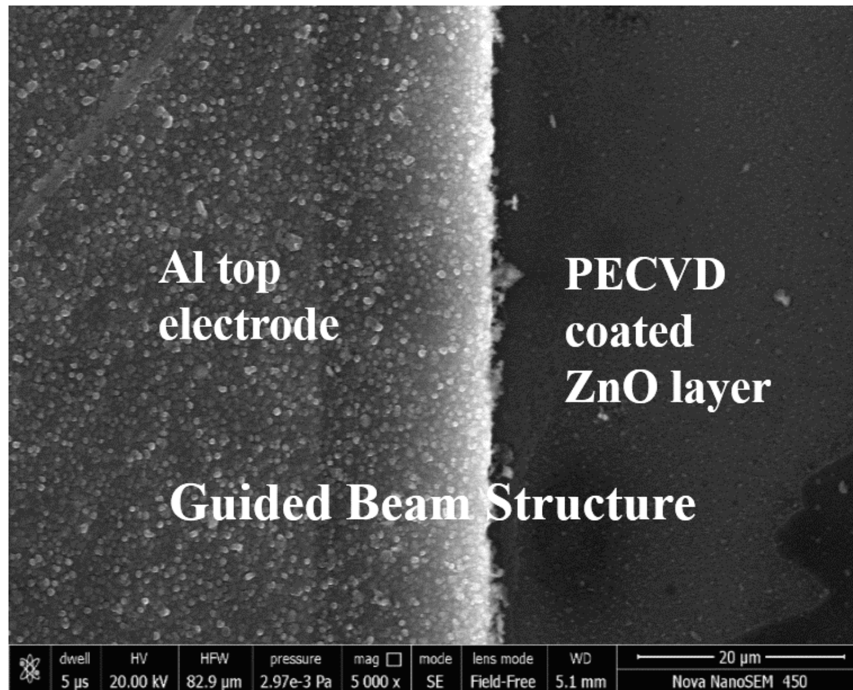

Fig. 6.6 SEM image of the interface of the top electrode and the piezoelectric layer

Fig. 6.6 shows the SEM image of the interface of the split electrode and the piezoelectric layer.

The AFM imaging was carried by the Multimode 8.0 instrument (Bruker, Germany) in the scan asyst mode on the different frame size as 2, 5 and 10 µm. The images infer that a smooth coating with homogeneous texture has been achieved in deposition for gold electrodes as well as ZnO.

Fig.6.7 (a) and (b) gives the AFM images of the gold metal deposited for bottom and top electrodes.

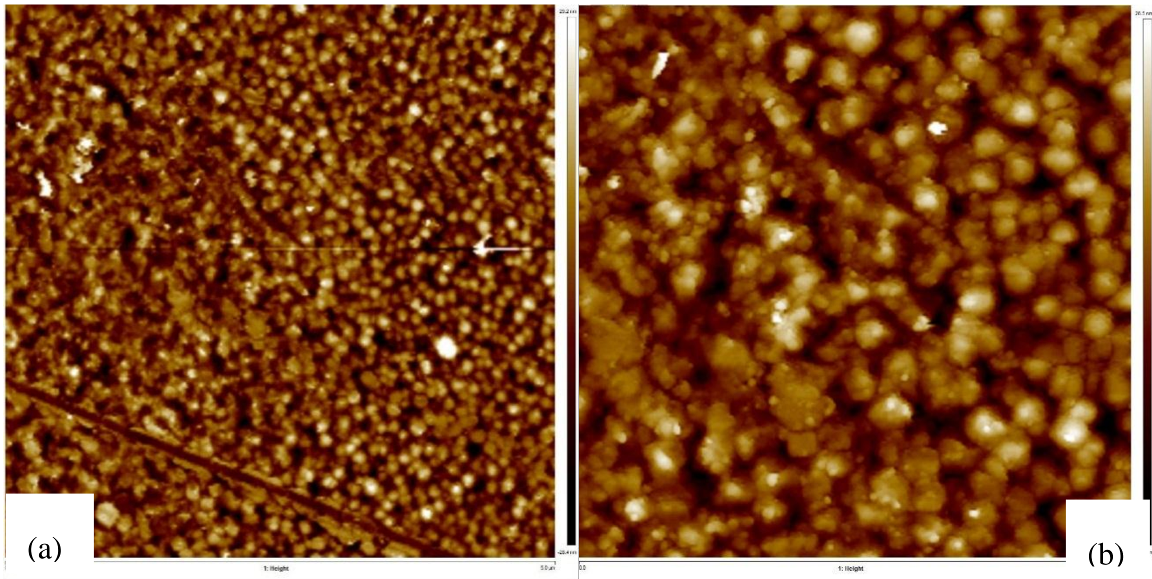

Fig. 6.7 (a) and (b) AFM images of the gold metal deposited for electrodes.

Fig. 6.8 (a) and (b) show the AFM of the deposited 2 μm thick ZnO layer. The ZnO layer deposited is highly oriented as seen from AFM images.

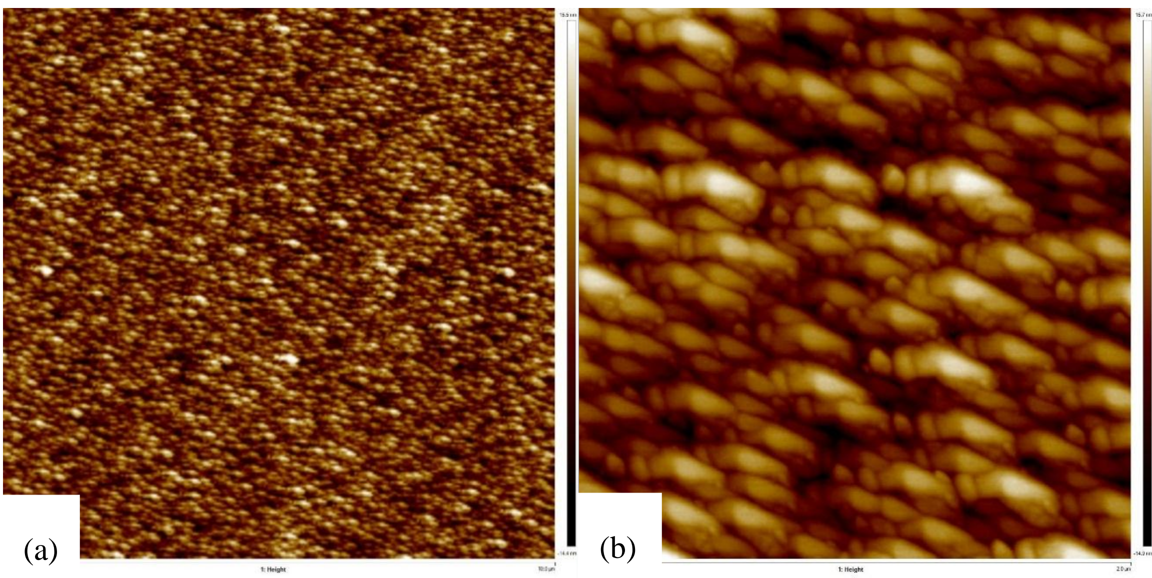

Fig. 6.8 (a) and (b) AFM images of deposited 2 μm thick ZnO layer.

6.2 Dynamic Characterization using Laser Doppler Vibrometer

Dynamic performance of the guided two-beam and four-beam piezoelectric energy harvester is performed using a Laser Doppler Vibrometer (LDV). Resonance frequency

of the energy harvesting device is the key parameter as the device should resonate with the ambient vibration frequency for maximum power generation. Laser Doppler Vibrometer is used to experimentally calculate the resonance frequency, bandwidth and the quality factor of the device. PolytecMSA-500 Micro System Analyzer (LDV), an optical transducer is used for determining the vibration velocity and displacement at a measurement position of the device. The dynamic parameters are calculated by sensing the frequency shift of backscattered light from a moving surface focused on the device. The object scatters or reflects light from the laser beam and the Doppler frequency shift is utilized to measure the component of velocity, which lies along the axis of the laser beam. The signal generator of the MSA-500 generates a broadband excitation signal called as periodic chirp, an AC signal to excite all frequencies in a range simultaneously, and then the Fast Fourier Transform (FFT) technique is used to measure all of these frequencies at the same time. Maximum instrument bandwidth is 1.5 MHz which measures the velocity of vibration structure. The LDV experimental setup (at CSIR-CEERI) is used to perform dynamic characterization for the guided two-beam and four-beam piezoelectric energy harvester is shown in Fig. 6.9. A piezoelectric disc is used to excite the device; a signal is applied to the disc for base excitation to excite all modes in the band for the device as shown in Fig. 6.10. The scan is performed around the center of the proof mass of the device to obtain data points for maximum displacement.

6.2.1 LDV measurement for guided two-beam piezoelectric energy harvester

Frequency sweep from 0 – 6 KHz is applied to obtain the displacement versus frequency response for the guided two-beam device. Fig. 6.11 gives the scan which clearly shows the mechanical resonance of the device in the Z direction. Fig. 6.12 gives the device resonance frequency measured using LDV which comes at 1971.9 Hz and having a bandwidth of 40.6 Hz. The maximum displacement measured at resonance frequency is 49.67 nm.

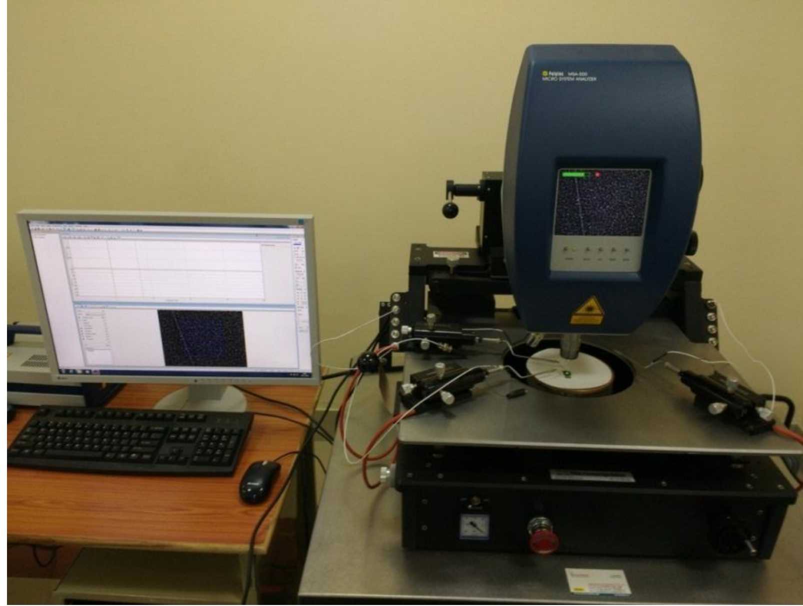

Fig. 6.9 Experimental setup of LDV used to measure dynamic response of the device at CSIR-CEERI.

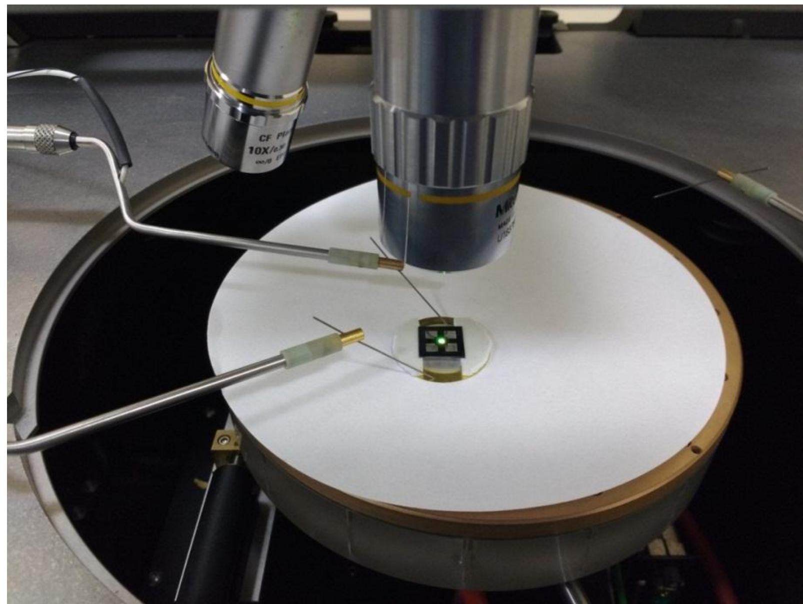

Fig. 6.10 Extended view of the device mounted on the piezo disc for LDV measurement.

Frequency response curve for the air-damped device clearly shows device operation in the dominant frequency mode. Since the device is mechanically excited using a piezoelectric disc, the electrical effects on spurious modes are eliminated. It can be seen

from Fig. 6.12 that secondary mode for the device comes around 4 KHz is suppressed and predominated by first mode. Therefore the guided two-beam device provides a stable and reliable operation by operating in dominant frequency mode and providing maximum displacement in Z-direction which leads to maximum power generation.

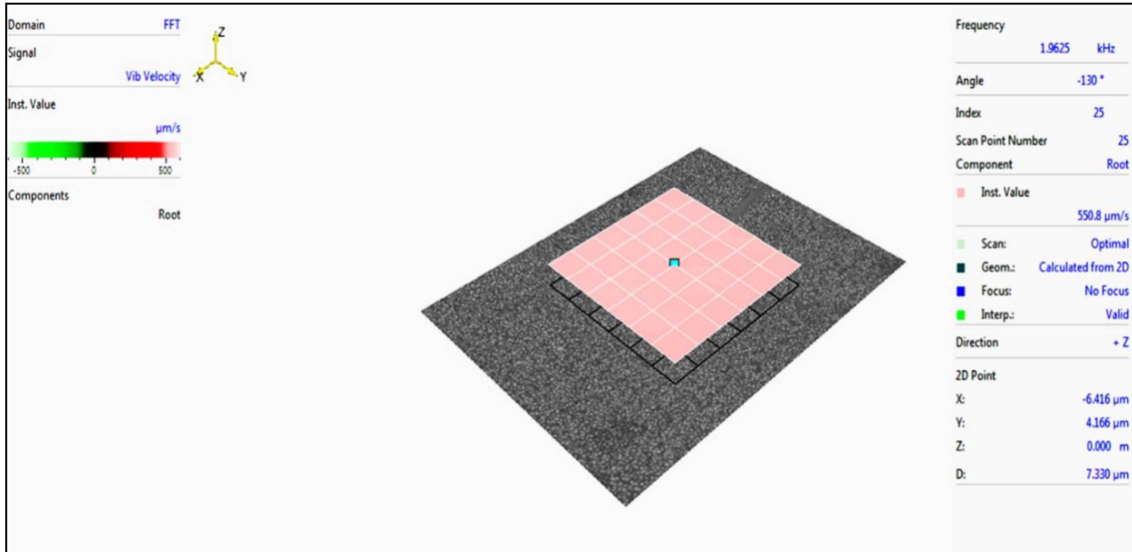

Fig. 6.11 Snapshot of Scanning LDV measurement result for guided two-beam device. The device operates in dominant frequency mode (±Z direction).

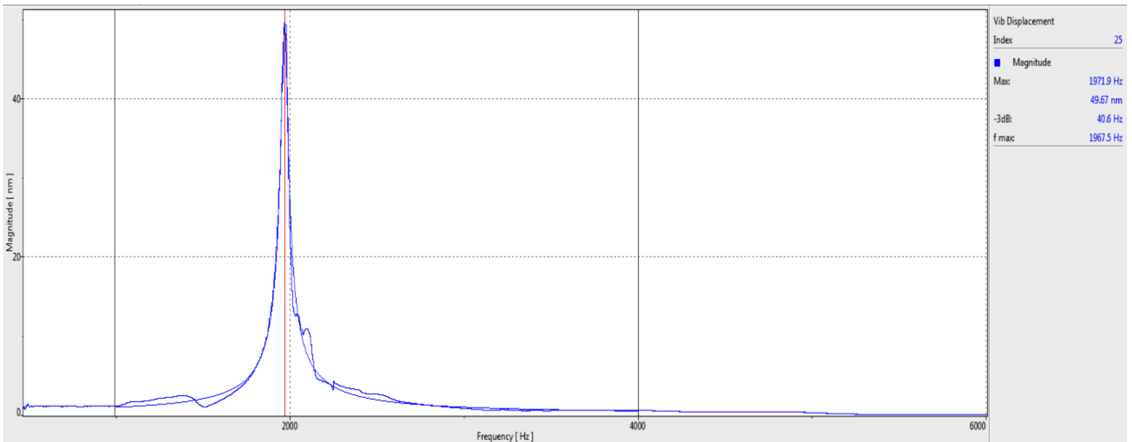

Fig. 6.12 Frequency versus displacement curve for the two-beam device obtained using LDV. The resonance frequency for the device obtained experimentally comes at 1971.9 Hz giving a maximum displacement of 49.67 nm.

Wideband frequency operation is another important parameter so that the energy harvester can resonate with a range of vibration frequencies for maximum power generation. This guided two-beam piezoelectric energy harvester gives a 3dB bandwidth of 40.6 Hz. Maximum displacement measured at resonance frequency is 49.67 nm which will generate stress on the two-beams resulting in potential generation.

Guided two-beam device gives a resonance frequency of 1622 Hz when calculated analytically using equation (4.1), whereas resonance frequency obtained using FEM comes at 1535.2 Hz. Resonance frequency experimentally calculated using LDV comes at 1971.9 Hz, therefore, the analytical calculation, simulation and experimental results are in close agreement to each other.

6.2.2 LDV measurement for guided four-beam piezoelectric energy harvester

Frequency sweep from 0 – 8 KHz is applied to obtain the displacement versus frequency response for the device. The frequency response for the energy harvester device is shown in Fig. 6.13 and Fig. 6.14, the device resonance frequency measured with LDV is at 2540.6 Hz and with a bandwidth of 101.9 Hz. The maximum displacement measured at resonance frequency is 32.17 nm.

Frequency response curve for the air-damped device clearly shows device operation in the dominant frequency mode. It can be seen from Fig.6.14 that second mode for the device comes around 5 KHz is suppressed and predominated by the first mode. Therefore the guided four-beam device provides a stable and reliable operation by operating in dominant frequency mode and providing maximum displacement in Z-direction which leads to maximum power generation.

Wideband frequency operation is another important parameter so that the energy harvester can resonate with a range of vibration frequencies for maximum power generation. This guided four-beam device gives a 3dB bandwidth of 101.9 Hz. Maximum displacement measured at resonance frequency is 32.17 nm which will generate stress on the four-beams resulting in a potential generation.

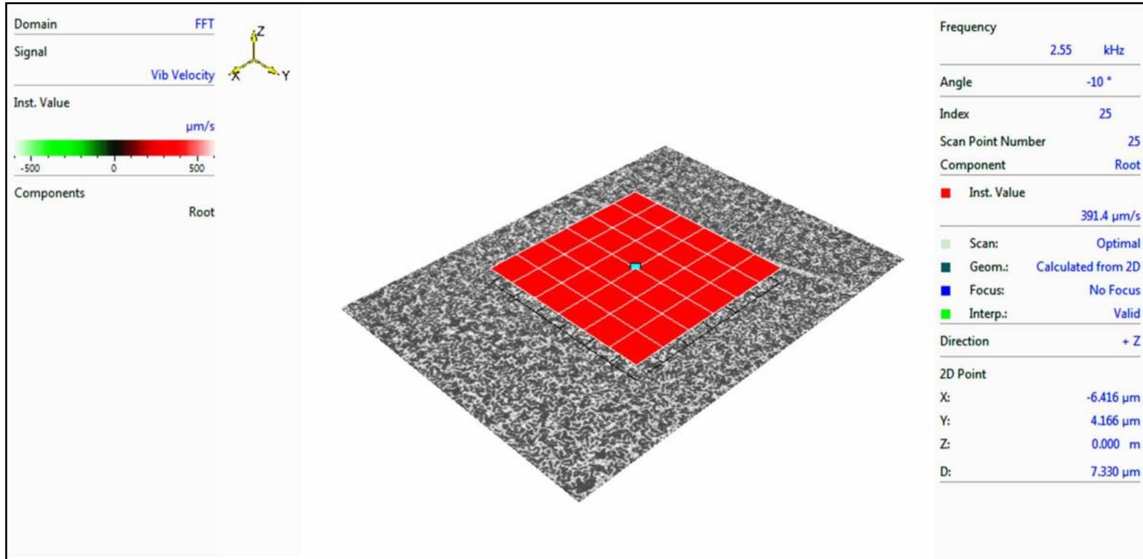

Fig. 6.13 Snapshot of Scanning LDV measurement result for guided four-beam device. The device operates in dominant frequency mode (±Z direction).

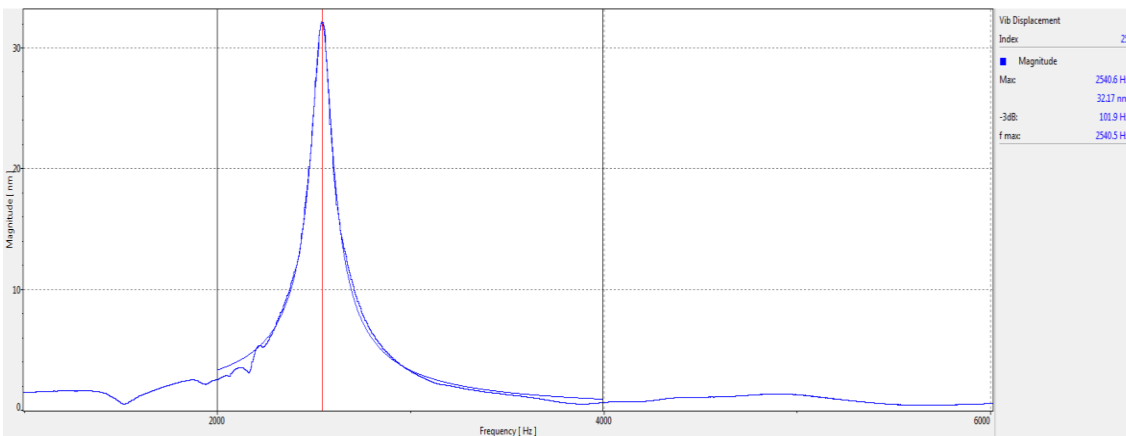

Fig. 6.14 Frequency versus displacement curve for the four-beam device obtained using LDV. The resonance frequency for the device obtained experimentally comes at 2540.6 Hz giving a maximum displacement of 32.17 nm.

Guided four-beam device gives a resonance frequency of 2294 Hz when calculated analytically using equation (4.1), whereas resonance frequency obtained using FEM comes at 2174.7 Hz. Resonance frequency experimentally calculated using LDV comes at 2540.6 Hz, therefore, the analytical calculation, simulation and experimental results are in close agreement to each other. There is a slight deviation of the value of the resonance frequency calculated using FEM and using LDV because fabrication precision could not

be achieved due to dependency of wet etching on several factors which results in non-uniform beam thickness.

6.3 Dynamic Characterization for Batch 2 devices using LDV

As discussed earlier the resonance frequency of the two-beam and four-beam devices is relatively higher in comparison to the freely available frequencies in ambient vibrations in the environment. The fabrication process was optimized as discussed in section 5.5 and devices are fabricated again (batch 2). The fabricated devices are dynamically tested using LDV.

6.3.1 LDV measurement for guided two-beam device

Frequency sweep from 0-2 KHz is applied to obtain the displacement versus frequency response for the device. The frequency response for the two-beam device is shown in Fig. 6.15. The device resonance frequency measured using LDV comes at 466.3 Hz. Frequency response curve for the air damped device clearly shows device operation in the dominant frequency mode giving displacement in Z-direction. The beam thinning process optimized using DRIE enabled to achieve the lowest resonance frequency so far reported for the guided two-beam device as shown in Table 6.2. In this case, the device is going to be quite useful to harvest the ambient energy vibrations from mechanical systems such as motors, rotors, engines, turbines etc. of lower frequency range from few hertz up to 500 Hz.

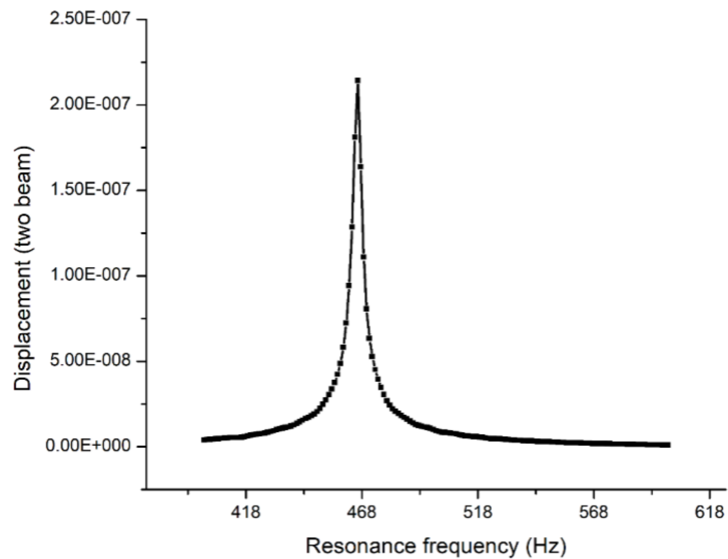

Fig. 6.15 Frequency versus displacement curve for the two-beam device. The resonance frequency for the device obtained experimentally is 466.3 Hz.

6.3.2 LDV measurement for guided four-beam device

Frequency sweep from 0-2 KHz is applied to obtain the displacement versus frequency response for the device. The frequency response for the four-beam device is shown in Fig. 6.16. The device resonance frequency measured using LDV comes at 515 Hz. Frequency response curve for the air-damped device clearly shows device operation in the dominant frequency mode giving displacement in Z-direction. The beam thinning process enabled the resonance frequency of four-beam device to reduce from 2540 Hz to 515 Hz which is very suitable for low frequency ambient vibrations. The overall low-frequency response of the device is improved. Beam thinning process enabled to closely match the resonance frequency of the two-beam and the four-beam device. The resonance frequency of the two-beam device is 466 Hz whereas for four-beam device is 515 Hz, which will almost give similar low-frequency response. Therefore, the four-beam device and two device have almost same frequency response.

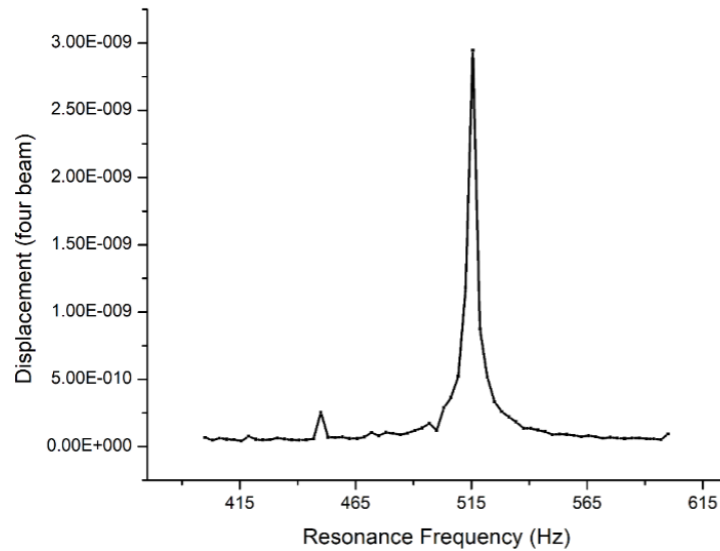

Fig. 6.16 Frequency versus displacement curve for the four-beam device. The resonance frequency for the device obtained experimentally is 515 Hz.

6.4 Static capacitance measurement and device packaging

Static capacitance of the device is measured before vibration testing to ensure proper device operation. The static capacitance of the energy harvester device is measured using low-level CV measurement (Keithley, SUSS Microteck) shown in Fig. 6.17, the static capacitance between bottom electrode and electrode T1 (fixed end) which is 153 pF whereas static capacitance measured between the bottom electrode and electrode T2 (guided end) is measured as 135 pF. Fig. 6.18 (a) shows the device mounted on a PCB package with non-conducting epoxy and Fig. 6.18 (b) shows the packaged and sealed device for vibration shaker testing.

Fig. 6.17 Low level CV measurement of device at CSIR-CEERI.

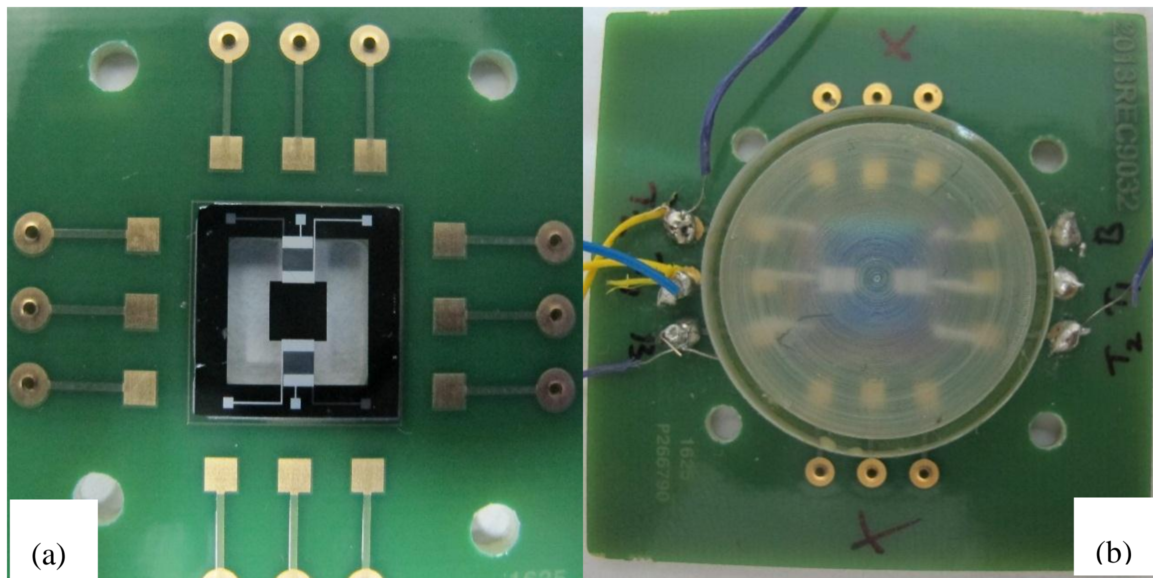

Fig. 6.18 (a) Device mounted on PCB package. (b) Device package sealed for testing.

6.5 Vibration Shaker Test

Vibration shaker test is performed to measure the output potential generated at a given acceleration on two-beam and four-beam device. The output potential generated from the individual electrodes T1 (fixed end) and T2 (guided end) as shown in Fig. 6.19 is experimentally measured using a vibration exciter.

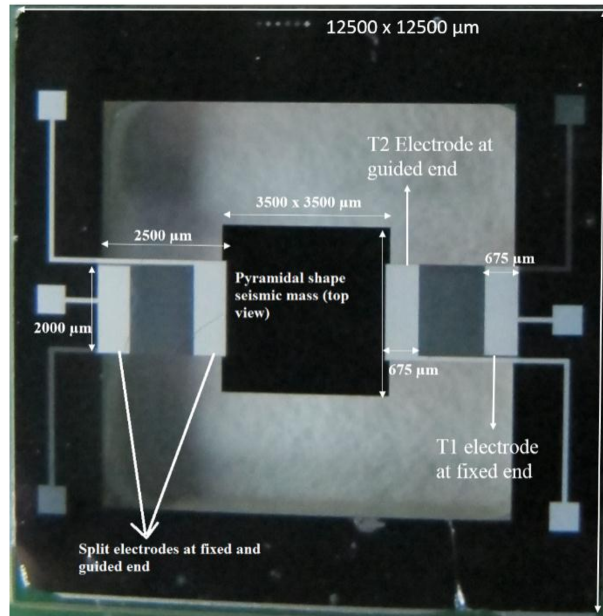

Fig. 6.19 Snapshot of fabricated guided two-beam energy harvester device.

The SPEKTRA SE-10 vibration exciter set-up at Acoustics and Vibration standards laboratory, National Physical Laboratory, Delhi, India is shown in Fig. 6.20. The device is mounted on the shaker and the data is fed to the analyzer.

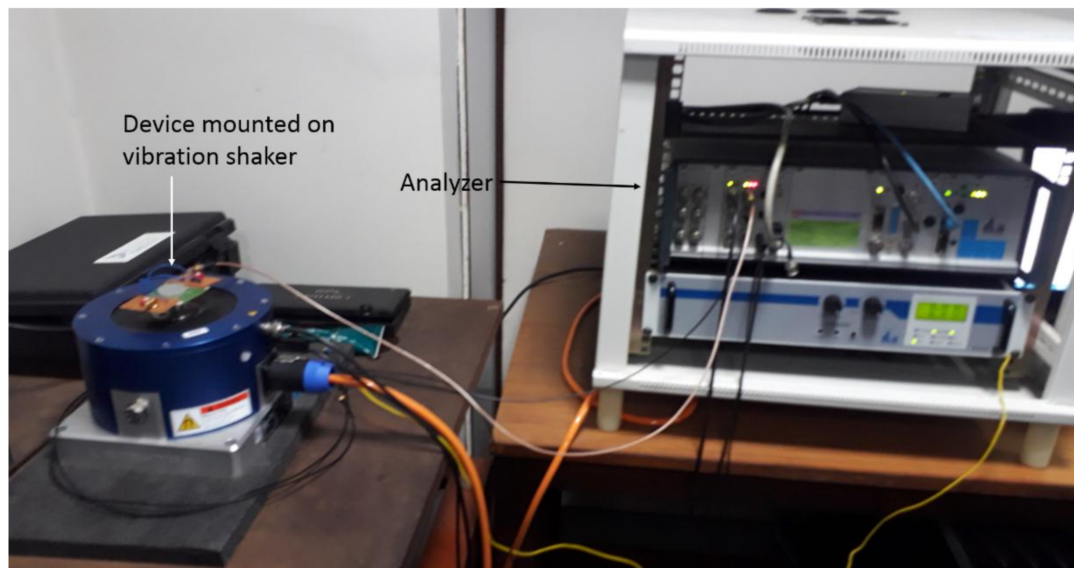

Fig. 6.20 (a) Device mounted on SPEKTRA SE-10 vibration exciter setup at Acoustics and Vibration standards laboratory, National Physical Laboratory, Delhi, India

The SE-10 vibration shaker has an inbuilt calibrated accelerometer having known sensitivity S1. At a given excitation the accelerometer will generate a voltage V1. The device under test (DUT) mounted as shown in Fig. 6.21 will also generate voltage V2. From equation 6.1 the S2 of the DUT is obtained. The main advantage of this measurement is that the device sensitivity becomes independent of the applied input vibration.

$$\frac{S1}{S2} = \frac{V1}{V2} \tag{6.1}$$

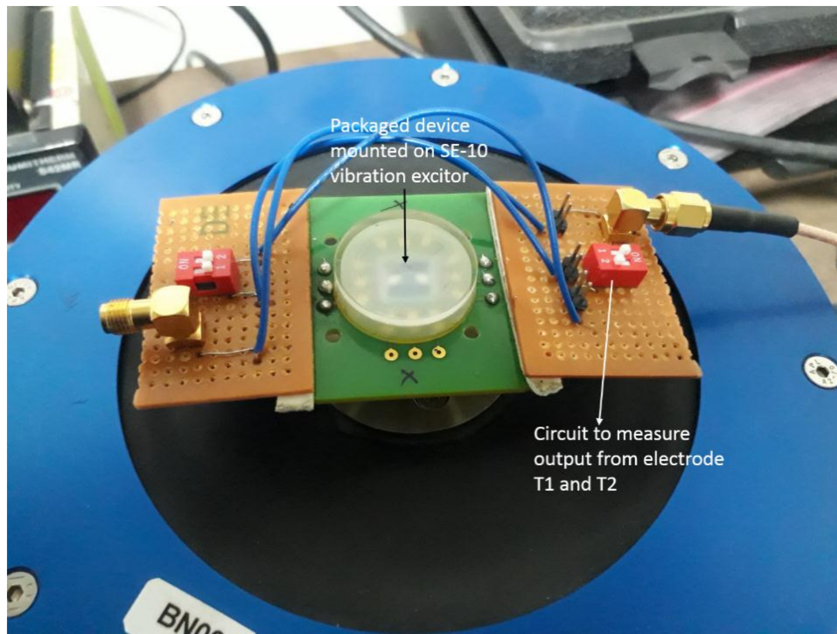

Fig. 6.21 Extended view of the device mounted on SE-10 vibration exciter.

The sensitivity S2 of the device is measured for a frequency range of 160 to 1000 Hz as shown in Fig. 6.20. The sensitivity of the device measured from electrode T1 (at fixed end) at 160 Hz is 0.62762 mV/m/s^2 and at 500 Hz is 0.67484 mV/m/s^2. The sensitivity of the device measured through electrode T2 (at guided end) at 160 Hz is 0.83231 mV/m/s^2 and at 500 Hz is 1.5089 mV/m/s^2 which can be seen from Fig. 6.22. It can be seen that both the electrodes gives higher sensitivity near the resonance of the device which is 466.3 Hz. The sensitivity of the device measured at 800 Hz at T1 electrode is 0.47354 mV/m/s^2 and at T2 electrode is 0.73915 mV/m/s^2. The sensitivity of the device measured

at 1000 Hz at T1 electrode is 0.23781 mV/m/s^2 and at T2 electrode is 0.58963 mV/m/s^2. It can be observed from Fig. 6.22 that after resonance frequency (466 Hz) the sensitivity of the device at both the electrodes reduces. Also, the sensitivity of device measured from electrode T2 at guided end is higher than the sensitivity of the device at electrode T1 at the fixed end because the total displacement at the guided end is higher than the fixed end.

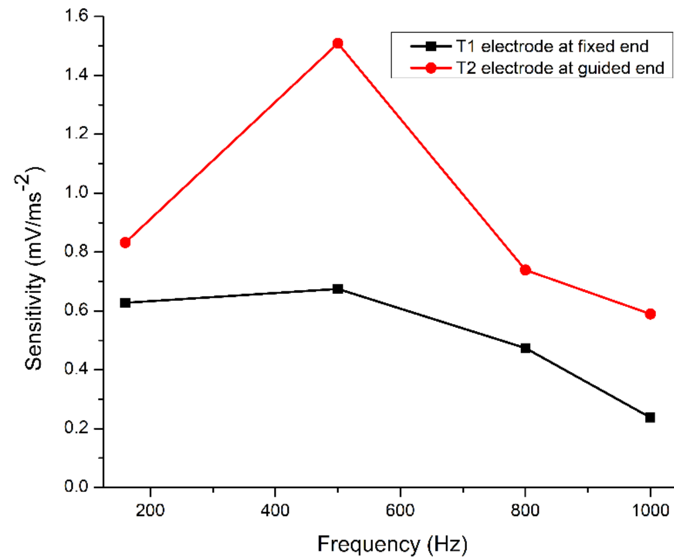

Fig. 6.22 Sensitivity of the device measured from SE-10 at T1 and T2 electrodes.

Guided four-beam device is tested using SPEKTRA SE-10 vibration exciter setup. Fig. 6.23 shows the mounted guided four-beam device on the SE-10 vibration exciter. The sensitivity S2 of the four-beam device is measured for a frequency range of 300 to 1000 Hz. Fig. 6.24 gives the comparison of sensitivity of guided two-beam and four-beam device for the frequency range of 300 to 1000 Hz. At 300 Hz the two-beam device gives a sensitivity of 2.4066 mV/g whereas the four-beam device gives sensitivity of 1.3925 mV/g. At 500 Hz near the resonance frequency of both devices the sensitivity for two-beam device is 1.1392 mV/g and for four-beam device is 1.0231 mV/g. At 800 Hz the sensitivity of two-beam device and four-beam device is 0.73915 mV/g and 0.67223 mV/g respectively. At 1000 Hz the sensitivity of two-beam device and four-beam device is 0.58963 mV/g and 0.56588 mV/g respectively.

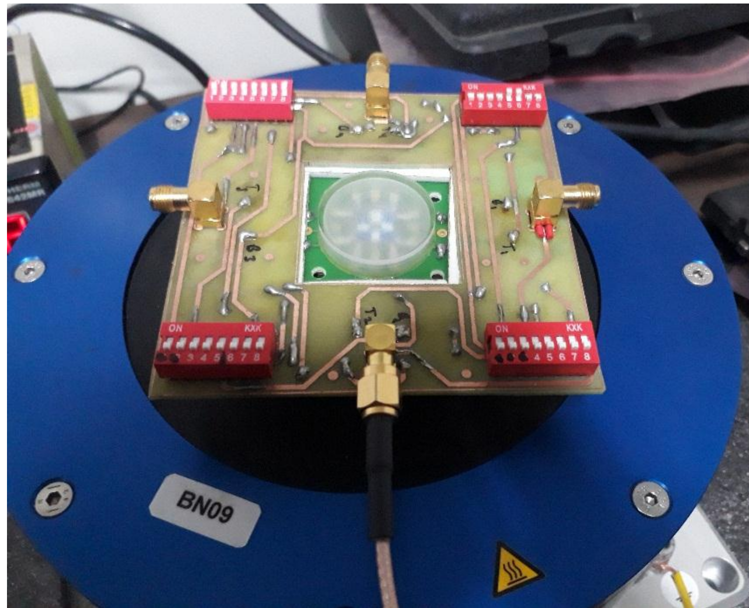

Fig. 6.23 Guided four-beam device mounted on SE-10 vibration exciter.

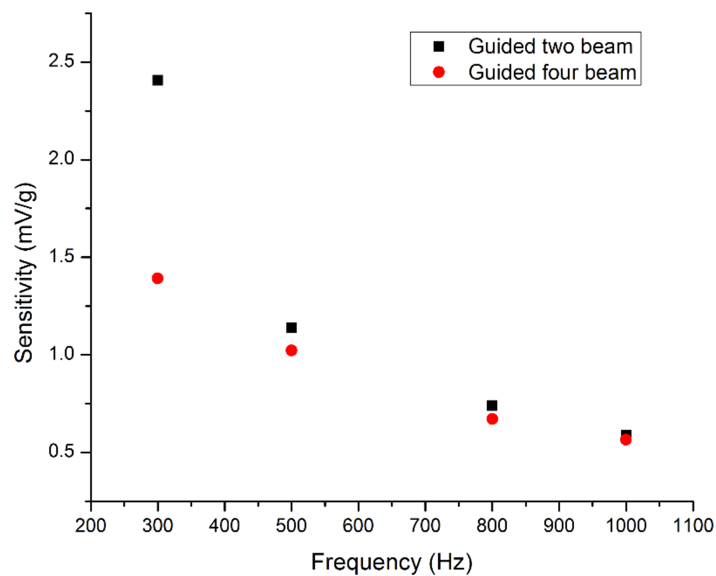

Fig. 6.24 Comparison of sensitivity of guided two-beam and four-beam device.

From Table 6.1, near resonance frequency at 500 Hz two-beam and four-beam device have sensitivity 1.1392 mV/g and 1.0231 mV/g. The output is measured for one beam in both two-beam and four-beam device.

Table 6.1 Comparison of sensitivity of guided two-beam and four-beam device

Shaker Frequency	Two-beam device	Four-beam device
300 Hz	2.4066 mV/g	1.3925 mV/g
500 Hz (near Resonance)	**1.1392 mV/g**	**1.0231 mV/g**
800 Hz	0.73915 mV/g	0.67223 mV/g
1000 Hz	0.58963 mV/g	0.56588 mV/g

Therefore, the total potential generated for two-beam device is 2.2784 mV/g (2x1.1392) whereas the total potential generated by four-beam device is 4.0924 mV/g (4x1.0231) which is 1.814 mV higher than the two-beam device. The beam thinning process done using DRIE to reduce the beam thickness of the two-beam and four-beam device resulted in low-frequency operation. As the resonance frequency of the four-beam device (515 Hz) and the two-beam device (466 Hz) are quite close to each other this gives similar low frequency response for both devices as shown in Fig. 6.24.

6.5.1 Output Voltage/Power versus input acceleration

The device is tested using 9100D Portable Shaker Table at Structural Solutions Private Limited, Hyderabad, India to obtain the output voltage/power as a function of input acceleration. Fig. 6.25 shows the device mounted on the 9100D portable shaker.

Fig. 6.25 Device mounted on 9100D Portable Shaker.

The amplitude knob seen in Fig. 6.25 is used to vary the acceleration from 0.5 g to 5g and voltage/power is obtained experimentally at a constant frequency. Fig. 6.26 gives the graph of voltage versus input acceleration from 0.5 g to 5g. Voltage at 0.5 g is 0.67 mV and at 5 g is 6.7 mV. Power calculated at resistance of 284 Kohm is also shown in Fig. 6.26.

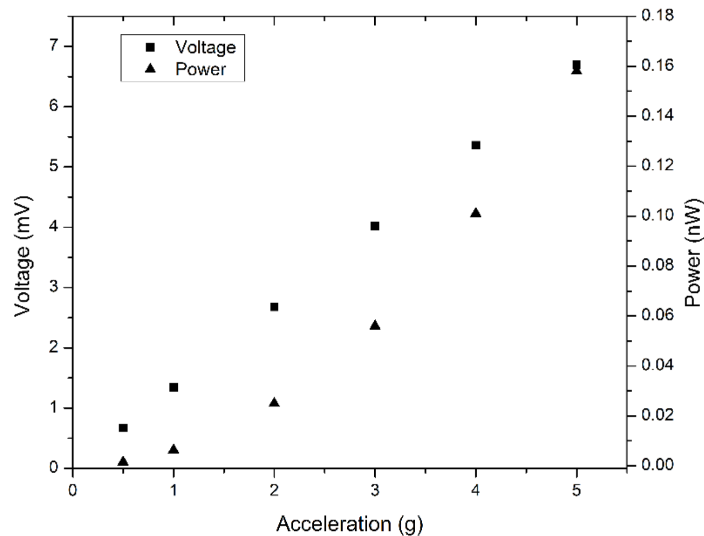

Fig. 6.26 Voltage/power vs acceleration amplitude from 0.5 g to 5 g.

6.5.1 Output Voltage versus frequency

Output voltage from the frequency range of 10 Hz to 800 Hz is obtained experimentally using 9100D Portable Shaker. The frequency from 9100D shaker is varied from 10 Hz to 800 Hz at input acceleration of 0.5 g as shown in Fig. 6.27. Similarly, the frequency variation is done for acceleration of 1g, 2g and 3g and output potential is obtained. Fig. 6.28 shows the graph between the output voltage and frequency at different acceleration ranging from 0.5 g to 3g. The device output increases near 500 Hz i.e. near the resonance frequency of the device. The device exhibits a large operation frequency range from 10 Hz to 800 Hz which can be seen from Fig. 6.28.

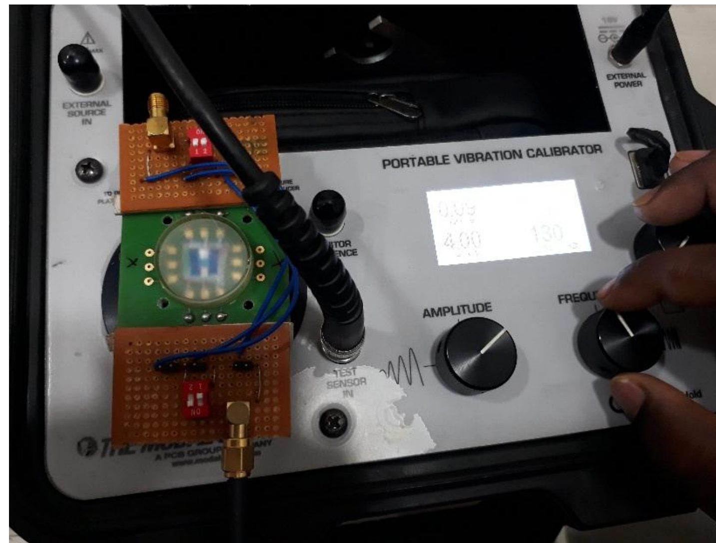

Fig. 6.27 Output voltage vs frequency test using 9100D portable shaker.

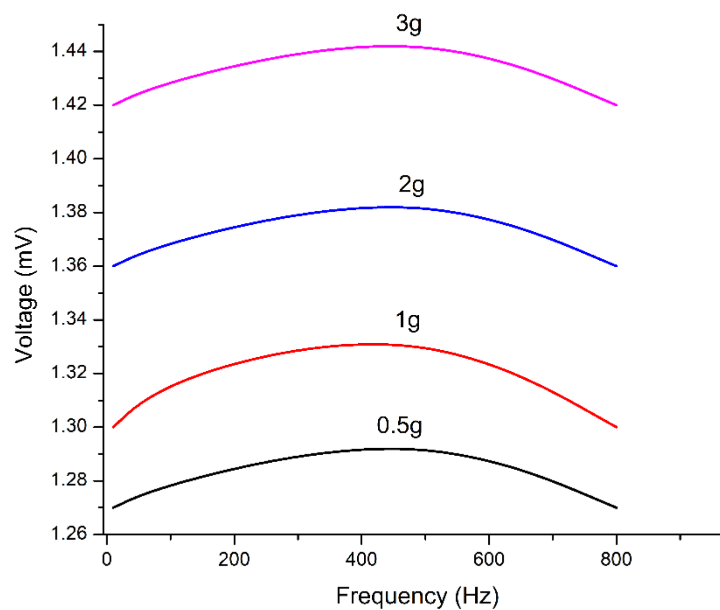

Fig. 6.28 Output voltage and frequency at acceleration ranging from 0.5 to 3g.

From the above characterization results, it is concluded that both two-beam and four-beam devices generate a good amount of power or voltage which can be utilized to in a good way through the design and fabrication of an array of devices integrated in parallel and series configurations to enhance voltage as well as total power to drive an MSN or WSN.

Table 6.2 gives comparison of the current work with the published work. Two-beam device gives lowest resonance frequency reported till date and good sensitivity around 500 Hz. The four-beam device is firstly reported in the current work and gives better results than two-beam device.

Table 6.2 Comparison with published work.

S.No:	Marzencki et al. [53]	Wang et al. [60]	Fabricated device	Remarks
Resonance frequency	1800 Hz	694 Hz	466/515 Hz	Lower frequency range is better
Output voltage	48.97 mV at 1800 Hz	Not reported	44.64/80.2 mV at 500 Hz	Voltage output is double of the net output, as each beam consists of two pair of electrodes, split electrodes on every beam (configured in series)
Voltage Sensitivity	18.53 $mV/m/s^2$	Not reported	2.2784/4.09272 $mV/m/s^2$	Different voltage sensitivity due to different dimensions of seismic mass

Chapter 7

Conclusion and Future Scope

In present research work, the design, modeling, fabrication and characterization of a MEMS-based guided beam type piezoelectric energy harvester has been carried out and presented. The focus of this work was to design and develop a MEMS-based piezoelectric energy harvester for low-frequency ambient vibrations. Two types of devices developed through this work give a stable response at low-frequency vibrations suitable for low power applications. This piezoelectric energy harvester forms part of the power sub-system of the wireless sensor node. The contributions made towards this goal are presented in the following section, followed by future research scope of this work.

7.1 Contributions

Contributions from research work towards realizing a piezoelectric energy harvester can be divided into following points:

(1) Effect of shape of seismic mass is investigated, it is found that pyramidal shape seismic mass gives better results than the conventional square shape seismic mass. Therefore this pyramidal shape of seismic mass is selected for device fabrication and is realized using tetramethyl ammonium hydroxide CMOS compatible 25wt% wet etching. Sharp convex corners of the seismic mass have been precisely realized through the design and implementation of the corner compensation structures.

(2) Position and length of the electrodes were optimized for the guided beam piezoelectric energy harvester. It was investigated that the proposed split electrode pattern reduces the resonance frequency of the energy harvester by 4.2 % as compared to the previously used pattern. Further, the effect of length of electrode on change in capacitance is investigated and it is found that the proposed split electrode pattern results in higher charge generation by 19.26 %.

Moreover, the split electrodes can be integrated in series to enhance the generated potential.

(3) Guided two-beam and four-beam devices were fabricated using MEMS technology through a combination of wet and dry bulk micromachining. The Wet Bulk-micromachining process was done by TMAH etching to realize pyramidal shape seismic mass followed by release of the beam and mass structures as well as the beam thinning using deep reactive ion etching (DRIE). The timing of the DRIE process was optimized to critically control the thickness of the beams which results in low resonance frequency compatible to ambient vibrations.

(4) The resonance frequency for two-beam and four-beam device is experimentally obtained at 466 Hz and 515 Hz which is lowest so far reported. This improves the low-frequency response of the device to make it useful for the energy harvesting of ambient vibrations.

(5) The sensitivity for two-beam device is 1.1392 $mV/m/s^2$ and for four-beam device is 1.0231 $mV/m/s^2$ at 500 Hz near resonance frequency which is highly suitable for low- frequency vibrations.

7.2 Future Scope

The devices realized through this research work are the first version of devices and hence there is a lot of scope based on this study. The prime factor of the device is the output power which can be improved with further research at the level of material, structural and technological levels. Additionally, device reliability, compactness, lifetime and deployability are other issues, which need to be studied. Device packaging is also an important aspect. Vacuum packaging of the device is going to excel the device performance tremendously. The overall size of the packaged device is also an important aspect so that it could be incorporated with the wireless networks efficiently. The current research work may be further utilized to develop a wideband vibration energy harvester to utilize a broader band of the abundantly available ambient vibration energy.

REFERENCES

[1] Agrawal, D.P., 2017. Applications of Sensor Networks. In *Embedded Sensor Systems* (pp. 35-63). Springer, Singapore.

[2] Bhatti, N.A., Alizai, M.H., Syed, A.A. and Mottola, L., 2016. Energy harvesting and wireless transfer in sensor network applications: Concepts and experiences. *ACM Transactions on Sensor Networks (TOSN)*, *12*(3), p.24.

[3] Knight, C., Davidson, J. and Behrens, S., 2008. Energy options for wireless sensor nodes. *Sensors*, *8*(12), pp.8037-8066.

[4] Liu, Y., 2012. Wireless sensor network applications in smart grid: recent trends and challenges. *International Journal of Distributed Sensor Networks*, *8*(9), p.492819.

[5] Ardila, G., Hinchet, R., Montes, L. and Mouis, M., 2013. Mechanical energy harvesting with piezoelectric nanostructures: great expectations for autonomous systems. *Future Trends in Microelectronics: Frontiers and Innovations*, pp.230-243.

[6] de Queiroz, A.C.M., 2013, February. Electrostatic generators for vibrational energy harvesting. In *2013 IEEE 4th Latin American Symposium on Circuits and Systems (LASCAS)* (pp. 1-4). IEEE.

[7] Chye, W.C., Dahari, Z., Sidek, O. and Miskam, M.A., 2010, October. Electromagnetic micro power generator—A comprehensive survey. In *2010 IEEE Symposium on Industrial Electronics and Applications (ISIEA)* (pp. 376-382). IEEE.

[8] Sazonov, E., Li, H., Curry, D. and Pillay, P., 2009. Self-powered sensors for monitoring of highway bridges. *IEEE Sensors Journal*, *9*(11), pp.1422-1429.

[9] Vijayaraghavan, K. and Rajamani, R., 2010. Novel batteryless wireless sensor for traffic-flow measurement. *IEEE Transactions on Vehicular Technology*, *59*(7), pp.3249-3260.

[10] Tolentino, I.M. and Talampas, M.R., 2012, October. Design, development, and evaluation of a self-powered GPS tracking system for vehicle security. In *SENSORS, 2012 IEEE* (pp. 1-4). IEEE.

[11] Löhndorf, M., Kvisterøy, T., Westby, E. and Halvorsen, E., 2007. Evaluation of energy harvesting concepts for tire pressure monitoring systems. *Proceedings of Power MEMS*, pp.331-334.

[12] Dondi, D., Napoletano, G., Bertacchini, A., Larcher, L. and Pavan, P., 2012, October. A WSN system powered by vibrations to improve safety of machinery with trailer. In *SENSORS, 2012 IEEE* (pp. 1-4). IEEE.

[13] Gutiérrez, J., Villa-Medina, J.F., Nieto-Garibay, A. and Porta-Gándara, M.Á., 2014. Automated irrigation system using a wireless sensor network and GPRS module. *IEEE transactions on instrumentation and measurement*, *63*(1), pp.166-176.

[14] Brunelli, D., Benini, L., Moser, C. and Thiele, L., 2008, March. An efficient solar energy harvester for wireless sensor nodes. In *2008 Design, Automation and Test in Europe* (pp. 104-109). IEEE.

[15] Yerva, L., Campbell, B., Bansal, A., Schmid, T. and Dutta, P., 2012, April. Grafting energy-harvesting leaves onto the sensornet tree. In *Proceedings of the 11th international conference on Information Processing in Sensor Networks*(pp. 197-208). ACM.

[16] Cong, P., Chaimanonart, N., Ko, W.H. and Young, D.J., 2009. A wireless and batteryless 10-bit implantable blood pressure sensing microsystem with adaptive RF powering for real-time laboratory mice monitoring. *IEEE Journal of Solid-State Circuits*, *44*(12), pp.3631-3644.

[17] Sun, H., Guo, Y.X., He, M. and Zhong, Z., 2012. Design of a high-efficiency 2.45-GHz rectenna for low-input-power energy harvesting. *IEEE Antennas and Wireless Propagation Letters*, *11*, pp.929-932.

[18] Zhao, C., Yisrael, S., Smith, J.R. and Patel, S.N., 2014, September. Powering wireless sensor nodes with ambient temperature changes. In *Proceedings of the 2014 ACM International Joint Conference on Pervasive and Ubiquitous Computing* (pp. 383-387). ACM.

[19] Zhang, C., Syed, A., Cho, Y. and Heidemann, J., 2011, November. Steam-powered sensing. In *Proceedings of the 9th ACM Conference on Embedded Networked Sensor Systems*(pp. 204-217). ACM.

[20] Martin, P., Charbiwala, Z. and Srivastava, M., 2012, November. DoubleDip: Leveraging thermoelectric harvesting for low power monitoring of sporadic water use. In *Proceedings of the 10th ACM Conference on Embedded Network Sensor Systems* (pp. 225-238). Acm.

[21] Rizzon, L., Rossi, M., Passerone, R. and Brunelli, D., 2013, November. Wireless sensor networks for environmental monitoring powered by microprocessors heat dissipation. In *Proceedings of the 1st International Workshop on Energy Neutral Sensing Systems* (p. 8). ACM.

[22] Campbell, B., Ghena, B. and Dutta, P., 2014, November. Energy-harvesting thermoelectric sensing for unobtrusive water and appliance metering. In *Proceedings of the 2nd International Workshop on Energy Neutral Sensing Systems*(pp. 7-12). ACM.

[23] Lossec, M., Multon, B. and Ahmed, H.B., 2013. Sizing optimization of a thermoelectric generator set with heatsink for harvesting human body heat. *Energy conversion and management*, *68*, pp.260-265.

[24] Reimers, C.E., Tender, L.M., Fertig, S. and Wang, W., 2001. Harvesting energy from the marine sediment− water interface. *Environmental science & technology*, *35*(1), pp.192-195.

[25] Donovan, C., Dewan, A., Heo, D. and Beyenal, H., 2008. Batteryless, wireless sensor powered by a sediment microbial fuel cell. *Environmental science & technology*, *42*(22), pp.8591-8596.

[26] Gong, Y., Radachowsky, S.E., Wolf, M., Nielsen, M.E., Girguis, P.R. and Reimers, C.E., 2011. Benthic microbial fuel cell as direct power source for an acoustic modem and seawater oxygen/temperature sensor system. *Environmental science & technology*, *45*(11), pp.5047-5053.

[27] Scorcioni, S., Bertacchini, A., Dondi, D., Larcher, L., Pavan, P. and Mainardi, G., 2011, November. A vibration-powered wireless system to enhance safety in agricultural machinery. In *IECON 2011-37th Annual Conference of the IEEE Industrial Electronics Society* (pp. 3510-3515). IEEE.

[28] Tan, Y.K. and Panda, S.K., 2011. Self-autonomous wireless sensor nodes with wind energy harvesting for remote sensing of wind-driven wildfire spread. *IEEE Transactions on Instrumentation and Measurement*, *60*(4), pp.1367-1377.

[29] Sardini, E. and Serpelloni, M., 2011. Self-powered wireless sensor for air temperature and velocity measurements with energy harvesting capability. *IEEE Transactions on Instrumentation and Measurement*, *60*(5), pp.1838-1844.

[30] Morais, R., Matos, S.G., Fernandes, M.A., Valente, A.L., Soares, S.F., Ferreira, P.J.S.G. and Reis, M.J.C.S., 2008. Sun, wind and water flow as energy supply for small stationary data acquisition platforms. *Computers and electronics in agriculture*, *64*(2), pp.120-132.

[31] Almouahed, S., Gouriou, M., Hamitouche, C., Stindel, E. and Roux, C., 2011. The use of piezoceramics as electrical energy harvesters within instrumented knee implant during walking. *IEEE/ASME Transactions on Mechatronics*, *16*(5), pp.799-807.

[32] Dopico, N.I., Gutiérrez, Á. and Zazo, S., 2012. Performance assessment of a kinetically-powered network for herd localization. *Computers and electronics in agriculture*, *87*, pp.74-84.

[33] Roundy, S., Otis, B.P., Chee, Y.H., Rabaey, J.M. and Wright, P., 2003. A 1.9 GHz RF transmit beacon using environmentally scavenged energy. *optimization*, *4*(2), p.4.

[34] Sample, A.P., Meyer, D.T. and Smith, J.R., 2011. Analysis, experimental results, and range adaptation of magnetically coupled resonators for wireless power transfer. *IEEE Transactions on industrial electronics*, *58*(2), pp.544-554.

[35] Campbell, B., Ghena, B. and Dutta, P., 2014, November. Energy-harvesting thermoelectric sensing for unobtrusive water and appliance metering. In *Proceedings of the 2nd International Workshop on Energy Neutral Sensing Systems*(pp. 7-12). ACM.

[36] Pietrelli, A., Micangeli, A., Ferrara, V. and Raffi, A., 2014. Wireless sensor network powered by a terrestrial microbial fuel cell as a sustainable land monitoring energy system. *Sustainability*, *6*(10), pp.7263-7275.

[37] R. Gherca and R. Olaru, “Harvesting vibration energy by electromagnetic induction,” in Annals of the University of Craiova, Proc. Electrical Engineering

Series, Vol. 35, pp. 123–125, Annals of the university of Craiova, Electrical Engineering Series (2011).

[38] Jha, S.K., 1976. Characteristics and sources of noise and vibration and their control in motor cars. *Journal of Sound and Vibration*, *47*(4), pp.543-558.

[39] Koenig, D., Chiaramont, M. and Balbinot, A., 2008. Wireless network for measurement of whole-body vibration. *Sensors*, *8*(5), pp.3067-3081.

[40] Szefi, J.T., Smith, E.C. and Lesieutre, G.A., 2004. Design and testing of a compact layered isolator for high-frequency helicopter gearbox isolation. In *Collection of Technical Papers-AIAA/ASME/ASCE/AHS/ASC Structures, Structural Dynamics and Materials Conference* (Vol. 6, pp. 4596-4608). American Institute of Aeronautics and Astronautics Inc.(AIAA).

[41] Williams, C.B. and Yates, R.B., 1996. Analysis of a micro-electric generator for microsystems. *sensors and actuators A: Physical*, *52*(1-3), pp.8-11.

[42] Liu, C., 2012. *Foundations of MEMS*. Pearson Education India.

[43] Bao, M., 2005. *Analysis and design principles of MEMS devices*. Elsevier.

[44] Dallago, E., Marchesi, M. and Venchi, G., 2010. Analytical model of a vibrating electromagnetic harvester considering nonlinear effects. *IEEE Transactions on Power Electronics*, *25*(8), pp.1989-1997.

[45] Soliman, M.S.M., El-Saadany, E.F. and Mansour, R.R., 2006, July. Electromagnetic MEMS based micro-power generator. In *2006 IEEE International Symposium on Industrial Electronics*(Vol. 4, pp. 2747-2753). IEEE.

[46] Yuan, Q., Sun, X., Low, C.H., Fang, D.M. and Zhang, H., 2010. Electromagnetic energy harveser fabricated with electrodeposition process. In *Proceedings of PowerMEMS 2010* (pp. 95-98).

[47] Li, X., Hehn, T., Thewes, M., Kuehne, I., Frey, A., Scholl, G. and Manoli, Y., 2013. Non-resonant electromagnetic energy harvester for car-key applications. In *Journal of Physics: Conference Series* (Vol. 476, No. 1, p. 012096). IOP Publishing.

[48] Chamanian, S., Zangabad, R.P., Zarbakhsh, P., Bahrami, M. and Khodaei, M., 2012, February. Wideband capacitive energy harvester based on mechanical frequency-up conversion. In *2012 IEEE Sensors Applications Symposium Proceedings*(pp. 1-4). IEEE.

[49] Vullers, R., van Schaijk, R., Gyselinckx, B. and Van Hoof, C., 2009, June. Is there a sweet spot for energy harvesting?. In *2009 Device Research Conference* (pp. 7-8). IEEE.

[50] O'Riordan, E., Blokhina, E. and Galayko, D., 2016, December. Electromechanical coupling in electrostatic kinetic energy harvesters. In *2016 IEEE International Conference on Electronics, Circuits and Systems (ICECS)* (pp. 436-437). IEEE.

[51] Nicolson, A.M., 1919. The piezo electric effect in the composite rochelle salt crystal. *Transactions of the American institute of electrical engineers*, *38*(2), pp.1467-1493.

[52] Kulah, H. and Najafi, K., 2008. Energy scavenging from low-frequency vibrations by using frequency up-conversion for wireless sensor applications. *IEEE Sensors Journal*, *8*(3), pp.261-268.

[53] Marzencki, M., Defosseux, M. and Basrour, S., 2009. MEMS vibration energy harvesting devices with passive resonance frequency adaptation capability. *Journal of Microelectromechanical Systems*, *18*(6), pp.1444-1453.

[54] Zhu, D., Tudor, M.J. and Beeby, S.P., 2009. Strategies for increasing the operating frequency range of vibration energy harvesters: a review. *Measurement Science and Technology*, *21*(2), p.022001.

[55] Karami, M.A., Bilgen, O., Inman, D.J. and Friswell, M.I., 2011. Experimental and analytical parametric study of single-crystal unimorph beams for vibration energy harvesting. *IEEE transactions on ultrasonics, ferroelectrics, and frequency control*, *58*(7), pp.1508-1520.

[56] Jamain, U.M., Ibrahim, N.H. and Ab Rahim, R., 2014, August. Performance analysis of zinc oxide piezoelectric MEMS energy harvester. In *2014 IEEE International Conference on Semiconductor Electronics (ICSE2014)* (pp. 263-266). IEEE.

[57] Koven, R., Mills, M., Gale, R. and Aksak, B., 2017. Low-frequency and broadband vibration energy harvesting using base-mounted piezoelectric transducers. *IEEE transactions on ultrasonics, ferroelectrics, and frequency control*, *64*(11), pp.1735-1743.

[58] Ko, Y., Lee, D., Kim, T., Yoo, C.S., Choi, B., Han, S.H., Jang, Y. and Kim, N., 2018, January. Design of cantilever type piezoelectric energy harvester with

wideband frequency operation for wireless sensor network. In *2018 International Conference on Electronics, Information, and Communication (ICEIC)* (pp. 1-2). IEEE.

[59] Jayarathne, W.M., Nimansala, W.A.T. and Adikary, S.U., 2018, May. Development of a vibration energy harvesting device using piezoelectric sensors. In *2018 Moratuwa Engineering Research Conference (MERCon)* (pp. 197-202). IEEE.

[60] Wang, Z., Matova, S., Elfrink, R., Jambunathan, M., De Nooijer, C., van Schaijk, R. and Vullers, R.J.M., 2012, January. A piezoelectric vibration harvester based on clamped-guided beams. In *2012 IEEE 25th International Conference on Micro Electro Mechanical Systems (MEMS)* (pp. 1201-1204). IEEE.

[61] Ishihara, K., Yung, C.F., Ayón, A.A. and Schmidt, M.A., 1999. Inertial sensor technology using DRIE and wafer bonding with connecting capability. *Journal of Microelectromechanical Systems*, *8*(4), pp.403-408.

[62] Glynne-Jones, P., Beeby, S.P. and White, N.M., 2001. Towards a piezoelectric vibration-powered microgenerator. *IEE Proceedings-Science, measurement and technology*, *148*(2), pp.68-72.

[63] Shahruz, S.M., 2006. Design of mechanical band-pass filters for energy scavenging. *Journal of sound and vibration*, *292*(3-5), pp.987-998.

[64] Fang, H.B., Liu, J.Q., Xu, Z.Y., Dong, L., Wang, L., Chen, D., Cai, B.C. and Liu, Y., 2006. Fabrication and performance of MEMS-based piezoelectric power generator for vibration energy harvesting. *Microelectronics Journal*, *37*(11), pp.1280-1284.

[65] Marzencki, M., Basrour, S., Belgacem, B., Muralt, P. and Colin, M., 2007, May. Comparison of piezoelectric MEMS mechanical vibration energy scavengers. In *Nanotech 2007*(pp. 21-24). CRC Press.

[66] Xue, H., Hu, Y. and Wang, Q.M., 2008. Broadband piezoelectric energy harvesting devices using multiple bimorphs with different operating frequencies. *IEEE transactions on ultrasonics, ferroelectrics, and frequency control*, *55*(9), pp.2104-2108.

[67] Muralt, P., Marzencki, M., Belgacem, B., Calame, F. and Basrour, S., 2009. Vibration energy harvesting with PZT micro device. *Procedia Chemistry*, *1*(1), pp.1191-1194.

[68] Lee, B.S., Lin, S.C., Wu, W.J., Wang, X.Y., Chang, P.Z. and Lee, C.K., 2009. Piezoelectric MEMS generators fabricated with an aerosol deposition PZT thin film. *Journal of Micromechanics and Microengineering*, *19*(6), p.065014.

[69] Hirasawa, T.H., Yen, Y.T.T., Wright, P.K., Pisano, A.P. and Lin, L., 2010. Design and fabrication of piezoelectric aluminum nitride corrugated beam energy harvester. *Proc. Power MEMS*, pp.211-214.

[70] Elfrink, R., Renaud, M., Kamel, T.M., De Nooijer, C., Jambunathan, M., Goedbloed, M., Hohlfeld, D., Matova, S., Pop, V., Caballero, L. and Van Schaijk, R., 2010. Vacuum-packaged piezoelectric vibration energy harvesters: damping contributions and autonomy for a wireless sensor system. *Journal of Micromechanics and Microengineering*, *20*(10), p.104001.

[71] Blystad, L.C.J., Halvorsen, E. and Husa, S., 2010. Piezoelectric MEMS energy harvesting systems driven by harmonic and random vibrations. *IEEE transactions on ultrasonics, ferroelectrics, and frequency control*, *57*(4), pp.908-919.

[72] Park, J.C., Park, J.Y. and Lee, Y.P., 2010. Modeling and characterization of piezoelectric d_{33}-mode MEMS energy harvester. *Journal of Microelectromechanical Systems*, *19*(5), pp.1215-1222.

[73] Morimoto, K., Kanno, I., Wasa, K. and Kotera, H., 2010. High-efficiency piezoelectric energy harvesters of c-axis-oriented epitaxial PZT films transferred onto stainless steel cantilevers. *Sensors and Actuators A: Physical*, *163*(1), pp.428-432.

[74] Durou, H., Ardila-Rodriguez, G.A., Ramond, A., Dollat, X., Rossi, C. and Esteve, D., 2010. Micromachined bulk PZT piezoelectric vibration harvester to improve effectiveness over low amplitude and low frequency vibrations. *Proc. Power MEMS'10*, pp.27-30.

[75] Hu, Y., Wang, J., Yang, F., Xue, H., Hu, H. and Wang, J., 2011. The effects of first-order strain gradient in micro piezoelectric-bimorph power harvesters. *IEEE transactions on ultrasonics, ferroelectrics, and frequency control*, *58*(4), pp.849-852.

[76] Chang, J.Y., 2011. Modeling and analysis of piezo-elastica energy harvester in computer hard disk drives. *IEEE Transactions on Magnetics*, *47*(7), pp.1862-1867.

[77] Karami, M.A., Bilgen, O., Inman, D.J. and Friswell, M.I., 2011. Experimental and analytical parametric study of single-crystal unimorph beams for vibration energy harvesting. *IEEE transactions on ultrasonics, ferroelectrics, and frequency control*, *58*(7), pp.1508-1520.

[78] Liu, H., Tay, C.J., Quan, C., Kobayashi, T. and Lee, C., 2011. Piezoelectric MEMS energy harvester for low-frequency vibrations with wideband operation range and steadily increased output power. *Journal of Microelectromechanical systems*, *20*(5), pp.1131-1142.

[79] Hajati, A. and Kim, S.G., 2011. Ultra-wide bandwidth piezoelectric energy harvesting. *Applied Physics Letters*, *99*(8), p.083105.

[80] Lei, A., Xu, R., Thyssen, A., Stoot, A.C., Christiansen, T.L., Hansen, K., Lou-Moeller, R., Thomsen, E.V. and Birkelund, K., 2011, January. MEMS-based thick film PZT vibrational energy harvester. In *2011 IEEE 24th International Conference on Micro Electro Mechanical Systems* (pp. 125-128). IEEE.

[81] Defosseux, M., Allain, M., Defay, E. and Basrour, S., 2012. Highly efficient piezoelectric micro harvester for low level of acceleration fabricated with a CMOS compatible process. *Sensors and Actuators A: Physical*, *188*, pp.489-494.

[82] Xu, R., Lei, A., Dahl-Petersen, C., Hansen, K., Guizzetti, M., Birkelund, K., Thomsen, E.V. and Hansen, O., 2012. Fabrication and characterization of MEMS-based PZT/PZT bimorph thick film vibration energy harvesters. *Journal of Micromechanics and Microengineering*, *22*(9), p.094007.

[83] Kanno, I., Ichida, T., Adachi, K., Kotera, H., Shibata, K. and Mishima, T., 2012. Power-generation performance of lead-free (K, Na) NbO3 piezoelectric thin-film energy harvesters. *Sensors and Actuators A: Physical*, *179*, pp.132-136.

[84] Al Ahmad, M. and Jabbour, G.E., 2012. Electronically droplet energy harvesting using piezoelectric cantilevers. *Electronics letters*, *48*(11), pp.647-649.

[85] Cui, N., Wu, W., Zhao, Y., Bai, S., Meng, L., Qin, Y. and Wang, Z.L., 2012. Magnetic force driven nanogenerators as a noncontact energy harvester and sensor. *Nano letters*, *12*(7), pp.3701-3705.

[86] Sang, Y., Huang, X., Liu, H. and Jin, P., 2012. A vibration-based hybrid energy harvester for wireless sensor systems. *IEEE transactions on Magnetics*, *48*(11), pp.4495-4498.

[87] Wang, Q., Cao, Z.P. and Kuwano, H., 2012. Metal-based piezoelectric energy harvesters by direct deposition of PZT thick films on stainless steel. *Micro & Nano Letters*, *7*(12), pp.1158-1161.

[88] Berdy, D.F., Srisungsitthisunti, P., Jung, B., Xu, X., Rhoads, J.F. and Peroulis, D., 2012. Low-frequency meandering piezoelectric vibration energy harvester. *IEEE transactions on ultrasonics, ferroelectrics, and frequency control*, *59*(5), pp.846-858.

[89] Elvin, N.G. and Elvin, A.A., 2013. Vibrational energy harvesting from human gait. *IEEE/ASME Transactions on Mechatronics*, *18*(2), pp.637-644.

[90] Yun, D. and Yun, K.S., 2013. Woven piezoelectric structure for stretchable energy harvester. *Electronics Letters*, *49*(1), pp.65-66.

[91] Gao, X., Shih, W.H. and Shih, W.Y., 2013. Flow energy harvesting using piezoelectric cantilevers with cylindrical extension. *IEEE Transactions on Industrial Electronics*, *60*(3), pp.1116-1118.

[92] Usman, A., Mukhtar, M. and Umer, R.M., 2014, December. MEMS based wireless energy harvesting mechanism for ECG and BCG application. In *2014 International Conference on Emerging Technologies (ICET)* (pp. 142-146). IEEE.

[93] Alsuwaiyan, A.S., Eltaib, M.E.H. and Sherif, H.A., 2014, August. Ambient vibrations piezoelectric harvester array with discrete multiple low frequencies. In *2014 2nd International Conference on Technology, Informatics, Management, Engineering & Environment* (pp. 174-178). IEEE.

[94] Xu, R. and Kim, S.G., 2015. Low-frequency, low-G MEMS piezoelectric energy harvester. In *Journal of Physics: Conference Series* (Vol. 660, No. 1, p. 012013). IOP Publishing.

[95] Saadon, S. and Wahab, Y., 2015, November. From ambient vibrations to green energy source: MEMS piezoelectric energy harvester for low frequency application. In *2015 IEEE Student Symposium in Biomedical Engineering & Sciences (ISSBES)*(pp. 59-63). IEEE.

[96] Emamian, S., Chlaihawi, A.A., Narakathu, B.B., Bazuin, B.J. and Atashbar, M.Z., 2016, October. A piezoelectric based vibration energy harvester fabricated using screen printing technique. In *2016 IEEE SENSORS* (pp. 1-3). IEEE.

[97] Nguyen, M.S., Yoon, Y.J., Kwon, O. and Kim, P., 2017. Lowering the potential barrier of a bistable energy harvester with mechanically rectified motion of an auxiliary magnet oscillator. *Applied Physics Letters*, *111*(25), p.253905.

[98] Wang, X., Chen, C., Wang, N., San, H., Yu, Y., Halvorsen, E. and Chen, X., 2017. A frequency and bandwidth tunable piezoelectric vibration energy harvester using multiple nonlinear techniques. *Applied energy*, *190*, pp.368-375.

[99] Jackson, N., Olszewski, O., Mathewson, A. and O'Murchu, C., 2018, January. Ultra-low frequency PiezoMEMS energy harvester for a leadless pacemaker. In *2018 IEEE Micro Electro Mechanical Systems (MEMS)* (pp. 642-645). IEEE.

[100] Wen, S., Xu, Q. and Zi, B., 2018. Design of a new piezoelectric energy harvester based on compound two-stage force amplification frame. *IEEE Sensors Journal*, *18*(10), pp.3989-4000.

[101] Nabavi, S. and Zhang, L., 2019. Nonlinear Multi-mode Wideband Piezoelectric MEMS Vibration Energy Harvester. *IEEE Sensors Journal*.

[102] Wen, S. and Xu, Q., 2019. Design of a Novel Piezoelectric Energy Harvester Based on Integrated Multi-Stage Force Amplification Frame. *IEEE/ASME Transactions on Mechatronics*.

[103] Mukhiya, R., Bagolini, A., Margesin, B., Zen, M. and Kal, S., 2006. ⟨ 1 0 0⟩ bar corner compensation for CMOS compatible anisotropic TMAH etching. *Journal of micromechanics and microengineering*, *16*(11), p.2458.

[104] Prasad, M., Sahula, V. and Khanna, V.K., 2013. Design and fabrication of Si-diaphragm, ZnO piezoelectric film-based MEMS acoustic sensor using SOI wafers. *IEEE transactions on semiconductor manufacturing*, *26*(2), pp.233-241.

[105] Sharma, A., Mukhiya, R., Kumar, S.S. and Pant, B.D., 2013. Design and simulation of bulk micromachined accelerometer for avionics application. In *VLSI Design and Test* (pp. 94-99). Springer, Berlin, Heidelberg.

[106] Upadhye, V. and Agashe, S., 2016. Effect of Temperature and Pressure Variations on the Resonant Frequency of Piezoelectric Material. *Measurement and Control*, *49*(9), pp.286-292.

Bio - Data

Shanky Saxena, born on 20th June 1986, is currently working as a research scholar in the Department of Electronics and Communication Engineering, Malaviya National Institute of Technology, Jaipur. He graduated in Electronics and Communication Engineering from the University of Rajasthan in 2008 and did Masters in Communication and Signal Processing from Jaipur National University, Jaipur in 2013. He has worked as a Research Scholar at the MEMS and Microsensors Department, CSIR-Central Electronics Engineering Research Institute, Pilani, India. His research interests include MEMS-based piezoelectric vibration energy harvesters and energy harvesting for bio-medical applications.